

Springer Theses

Recognizing Outstanding Ph.D. Research

Jia Liu

Biomimetics Through Nanoelectronics

Development of Three Dimensional
Macroporous Nanoelectronics for
Building Smart Materials, Cyborg
Tissues and Injectable Biomedical
Electronics

 Springer

Springer Theses

Recognizing Outstanding Ph.D. Research

Aims and Scope

The series “Springer Theses” brings together a selection of the very best Ph.D. theses from around the world and across the physical sciences. Nominated and endorsed by two recognized specialists, each published volume has been selected for its scientific excellence and the high impact of its contents for the pertinent field of research. For greater accessibility to non-specialists, the published versions include an extended introduction, as well as a foreword by the student’s supervisor explaining the special relevance of the work for the field. As a whole, the series will provide a valuable resource both for newcomers to the research fields described, and for other scientists seeking detailed background information on special questions. Finally, it provides an accredited documentation of the valuable contributions made by today’s younger generation of scientists.

Theses are accepted into the series by invited nomination only and must fulfill all of the following criteria

- They must be written in good English.
- The topic should fall within the confines of Chemistry, Physics, Earth Sciences, Engineering and related interdisciplinary fields such as Materials, Nanoscience, Chemical Engineering, Complex Systems and Biophysics.
- The work reported in the thesis must represent a significant scientific advance.
- If the thesis includes previously published material, permission to reproduce this must be gained from the respective copyright holder.
- They must have been examined and passed during the 12 months prior to nomination.
- Each thesis should include a foreword by the supervisor outlining the significance of its content.
- The theses should have a clearly defined structure including an introduction accessible to scientists not expert in that particular field.

More information about this series at <http://www.springer.com/series/8790>

Jia Liu

Biomimetics Through Nanoelectronics

Development of Three Dimensional
Macroporous Nanoelectronics for Building
Smart Materials, Cyborg Tissues
and Injectable Biomedical Electronics

Doctoral Thesis accepted by
Harvard University, USA

 Springer

Author

Dr. Jia Liu
Department of Chemistry and Chemical
Biology
Harvard University
Cambridge, CA
USA

Supervisor

Prof. Charles M. Lieber
Harvard University
Cambridge
USA

and

Department of Chemical Engineering
Stanford University
Stanford, CA
USA

ISSN 2190-5053

Springer Theses

ISBN 978-3-319-68608-0

<https://doi.org/10.1007/978-3-319-68609-7>

ISSN 2190-5061 (electronic)

ISBN 978-3-319-68609-7 (eBook)

Library of Congress Control Number: 2017955240

© Springer International Publishing AG 2018

This work is subject to copyright. All rights are reserved by the Publisher, whether the whole or part of the material is concerned, specifically the rights of translation, reprinting, reuse of illustrations, recitation, broadcasting, reproduction on microfilms or in any other physical way, and transmission or information storage and retrieval, electronic adaptation, computer software, or by similar or dissimilar methodology now known or hereafter developed.

The use of general descriptive names, registered names, trademarks, service marks, etc. in this publication does not imply, even in the absence of a specific statement, that such names are exempt from the relevant protective laws and regulations and therefore free for general use.

The publisher, the authors and the editors are safe to assume that the advice and information in this book are believed to be true and accurate at the date of publication. Neither the publisher nor the authors or the editors give a warranty, express or implied, with respect to the material contained herein or for any errors or omissions that may have been made. The publisher remains neutral with regard to jurisdictional claims in published maps and institutional affiliations.

Printed on acid-free paper

This Springer imprint is published by Springer Nature

The registered company is Springer International Publishing AG

The registered company address is: Gewerbestrasse 11, 6330 Cham, Switzerland

Supervisor's Foreword

Three-dimensionally seamless and noninvasive integration of electronics within biological tissues could allow continuous monitoring and modulation of tissue activities for applications ranging from tissue activity mapping to electronics-enabled therapies. Previous studies have been only focused on placing tissue slices on rigid electronic devices or covering flexible electronics on tissue surfaces, which have greatly limited the interface between electronic components with cells in the interior space of tissues. This thesis describes Dr. Jia Liu's fundamental research results during his doctoral study in the Department of Chemistry and Chemical Biology at Harvard University to answer the question of how to integrate electronics in a three-dimensionally seamless and noninvasive way within biological tissues to build a direct electronics–cellular interface through the whole biological tissue *in vitro* and *in vivo*.

Dr. Liu started his research with the design of nanoelectronic sensor arrays into a three-dimensional (3D), flexible, and macroporous structure, which fully mimics the structure of the extracellular matrix. He extended the contact printing method to assemble synthesized silicon nanowires as nanoelectronic components on patterned polymer structures and fabricated two-dimensional (2D) macroporous nanoelectronics as precursors for 3D nanoelectronics. Dr. Liu designed the metal interconnects with internal strain, which, after being peeled-off from substrate, self-roll up to reorganize the 2D nanoelectronic precursor into a 3D macroporous nanoelectronic network. Dr. Liu demonstrated that this 3D macroporous nanoelectronics network could be integrated within conventional soft materials and functioned as chemical, mechanical, and photonic detector arrays. The 3D nanoelectronics do not alter the chemical and physical properties of those soft materials due to their high porosity, nanoscale feature size, and ultra-flexibility.

Through the collaboration with Dr. Bozhi Tian, Dr. Liu designed macroporous nanoelectronics into nanoelectronics tissue scaffolds (nanoES), combined these nanoES with synthetic tissue scaffolds, and cultured synthetic tissues. The results demonstrated a seamless and noninvasive interpenetration of synthetic cellular networks with nanoelectronic networks. Dr. Liu demonstrated the 3D recording of the synthetic tissues responses to the external drug stimulations and pH change.

These nanoelectronics-innervated synthetic tissues have now been referred to as “cyborg tissues” by societies, but that also left the question of how to get this inside a living animal, especially a living brain. So, Dr. Liu further developed a syringe-injectable method to deliver the macroporous nanoelectronics into brain tissue injected by a 100- μm -diameter needle through a hole on the skull. By specific mechanical design, the macroporous nanoelectronics can self-scroll up into a tubular structure inside the needle to be precisely delivered into targeted region inside the brain with no damage to the device for recording of neural activity at single spike and single cellular level. The injected electronics are one millionth times more flexible than conventional implantable electronics and contain more than 95% empty space. They can unfold in the cavity region inside brain such as the lateral ventricle and partially unfold in the dense tissue region. After 5-week implantation, the injected macroporous nanoelectronics interpenetrate with neural networks with no immune response and inflammation. In addition, Dr. Liu also demonstrated that the injected macroporous nanoelectronic network can promote the proliferation and migration of neural progenitor cells and co-injection of cultured cells with electronics, which paves the way for the potential nanoelectronics-enabled cellular therapies. The syringe-injectable electronics have been awarded as Top Research of 2015 by *Chemical & Engineering News* and 10 World Changing Ideas by *Scientific American*.

This thesis work shows the most advanced technology of building electronics–tissue interface in vitro and in vivo, which opens up unprecedented opportunities from fundamental research of brain activity mapping to nanoelectronics-enabled drug screening assays and therapies.

Cambridge, MA, USA
February 2016

Prof. Charles M. Lieber

Preface

Nanoscale materials enable unique opportunities at the interface between physical and life sciences. The interface between nanoelectronic devices and biological systems makes possible communication between these two diverse systems at the length scale relevant to biological functions. The development of a “bottom-up” paradigm allows nanoelectronic units to be synthesized and patterned on unconventional substrates. In this thesis, I will focus on the development of three-dimensional (3D) and flexible nanoelectronics, which mimics the physical and chemical properties of biomaterials in order to explore fundamentally new methods for the seamless integration of electronics with other systems, with a special focus on living biological tissue.

First, I introduce a mechanics-driven strategy that employs “bottom-up” approach for the fabrication of ultra-flexible 3D macroporous nanoelectronic networks, which have the porosity larger than 99%, hundreds of addressable nanodevices and feature sizes ranging from 10 μm to 10 nm. Second, I demonstrate that these nanoelectronics as nanoelectronic scaffolds (nanoES) that mimic the structure of natural extracellular matrix can be easily integrated with organic gels, polymers, and biomaterials without altering their physical/chemical properties. Notably, these devices, as functional embedded systems, can sense local optical, voltage, chemical, and strain signals in hybrid materials. Third, I present the culture of synthetic tissues within these nanoES to generate “cyborg” tissues, introducing a fundamentally new way to seamlessly integrate nanoelectronics with tissues in 3D to precisely interrogate the whole tissue activity at single cell and single spike level. The response of cyborg tissue to the external drug stimulation and microenvironment pH change can be monitored in real time by the embedded devices. Finally, I report a freestanding “mesh electronics” that can be delivered through syringe injection and self-restore their geometric configuration. This mesh electronics can be injected into *in vivo* systems for a chronic brain–machine interface at single neuron level in a minimally invasive way, representing the *state-of-the-art* brain–machine interface. Multiplexed recording of brain signals from nanosensors on the scaffold shows promise for the precise mapping of brain activity. The macroporous structure of the electronics allows reorganization of the neural tissue surround and within the

electronic network and promotes migration of adult neural stem cells from the subventricular zone to the electronic network. The ultra-flexibility and nanoscale feature size fully mimic the mechanical properties of the tissue, eliminating the immunoresponse from the brain tissue to the implanted electronics. Together, these results open up new directions in the design of nanoelectronics and integration of nanoelectronics with living cellular networks, tissues, and organs, bringing opportunities that we can explore to fundamentally revolutionize fields ranging from smart systems design and regenerative medicine to brain-machine interface.

Palo Alto, USA
Nov 2017

Dr. Jia Liu

Parts of this thesis have been published in the following documents:

1. C. Xie*, **J. Liu***, T. Fu*, X. Dai, W. Zhou and C.M. Lieber, “Three-dimensional macroporous nanoelectronic networks as minimally-invasive brain probes,” *Nature Mater.* **14**, 1286-1292 (2015).
2. **J. Liu***, T. Fu*, Z. Cheng*, G. Hong, T. Zhou, L. Jin, M. Duvvuri, Z. Jiang, P. Kruskal, C. Xie, Z. Suo, Y. Fang and C.M. Lieber, “Syringe injectable electronics,” *Nature Nano.* **10**, 629-636 (2015).
3. **J. Liu***, C. Xie*, X. Dai*, L. Jin, W. Zhou and C.M. Lieber, “Multifunctional three-dimensional macroporous nanoelectronic networks for smart materials,” *Proc. Natl. Acad. Sci. USA.* **110**, 6694-6699 (2013).
4. B. Tian*, **J. Liu***, T. Dvir*, L. Jin, J.H. Tsui, Q. Qing, Z. Suo, R. Langer, D.S. Kohane and C.M. Lieber, “Macroporous nanowire nanoelectronic scaffolds for synthetic tissues,” *Nature Mater.* **11**, 986-994 (2012).

(*indicates equal contributors)

Acknowledgements

The life in graduate school has been one of the most important experiences in my life. I would like to express my appreciation to many people who made this possible.

First of all, I would like to thank my advisor, Prof. Charles M. Lieber, for his advice and inspiration, who has offered me great opportunities and constant inspiration. Professor Lieber is an incredible advisor and a great mentor. I want to thank him for providing invaluable guidance to me in science and research. I admire his constant enthusiasm and persistence for exploring new things and concepts. I greatly appreciate his support, which has been critical to my research at Harvard these years, and his patience to help me improve my capability of research, writing, and presentation.

My sincere gratitude is also due to members of my Graduate Advising Committee, Prof. Xiaowei Zhuang, Prof. Daniel Nocera, and Prof. Sunney Xie for the time they spent discussing my research and giving me invaluable advice for achieving my results, and great support they offered.

I also want to thank Dr. Jinlin Huang, for his valuable advice, tremendous support, and trust throughout these years. It is very pleasure to me to work with Jinlin, who is a very experienced person in electronics. His exceptional insights are greatly appreciated.

I would like to acknowledge Prof. Bozhi Tian, Prof. Quan Qing, and Prof. Zhe Yu, who gave me great help and bring me into the field of nanoscience, nano-electronics, and nanobiotechnology area. Without them, the work in this thesis would not have been possible achieved. I would like to acknowledge Prof. Tal Dvir, Zengguang Cheng, Xiaochuan Dai, Dr. Wei Zhou, Prof. Xiaojie Duan, Tian-ming Fu, and Dr. Chong Xie for the fruitful collaborations. The many hours of discussion have enriched my knowledge in many ways. I also want to thank Dr. Ping Xie for his tremendous help for the fabrication, electronics, and measurement; Dr. Jun Yao for his inspiration in nanowire assembly and electronics characterization; and Dr. Lu Wang and Sirui Zou for their great help in the biomolecular sensing experiments. I would like to thank Zhe Jiang, Dr. Thomas Kempa, Dr. Hao Yan,

Dr. Xiaochen Jiang, and Prof. Tzahi Cohen-Karni, for their great help in experiments. Discussions with them inspired me in many ways. I also want to thank Robert Day and Max Mankin for their great efforts on maintaining the nanowire growth setup and bring me lots of tips for the chemical vapor growth. My sincere thanks are also due to Dr. James Cahoon, Dr. Yongjie Hu, Dr. SungWoo Nam, Hwan Sung Choe, Dr. Jang-Ung Park, Dr. Steffen Strehle, Dr. Yajie Dong, Ruixuan Gao, Dr. Didier Casanova, Lin Xu, Dr. Peter Kruskal, Dr. Jae-Hyun Lee, Tao Zhou, Wenshan Zheng, and Sean You for the help and support, and making lab such a pleasure place to work. I want to express my great gratitude to Dr. Yue Yang for teaching my skill for neuron cell culture, Jiang He for immunostaining, and Dr. Lihua Jin and Prof. Zhigang Suo for their great help in mechanical simulation and subsequent inspiration for electronics design. I appreciate technical help from Yuan Lu, Jiandong Deng, and Steve Shepard, and also the administrative assistance from Purvant Patel, Kathleen Ledyard, and Renée Donlon.

I would like to thank my parents for their endless love, unflinching support, tremendous trust, and encouragement for all these years of my studies and helped me go through those difficult times.

Finally, I am grateful to all of you who have directly or indirectly contributed to the completion of this work.

Contents

1	Introduction	1
1.1	Synthesis of Nanowires as Nanoelectronic Units	2
1.2	Assembly of Nanowires for Flexible and 3D High-Performance Nanoelectronics	3
1.3	Nanoelectronics in Biology: Interfacing with Living Cells	5
1.4	Nanoelectronics in Biology: Interfacing with Living Tissues and Organs	7
1.5	Overview of Thesis	8
	Bibliography	9
2	Three-Dimensional Macroporous Nanoelectronics Network	15
2.1	Introduction	15
2.2	Experimental	16
2.2.1	3D Macroporous Nanowire Nanoelectronic Network Fabrication	16
2.2.2	Three-Layer Interconnect Ribbon for Mechanical Simulation	17
2.2.3	Characterization and Measurement of Macroporous Nanoelectronics	17
2.3	Results and Discussion	19
2.3.1	3D Macroporous Nanoelectronic Network	19
2.3.2	Mechanics Analysis	22
2.4	Conclusions	24
	Bibliography	24
3	Integration of Three-Dimensional Macroporous Nanoelectronics with Materials	27
3.1	Introduction	27
3.2	Experimental	27
3.2.1	Optically Addressable 3D Macroporous Nanoelectronic Network	27

3.2.2	3D Macroporous Chemical Sensors Network	28
3.2.3	3D Macroporous Strain Sensors Network	28
3.3	Results and Discussion	28
3.3.1	Imaging Nanowire Device in 3D Structure	28
3.3.2	Mapping Chemical Diffusion in Gel	32
3.3.3	Mapping Strain Distribution in Elastomer	34
3.4	Conclusion	36
	Bibliography	37
4	Three-Dimensional Macroporous Nanoelectronics Scaffold	
	Innervated Synthetic Tissue	39
4.1	Introduction	39
4.2	Experimental	41
4.2.1	NanoES/Tissue Scaffold	41
4.2.2	Scaffold Mechanical Properties	42
4.2.3	Cell Culture	42
4.2.4	Staining	45
4.2.5	Characterization	46
4.2.6	Electrical Measurement	46
4.3	Results and Discussion	46
4.3.1	NanoES Characterization	46
4.3.2	Mechanics-Driven 3D Self-organization	50
4.3.3	NanoES/Tissue Scaffold Hybrids	52
4.3.4	Characterization of NanoES/Tissue Interface	53
4.3.5	Monitoring of Cell Activity Change to External Stimulations	56
4.4	Conclusion	61
	Bibliography	62
5	Syringe Injectable Electronics	65
5.1	Introduction	65
5.2	Experimental	66
5.2.1	Freestanding Mesh Electronics Fabrication	66
5.2.2	Mesh Structure Design	66
5.2.3	Injection of Mesh Electronics	68
5.2.4	Injection of Mesh Electronics into Behaving Animals	70
5.2.5	Mechanical Analysis	72
5.2.6	Electrical Measurement	74
5.2.7	Characterization	75
5.2.8	Chronic Damage Analysis	77
5.3	Results and Discussion	78
5.3.1	Syringe-Injectable Electronics	78
5.3.2	Parameters for Syringe Injectable Electronics	81
5.3.3	Syringe-Injectable Electronics for Soft Matters	85

5.3.4 Syringe-Injectable Electronics for Behaving	
Rodent Brains	88
5.4 Conclusion	91
Bibliography	92
6 Outlook	95
Bibliography	97

Abbreviations

CVD	Chemical vapor deposition
DAPI	4',6-diamidino-2-phenylindole
FET	Field-effect transistor
GFAP	Glial fibrillary acidic protein
I-V	Current-Voltage
NeuN	Hexaribonucleotide binding protein-3
PLGA	Poly(lactic-co-glycolic acid)
S/D	Source/Drain
SEM	Scanning electron microscopy
SVZ	Subventricular zone
Tuj 1	Anti-beta III tubulin

List of Figures

Fig. 1.1	Contact printing nanowire for assembly	3
Fig. 1.2	Intracellular electrical recording by nanowire nanoFET device	6
Fig. 2.1	Schematic of macroporous nanoelectronics fabrication	16
Fig. 2.2	Bending stiffness measurements	18
Fig. 2.3	Strategy for preparing 3D macroporous nanoelectronic networks	19
Fig. 2.4	Organized 2D and 3D macroporous nanoelectronic networks . . .	21
Fig. 2.5	Schematics for bending stiffness calculation	23
Fig. 3.1	Strategy for integration of 3D macroporous nanoelectronics with host materials	29
Fig. 3.2	3D macroporous photodetectors network and device localization	30
Fig. 3.3	Localization of 3D macroporous nanoelectronic devices	31
Fig. 3.4	3D macroporous chemical sensors.	33
Fig. 3.5	3D macroporous strain sensors embedded in elastomer.	34
Fig. 3.6	Calibration of the 3D macroporous nanoelectronic strain sensors.	35
Fig. 4.1	Integrating nanoelectronics with cells and tissue	40
Fig. 4.2	Chip assembly for neuronal 3D cultures	43
Fig. 4.3	Schematic of cardiomyocyte 3D culture	44
Fig. 4.4	Schematic of vascular nanoES construct preparation and pH sensing	45
Fig. 4.5	Macroporous and flexible nanowire nanoES. Device fabrication schematics	47
Fig. 4.6	3D self-organized nanowire nanoES	48
Fig. 4.7	Mesh nanowire nanoES.	48
Fig. 4.8	Device performance characterization	49
Fig. 4.9	Geometry control by design in nanoES.	50
Fig. 4.10	Design and fabrication of self-organized nanoES	51
Fig. 4.11	Hierarchical nanoES	51

Fig. 4.12	Hybrid macroporous nanoelectronic scaffolds	52
Fig. 4.13	NanoES innervated synthetic neural tissue	54
Fig. 4.14	NanoES innervated synthetic cardiac patch	55
Fig. 4.15	Biocompatibility of nanoES.	56
Fig. 4.16	Multiplexed electrical recording from nanoES innervated synthetic cardiac patch	58
Fig. 4.17	Multiplexed 3D recording from hybrid self-organized nanoES/neural constructs.	59
Fig. 4.18	Mesh nanoES innervated synthetic vascular construct	60
Fig. 4.19	Synthetic vascular construct enabled pH sensing.	61
Fig. 5.1	Optical images of electronics structure	67
Fig. 5.2	Schematics of mesh design	68
Fig. 5.3	Loading in needle	70
Fig. 5.4	Mechanics of mesh during rolling.	73
Fig. 5.5	Bonding process	76
Fig. 5.6	Syringe-injectable electronics	78
Fig. 5.7	Stepwise injection	79
Fig. 5.8	Control of injection process.	80
Fig. 5.9	Yield of injection	81
Fig. 5.10	Parameters for injection.	82
Fig. 5.11	Mechanical analysis for injection process	84
Fig. 5.12	Control experiments of thin film electronics in needle.	86
Fig. 5.13	Injectable electronics for soft mater.	87
Fig. 5.14	Inject electronics for tissue engineering	88
Fig. 5.15	Injectable electronics for brain implants	89
Fig. 5.16	Interface between electronics and in vivo regenerative neural tissue	90

Chapter 1

Introduction

In the past half-century, advances in electronics have been driven by increases in their complexity and performance, and decreases in unit size (Moore's law) [1]. The mainstream microelectronics industry continues to provide ever-increasing performance and functionality and brings new technologies in computing, memory, and telecommunication that change the way we live [2]. These developments have in turn spurred interest in "macroelectronics," which requires the low-cost distribution of nanoelectronic units and circuits over the largest possible area in unconventional configurations, for instance on flexible substrates and in 3D geometries [3]. This new type of electronics is expected to bring unimaginable applications in flexible displays and integrated circuits (ICs) [4], from paper-like computers [5, 6] to novel methods and solutions for seamless integration of electronics with our daily life or even our bodies (for example, wearable and implantable biomedical electronics) [7–18].

Traditional nanoelectronics fabrication technology mainly relies on the "top-down" paradigm, in which nanostructures of electronic units are patterned by lithography techniques and subsequently etched from single-crystalline bulk materials (for example, silicon wafers) [19, 20]. This fabrication paradigm intrinsically precludes a high yield, high resolution transfer of nanoelectronic units from the rigid wafer to other substrates. Several unconventional transfer techniques have been developed [21, 22], however, they are still at an early stage, with operation resolution at the micro- or even millimeter scale, and difficult for large-scale fabrication and manufacturing. Another possible solution involves patterned organic electronic materials instead of inorganic materials [6, 11–13]. Their flexible properties and fabrication processes are promising for potential use in large-scale flexible display and consumer wearable electronic devices, however, organic electronic materials do not offer high performance, reliability for advanced amplification device and sensors in ambient environment.

As an alternative, inorganic nanomaterials synthesized through the "bottom-up" paradigm are considered as good candidate for the applications in this field [23–26]. In the bottom-up paradigm, nanomaterials are synthesized from the most primitive

units, atoms, molecules and nanoclusters, and assembled into complex structures [27–30]. The synthesized nanomaterials have been demonstrated as active components for high-performance electronics, sensors and patterned on virtually any substrate and in 3D space. Importantly, the size of these synthetic nanomaterials is comparable to, or even smaller than, the *state-of-the-art* nanoelectronic units in industry [31]. These properties of flexible nanoelectronics such as ultraflexibility, nanoscale feature sizes, high performances, etc. offer a great promise for building bioelectronics and biomedical devices for living cellular and tissue system interface.

1.1 Synthesis of Nanowires as Nanoelectronic Units

Of all nanoelectronic building blocks for macroelectronics, semiconductor nanowires have the most flexible yet controllable structures and electronic properties for the following reasons: (1) Through rational design of catalyst and precursor, virtually all kinds of semiconductor nanowires can be formed [32–39]; (2) nanowire structure and doping can be rationally modulated to meet different requirements, which is very difficult to achieve by traditional fabrication technology [40–44] and (3) high-performance electronics can be realized by synthetic nanowire circuits [45–48].

The most general process for the synthesis of high quality nanowires is the nanocluster-catalyzed vapor-liquid-solid (VLS) growth [49–53]. In this process, metal nanoclusters are heated to form a liquid solution. The presence of a vapor-phase source of the semiconductor results in nucleation sites for the crystallization. The solid-liquid interface forms as the growth interface attracting a continued incorporation of precursor gas and precipitation of semiconductor atoms into the lattice, leading to a preferential one-dimensional growth. Different methods have been explored to grow semiconductor nanowires. The chemical vapor deposition (CVD) process, in which the metal nanocluster serves as a catalyst, is one of the most popular techniques for VLS growth. In the case of Si nanowire growth, Au nanoparticles serve as catalyst sites where the gaseous precursor silane decomposes to provide semiconductor reactants [26, 50]. With appropriate selection of nanocluster catalyst diameter, reactant gases, pressure and temperature, one can easily design nanowire structures de novo and synthesize these structures with different modulations of composition, doping defects and geometry [44]. Based on reports in the literature [18, 44, 54, 55], virtually all electronic units can be synthesized and implemented into single-nanowire structures via the bottom-up paradigm. For example, nanowires involving *p-i-n* dopant modulation in axial and coaxial geometries have been explored to synthesize nanowire photovoltaics [54]. Branched nanowires containing nanowire heterostructures, including single-crystalline semiconductor groups IV, III–V and II–VI and metals, have been explored to synthesize nanowire light-emitting diodes (LEDs), field-effect transistors (FET) and biosensors [55]. Kinked nanowires, with precise geometry design and dopant modulation in the axial direction, have been utilized in the design of localized FET detectors [18, 44].

1.2 Assembly of Nanowires for Flexible and 3D High-Performance Nanoelectronics

A wide range of semiconductor nanowires have been produced via CVD growth with high carrier mobility, including Ge/Si core-shell nanowires (ca. $730 \text{ cm}^2 \text{ V}^{-1} \text{ s}^{-1}$) [45], GaAs nanowires (ca. $4100 \text{ cm}^2 \text{ V}^{-1} \text{ s}^{-1}$) [56] and InAs nanowires (ca. $2000 \text{ cm}^2 \text{ V}^{-1} \text{ s}^{-1}$) [57] yet assemble individual wires into integrated device is challenge. Several assembly methods such as flow-directed alignment [58, 59], blown-bubble technique [60], Langmuir-Blodgett approaches [30, 61, 62] and shear-printing methods [63–65] have been developed to form large-scale oriented nanowire arrays at room temperature on virtually all kinds of substrates, including silicon wafer, glass, plastics, paper, etc. With standard lithography, nanoelectronic units can be coated with a dielectric layer and connected by metal wires to form electronic circuitry on those substrates [47].

Among the different patterning methods, shear-printing methods, especially the lubricant-assisted contact printing method [64], show great promise due to their ability to assemble nanowires uniformly on large scales (several centimeters) and create high-density individually connected nanowire arrays at high efficiency and with high alignment ratios (ca. 90–95% at a $\pm 5^\circ$ misalignment angle) (Fig. 1.1a). This process uses the nanowire growth substrate as a donor substrate to directionally slide over a receiver substrate, which is pre-treated to affiliate with the

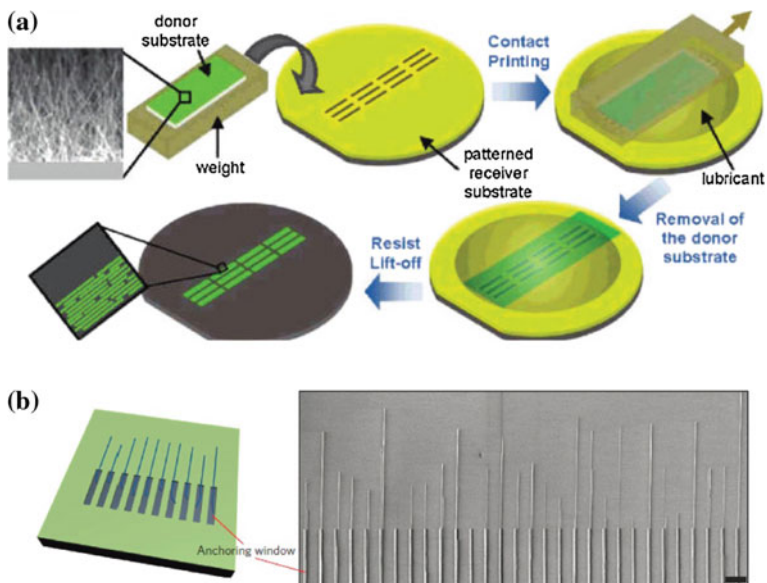


Fig. 1.1 Contact printing nanowire for assembly. **a** Schematics of contact printing nanowire by lubricant-assisted process Reprinted with permission from Ref. [63]. Copyright 2008 American Chemical Society. **b** Schematics and SEM image of contact printing nanowire by deterministic nanocombing Reprinted with permission from Ref. [69]. Copyright 2013 Nature Publishing Group.

nanowire surface chemically or physically. Lubricants such as octane and mineral oils are used between the two substrates to reduce friction. During the contact sliding process, nanowires are detached from the donor substrate by adhesive interactions with the receiver substrate and ultimately realigned by the sliding shear force, resulting in the direct transfer of parallel nanowires to the receiver substrate. After further standard fabrication processes, a well aligned multiple-nanowire device can be fabricated. Through pre-alignment and transfer, McAlpine et al. [66] demonstrated the fabrication of chemical sensors on a flexible substrate. Timko et al. [67] demonstrated the use of contact printing to assemble silicon nanowires on a polymeric substrate to create nanowire FET arrays for electrical detection and recording from chicken cardiomyocytes. Multiplexed recording from these arrays recorded signal propagation times across the myocardium with high spatial resolution. Takei et al. [68] used a contact printing technique to assembly Ge/Si core-shell nanowire on a polyimide substrate to form fully integrated nanowire active matrix circuitry. Integrating it with pressure-sensitive rubber, they demonstrated this circuitry as electronic “skin” for pressure sensing with lower operation voltages (<5 V) than its organic counterparts.

However, this technique has limitations with respect to fabrication of high-performance single-nanowire electronics. While the process enables large-scale and uniform assembly of nanowires, it lacks the control to precisely integrate individual nanowires at the nanometer scale, causing uneven electronic performance. To further extend the contact printing technique, Yao et al. have recently reported a nanocombing assembly technique [69]. This new technique involves defining regions of a surface that can physically or chemically anchor part of the nanowires and then drawing them out over a region of the surface that has little interaction with the nanowire, to stretch and align nanowires in highly oriented arrays (Fig. 1.1b). This method pushes the yield of arrays to greater than 98.5% of the nanowires aligned, to within $\pm 1^\circ$ of the combing direction. With lithography pre-patterning chemically distinct regions, a deterministic assembly has been demonstrated to produce a high yield of single-nanowire (20–30 nm in diameter) devices on different substrates.

In addition, post-growth assembly of nanowires and patterning techniques allow for the integration of electronic units through a layer-by-layer assembly process [64, 65, 70], opening up new opportunities for 3D integrated circuits (3D-ICs). 3D-ICs consisting of multiple layers of active electronic units enable more efficient interconnections, higher integration density, faster operation speed and lower power consumption. Moreover, this technology allows for the integration of different materials without the requirement of materials or processing compatibility. As an example, Nam et al. recently demonstrated the integration of the first layer *n*-InAs nanowire with a second layer *p*-Ge/Si core-shell nanowire to form a vertically interconnected 3D complementary metal–oxide–semiconductor (CMOS) inverter by contact printing [65].

Together, these growth and assembly technologies open up new opportunities to realize nanoelectronics on virtually any kind of substrate and 3D interconnections to usher nanoelectronics design into a new era.

1.3 Nanoelectronics in Biology: Interfacing with Living Cells

Applications of nanoelectronics in biomolecule detection and electrophysiological recording have been highly successful, which offer advantages such as high throughput, scalability and low cost leading to novel analytical devices for disease-marker detection, DNA sequencing and other applications [71–73]. For example, electrophysiological recording of cellular activity is central to areas ranging from basic biophysical study to medical applications [74–88]. In past decades, glass micropipette intracellular probes and sharp electrode probes have been predominantly used to interface with the internal environment of cells [74–77], and multi-electrode arrays [78–81] and planar FETs [81–88] have been used to interface to and record from electrogenic cells. However, these technologies are either invasive or lack the ability to record signals in the intracellular and subcellular regions. Moreover, metal-based electrical recording suffers from the limitation of liquid-solid input impedance, which precludes further decrease of detector size [89].

Recently, there have been several advances using nanowire-based nanoelectronics to interface with single cells. One has been the use of metallic vertical nanowires as detectors to interface with the cells cultured directly on them. Through localized electroporation, the nanowires can break the cell membrane to form a temporary connection between detectors and the intracellular environment [90, 91]. However, this technique is still invasive to cells despite some modifications which allow longer intracellular detection time. Moreover, as mentioned above, metal-based electrical recording probes cannot be made smaller and less invasive without increasing the input impedance. In addition, the amplitude of signal, temporal resolution and signal-to-noise (S/N) are all limited by the sub-microscale size of the detector [89]. Importantly, those vertical metallic nanowires all fail to identify the subthreshold voltage change in action potential recording [90, 91]. On the contrary, the FET has proved to be an “active” detector, in which the sensitivity will drop with decreasing detector size [71, 92]. In an FET device, the potential is recorded by measuring the conductance between the source and drain electrodes. The potential applied to the channels of the FET serves as a gate potential changing the carrier density in the FET channels, which leads to conductance change. This process is independent of the input impedance of the FET channels and source-drain electrodes; therefore, the size of the detector does not affect the sensitivity of the FET. As an example of such an FET detector, Tian et al. synthesized kinked nanowire with ca. 80-nm diameter and modulated its axial doping to localize a lightly doped nanoscale FET region on the tip of the kink with two metallic arms. Stressed metal contacts were formed to leverage the nanowire into a 3D probe. Phospholipid bilayers were coated on the surface of the kinked nanowire to facilitate the penetration of the nanowire into the cell. Using this nanoFET probe, a full amplitude cardiomyocyte action potential with 75–100 mV was recorded (Fig. 1.2a–c) [18]. Moreover, Duan et al. [93] fabricated a silica nanotube, coated

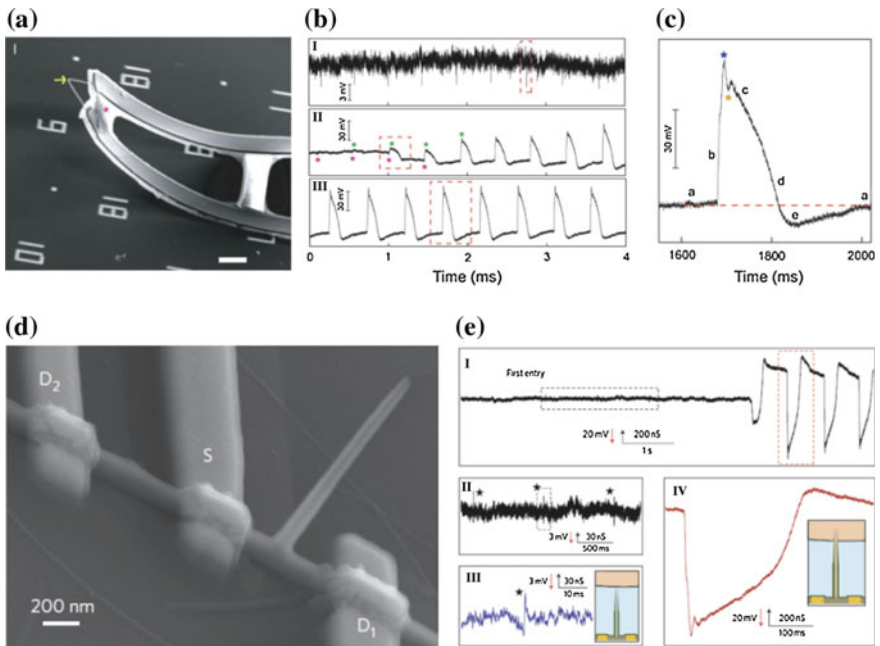


Fig. 1.2 Intracellular electrical recording by nanowire nanoFET device. **a** A 3D, free-standing kinked nanowire FET probe bent up by stress release of the metal interconnects. The yellow arrow and pink star mark the nanoscale FET and SU-8, respectively. Scale bars, 5 μm . **b** Transition from extracellular (I) to intracellular recordings during (II) cellular entrance recorded by a kinked nanowire FET probe from beating cardiomyocytes. Green and pink stars denote the peak positions of intracellular and extracellular signal components, respectively; (III) Steady-state intracellular recording. **c** Zoom-in signals of an intracellular action potential peak. Blue and orange stars designate features that are possibly associated with inward sodium and outward potassium currents, respectively. The letters 'a' to 'e' denote five characteristic phases of a cardiac intracellular potential, as defined in text. The red-dashed line is the baseline corresponding to intracellular resting state. Reprinted with permission from Ref. [18]. Copyright 2010 American Association for the Advancement of Science. **d** SEM image of a BIT-FET device (S-D1) and control device (S-D2). **e** (I), Representative trace (conductance vs. time) reflecting the transition from extracellular to intracellular recording. (II) Magnified view of the trace inside the black dashed rectangle in (I). (III) Magnified view of the trace inside the blue dashed rectangle in (II). The stars in (II) and (III) mark the position of extracellular spikes. (IV) Magnified view of the peak inside the red dashed rectangle in (I). Reprinted with permission from Ref. [93]. Copyright 2014 Nature Publishing Group.

with a phospholipid bilayer, on a silicon nanowire to bring the cytosol into contact with the FET region on the bottom when the tube was inserted into cells (Fig. 1.2d, e). Multiplexed intracellular recordings from a single cell or cellular network have been demonstrated with this technique. Based on these two concepts, several different intracellular electrophysiological recording techniques have been further developed [94–96].

In addition to electrophysiological recording, nanowires and nanowire-related structures have been used for delivery of biomolecular materials into cells that are inaccessible by traditional methods [97–99] to interrogate genomic behavior of cells.

1.4 Nanoelectronics in Biology: Interfacing with Living Tissues and Organs

Progress in nanotechnology has already significantly advanced our ability to interrogate tissue structure. For examples, nanoparticles have been used to image tissue structure and activity in vitro and in vivo [100, 101], and as drug delivery materials to control the release of drugs in tissue [102, 103]; micro- and nanofluidic channels have been used to deliver or inject biomolecules and virus vectors to the targeted tissue region [104] and 3D macroporous materials with micro- and nanoscopic features have been developed to build synthetic tissue scaffolds [105].

While interfacing electronic units with individual cells has been progressed, building electronics-tissues interface is still challenge due to the complicated and compact 3D cellular structure, dynamic movement in behaving objects and molecular responses from tissue to the implanted foreign objects. The emerge of flexible nanoelectronics shows great opportunities for interfacing electronics with living tissues and organs due to: (1) nanoscale feature size of nanoelectronic unit will introduce minimal interrupting to the internal tissue structures and cellular networks, (2) geometry and composition of nanoelectronics engineered to mimic the chemical and physical properties of biomaterials can further facilitate the seamless integration with tissue, (3) unique optical and electrical performances that allow millions to billions functional units to be addressed simultaneously will greatly enhance our capability for tissue activity monitoring, especially for brain mapping, (4) ultraflexibility that eliminates the mechanical mismatch between the living tissue and electronics will enhance the working life and efficiency of those units inside tissue and (5) the unprecedented integration of multiple functions in a small volume (e.g. the volume of one million flexible interconnected nanosensors array will only occupy much less than 1 thousandth volume of a living mice brain) could possibly allow us to seamlessly integrate nanoelectronics within behaving animals to create a true cyborg system.

However, very few works have been done in interfacing nanoelectronics to cellular networks, tissues and organs. The challenges are that (1) tissue has a 3D and heterogeneous structure and (2) in contrast to single cells, cells in tissues closely pack in 3D networks surrounded by dense extracellular matrix which are inaccessible to nanoelectronic units. Some flexible electronics have been used to interface to the top surface of tissue to facilitate attachment and adhesion [16, 17, 106, 107]. However, the surface of tissue provides only limited information that can also be acquired by optical methods [108]. To be delivered into the interior space of tissues, currently nanoelectronic systems need sensors fabricated on the rigid substrates to provide mechanical strength for penetrating though the dense cellular structure and attach functional units targeted cells [109–113]. The dimensions of this rigid substrate need to be micro- to millimeter scale to maintain enough mechanical strength. This approach introduces large acute damage from inserting a significantly large volume of substrate materials (vs. nanoelectronics) into the living system. In addition, the mechanical mismatch between the nanoelectronics and

tissue can cause continuously chronic damage to the surrounding cells during long-term implantation and recording, resulting in severe immunoreactivity, which degrades the quality and efficiency of recording and stimulation.

Although we have many challenges for building electronics-tissue interface, the necessity to deliver and seamlessly integrate nanoelectronic units within tissue in 3D, from subcellular scale to throughout the whole tissue is ever-increasing. For example, the integration of billions of sensing units within brain tissue in behaving animals at single-cell level to minimal-invasively monitor the activity from statistically significant amount of neurons is the key for precise brain activity mapping [114, 115]. Other examples include a smart drug release system coupled with ability to sense microenvironment changes throughout our body [116, 117], a 3D in situ sequencing technique based on the integration of nanopore enabled sequencing technique with 3D tissue [118–120], and the development of a completely cyborg system for robotics. These advances would significantly impact the fields of biomedical devices, tissue engineering and neuroscience and lead to fundamental new understanding of biological systems and its integration with digital systems.

1.5 Overview of Thesis

In this thesis, I first propose a fundamentally new idea for the interfacing and integrating nanoelectronics with tissue *in vitro* and *in vivo*. This new approach involves stepwise incorporation of biomimetic and biological elements into a network with addressable, nanoscale-feature units assembled on a centimeter-size scale in a 3D structure. This electronic network mimics the flexible and macroporous structure of the extracellular matrix as nanoelectronic scaffold (nanoES), which allows its integration with other soft materials and biomaterials without affecting their physical and chemical properties. Then, I introduce the *in vitro* culture of cells within tissue scaffolds that is hybridized with nanoES to build synthetic tissues, in which nanoelectronic units have been intrinsically embedded as cyborg tissues. Finally, I show that the completely freestanding nanoES can be delivered and integrated into *in vivo* rodent brain systems through a minimally invasive syringe-injection. The injected nanoES can unfold within tissue to distribute nanosensors three-dimensionally into the largest possible volume for local field and action potential recording, and act as tissue scaffolds to actively guide stem cell growth.

In Chap. 2, I first introduce a new method to pattern and fabricate a real 3D nanoelectronic network. This 3D network is initially fabricated on a 2D sacrificial layer. Using a contact printing technique and lithography patterning, single-nanowire based nanoelectronics are then patterned into regular arrays formed by polymers. Removing the underlying sacrificial layer allows the 2D nanoelectronics to be organized into 3D structures by either external manipulation or internal stress control.

In Chap. 3, I introduce the integration of these 3D nanoelectronic networks with other soft materials such as PDMS and gel. Moreover, use of nanoelectronic units such as photodetectors, chemical sensors and strain sensors will be demonstrated.

In Chap. 4, I focus on transforming the nanoelectronic network into a 3D network that mimics the structure of different extracellular matrices and integrates with synthetic or natural tissue scaffolds to form hybrid nanoES. Moreover, neurons and cardiomyocytes are cultured within this hybrid nanoES to develop a synthetic cellular construct with embedded nanoelectronics. Their potential application in pharmacology is discussed. Finally, I will discuss that using this nanoES alone with the culture of smooth muscle cells to build a vascular construct that can act as nanoelectronic blood vessel, and discuss the functions of the nanoelectronic pH sensing units in this nanoelectronic blood vessel.

In Chap. 5, I focus on how to deliver and integrate this nanoES into in vivo systems, with emphasis on in vivo rodent brain tissue. Specifically, I introduce a syringe-injection method to deliver the nanoelectronic network. The behavior of the nanoelectronic network in the needle and tissue analogies is discussed. Implantation and the integration of nanoelectronics with brain tissue are analyzed. The vanishingly small immunoreactivity of the tissue to the electronics during chronic implantation is discussed. Finally, preliminary data are presented which show the promise of nanoelectronics as an active tissue scaffold for guiding the outgrowth of neuron stem cells in the subventricular zone.

Bibliography

1. Moore G (1965) Cramming more components onto integrated circuits. *Electronics* 38:114
2. International Technology Roadmap for Semiconductors (2005) Ed., www.itrs.net/common/2005ITRS/Home2005.htm
3. Reuss RH, Hopper DG, Park JG (2006) Macroelectronics. *MRS Bull* 31:447
4. Gelinck GH et al (2004) Flexible active-matrix displays and shift registers based on solution-processed organic transistors. *Nat Mater* 3:106
5. Rogers JA et al (2001) Paper-like electronic displays: large-area rubber-stamped plastic sheets of electronics and microencapsulated electrophoretic inks. *Proc Natl Acad Sci U S A* 98:4835
6. Forrest SR (2004) The path to ubiquitous and low-cost organic electronic appliances on plastic. *Nature* 428:911
7. Dodabalapur A (2006) Organic and polymer transistors for electronics. *Mater Today* 9:24
8. Someya T et al (2005) Conformable, flexible, large-area networks of pressure and thermal sensors with organic transistor active matrixes. *Proc Natl Acad Sci U S A* 102:12321
9. Yu G, Gao J, Hummelen JC, Wudi F, Heeger AJ (1995) Polymer photovoltaic cells: enhanced efficiencies via a network of internal donor-acceptor heterojunctions. *Science* 270:1789
10. Shaheen SE, Ginley DS, Jabbour GE (2005) Organic-Based Photovoltaics: Toward Low-Cost Power Generation. *MRS Bull* 30:10
11. Ouyang J, Chu CW, Szmanda CR, Ma L, Yang Y (2004) Programmable polymer thin film and non-volatile memory device. *Nat Mater* 3:918

12. Baude PF et al (2003) Pentacene-based radio-frequency identification circuitry. *Appl Phys Lett* 82:3964
13. Cantatore E et al (2007) A 13.56-MHz RFID system based on organic transponders. *IEEE J Solid-State Circuits* 42:84
14. Keefer EW, Botterman BR, Romero MI, Rossi AF, Gross GW (2008) Carbon nanotube coating improves neuronal recordings. *Nat Nanotechnol* 3:434
15. Kim DH et al (2011) Materials for multifunctional balloon catheters with capabilities in cardiac electrophysiological mapping and ablation therapy. *Nat Mater* 10:316
16. Kim DH et al (2010) Dissolvable films of silk fibroin for ultrathin conformal bio-integrated electronics. *Nat Mater* 9:511
17. Kim DH et al (2011) Epidermal electronics. *Science* 333:838
18. Tian B et al (2010) Three-dimensional, flexible nanoscale field-effect transistors as localized bioprobes. *Science* 329:831
19. Arns RG (1998) The other transistor: early history of the metal-oxide semiconductor field-effect transistor. *Eng Sci Educ J* 7:233
20. Vogel EM (2007) Technology and metrology of new electronic materials and devices. *Nat Nanotechnol* 2:25
21. Meitl MA et al (2006) Transfer printing by kinetic control of adhesion to an elastomeric stamp. *Nat Mater* 5:33
22. Sun Y, Kim S, Adesida I, Rogers JA (2005) Bendable GaAs metal-semiconductor field-effect transistors formed with printed GaAs wire arrays on plastic substrates. *Appl Phys Lett* 87:083501
23. Murray CB, Kagan CR, Bawendi MG (2000) Synthesis and characterization of monodisperse nanocrystals and close-packed nanocrystal assemblies. *Annu Rev Mater Sci* 30:545
24. Punties VF, Krishnan KM, Alivisatos AP (2001) Colloidal nanocrystal shape and size control: the case of cobalt. *Science* 291:2115
25. Iijima S (1991) Pentagons, heptagons and negative curvature in graphite microtubule growth. *Nature* 354:56
26. Morales AM, Lieber CM (1998) A laser ablation method for the synthesis of crystalline semiconductor nanowires. *Science* 279:208
27. Schreiber F (2000) Structure and growth of self-assembling monolayers. *Prog Surf Sci* 65:151
28. Li XS et al (2009) Large-area synthesis of high-quality and uniform graphene films on copper foils. *Science* 324:1312
29. Kim KS et al (2009) Large-scale pattern growth of graphene films for stretchable transparent electrodes. *Nature* 457:706
30. Whang D, Jin S, Wu Y, Lieber CM (2003) Large-scale hierarchical organization of nanowire arrays for integrated nanosystems. *Nano Lett* 3:1255
31. Lieber CM (2003) Nanoscale science and technology: building a big future from small things. *MRS Bull* 28:486
32. Duan XF, Lieber CM (2000) General synthesis of compound semiconductor nanowires. *Adv Mater* 12:298
33. Cui Y, Duan XF, Hu JT, Lieber CM (2000) Doping and electrical transport in silicon nanowires. *J Phys Chem B* 104:5213
34. Yang PD et al (2002) Controlled growth of ZnO nanowires and their optical properties. *Adv Funct Mater* 12:323
35. Hu JT, Ouyang M, Yang PD, Lieber CM (1999) Controlled growth and electrical properties of heterojunctions of carbon nanotubes and silicon nanowires. *Nature* 399:48
36. Huang Y et al (2001) Logic gates and computation from assembled nanowire building blocks. *Science* 294:1313
37. Gudiksen MS, Lieber CM (2000) Diameter-selective synthesis of semiconductor nanowires. *J Am Chem Soc* 122:8801
38. Zheng GF, Lu W, Jin S, Lieber CM (2004) Synthesis and fabrication of high-performance n-type silicon nanowire transistors. *Adv Mater* 16:1890

39. Zhong ZH, Qian F, Wang DL, Lieber CM (2003) Synthesis of p-type gallium nitride nanowires for electronic and photonic nanodevices. *Nano Lett* 3:343
40. Yang C, Zhong ZH, Lieber CM (2005) Encoding electronic properties by synthesis of axial modulation-doped silicon nanowires. *Science* 310:1304
41. Gudiksen MS, Lauhon LJ, Wang J, Smith DC, Lieber CM (2002) Growth of nanowire superlattice structures for nanoscale photonics and electronics. *Nature* 415:617
42. Lauhon LJ, Gudiksen MS, Wang CL, Lieber CM (2002) Epitaxial core-shell and core-multishell nanowire heterostructures. *Nature* 420:57
43. Wang D, Qian F, Yang C, Zhong ZH, Lieber CM (2004) Rational growth of branched and hyperbranched nanowire structures. *Nano Lett* 4:871
44. Tian BZ, Xie P, Kempa TJ, Bell DC, Lieber CM (2009) Single-crystalline kinked semiconductor nanowire superstructures. *Nat Nanotechnol* 4:824
45. Xiang J et al (2006) High performance field effect transistors based on Ge/Si nanowire heterostructures. *Nature* 441:489
46. Lu W, Lieber CMJ (2006) Semiconductor nanowires. *Phys D-Appl Phys* 39:R387
47. Yan H et al (2011) Programmable nanowire circuits for nanoprocessors. *Nature* 470:240
48. Yao J, Yan H, Das S, Klemic J, Ellenbogen J, Lieber CM (2014) Nanowire nanocomputer as a finite-state machine. *Proc Natl Acad Sci U S A* 111:2431
49. Duan XF, Lieber CM (2000) Laser-assisted catalytic growth of single crystal GaN nanowires. *J Am Chem Soc* 122:188
50. Liu JL, Cai SJ, Jin GL, Thomas SG, Wang KL (1999) Growth of Si whiskers on Au/Si (111) substrate by gas source molecular beam epitaxy (MBE). *J Cryst Growth* 200:106
51. Wu YY, Yang PD (2001) Direct observation of vapor- liquid- solid nanowire growth. *J Am Chem Soc* 123:3165
52. Wu Y et al (2004) Controlled growth and structures of molecular-scale silicon nanowires. *Nano Lett* 4:433
53. Hansen M, Anderko K (1958) Constitution of binary alloys. McGraw-Hill
54. Tian B et al (2007) Coaxial silicon nanowires as solar cells and nanoelectronic power sources. *Nature* 449:885
55. Jiang X et al (2011) Rational growth of branched nanowire heterostructures with synthetically encoded properties and function. *Proc Natl Acad Sci U S A* 108:12212
56. Fortuna SA, Li X (2009) GaAs MESFET with a high-mobility self-assembled planar nanowire channel. *IEEE Electron Device Lett* 30:593
57. Jiang X, Xiong Q, Nam S, Qian F, Li Y, Lieber CM (2007) InAs/InP radial nanowire heterostructures as high electron mobility devices. *Nano Lett* 7:3214
58. Duan XF, Niu CM, Sahi V, Chen J, Parce JW, Empedocles S, Goldman JL (2003) High-performance thin-film transistors using semiconductor nanowires and nanoribbons. *Nature* 425:274
59. Huang Y, Duan XF, Wei QQ, Lieber CM (2001) Directed assembly of one-dimensional nanostructures into functional networks. *Science* 291:630
60. Yu G, Cao A, Lieber CM (2007) *Nat Nanotechnol* 2:372
61. Tao AR, Huang J, Yang P (2008) Large-area blown bubble films of aligned nanowires and carbon nanotubes. *Acc Chem Res* 41:1662
62. Wang DW, Chang YL, Liu Z, Dai H (2005) Oxidation resistant germanium nanowires: bulk synthesis, long chain alkanethiol functionalization, and Langmuir-Blodgett assembly. *J Am Chem Soc* 127:11871
63. Fan Z et al (2008) Wafer-scale assembly of highly ordered semiconductor nanowire arrays by contact printing. *Nano Lett* 8:20
64. Javey A, Nam S, Friedman RS, Yan H, Lieber CM (2007) Layer-by-layer assembly of nanowires for three-dimensional, multifunctional electronics. *Nano Lett* 7:773
65. Nam S, Jiang X, Xiong Q, Ham D, Lieber CM (2009) Vertically integrated, three-dimensional nanowire complementary metal-oxide-semiconductor circuits. *Proc Natl Acad Sci U S A* 106:21035

66. McAlpine MC, Ahmad H, Wang D, Heath JR (2007) Highly ordered nanowire arrays on plastic substrates for ultrasensitive flexible chemical sensors. *Nat Mater* 6:379
67. Timko BP et al (2009) Electrical recording from hearts with flexible nanowire device arrays. *Nano Lett* 9:914
68. Takei K et al (2010) Nanowire active-matrix circuitry for low-voltage macroscale artificial skin. *Nat Mater* 9:821
69. Yao J, Yan H, Lieber CM (2013) A nanoscale combing technique for the large-scale assembly of highly aligned nanowires. *Nat Nanotechnol* 8:329
70. Ahn JH et al (2006) Heterogeneous three-dimensional electronics by use of printed semiconductor nanomaterials. *Science* 314:1754
71. Zheng GF, Patolsky F, Cui Y, Wang WU, Lieber CM (2005) Multiplexed electrical detection of cancer markers with nanowire sensor arrays. *Nat Biotechnol* 23:1294
72. Venkatesan BM, Bashir R (2011) Nanopore sensors for nucleic acid analysis. *Nat Nanotechnol* 6:615
73. Rothberg JM et al (2011) An integrated semiconductor device enabling non-optical genome sequencing. *Nature* 475:348
74. Hille B (2001) *Ion channels of excitable membranes*. Sinauer Associates, Inc.
75. Zipes DP, Jalife J (2004) *Cardiac electrophysiology: from cell to bedside*. Saunders
76. Dhein S, Mohr FW, Delmar M (2005) *Practical methods in cardiovascular research*. Springer, Berlin
77. Davie JT et al (2006) Dendritic patch-clamp recording. *Nat Protocols* 1:1235
78. Halbach MD, Egert U, Hescheler J, Banach K (2003) Estimation of action potential changes from field potential recordings in multicellular mouse cardiac myocyte cultures. *Cell Physiol Biochem* 13:271
79. Meyer T, Boven KH, Gunther E, Fejtl M (2004) Micro-electrode arrays in cardiac safety pharmacology: a novel tool to study QT interval prolongation. *Drug Saf* 27:763
80. Erickson J, Tooker A, Tai YC, Pine J (2008) Caged neuron MEA: A system for long-term investigation of cultured neural network connectivity. *J Neurosci Method* 175:1
81. Law JKY et al (2009) The use of microelectrode array (MEA) to study the protective effects of potassium channel openers on metabolically compromised HL-1 cardiomyocytes. *Physiol Meas* 30:155
82. Ingebrandt S, Yeung C-K, Krause M, Offenhausser A (2001) Cardiomyocyte-transistor-hybrids for sensor application. *Biosens Bioelectron* 16:565
83. Yeung C-K, Ingebrandt S, Krause M, Offenhausser A, Knoll W (2001) Validation of the use of field effect transistors for extracellular signal recording in pharmacological bioassays. *J Pharmacol Toxicol Meth* 45:207
84. Cohen A, Shappir J, Yitzchiak S, Spira ME (2006) Experimental and theoretical analysis of neuron-transistor hybrid electrical coupling: the relationships between the electro-anatomy of cultured Aplysia neurons and the recorded field potentials. *Biosens Bioelectron* 22:656
85. Cohen A, Shappir J, Yitzchaik S, Spira ME (2008) Experimental and theoretical analysis of neuron-transistor hybrid electrical coupling: the relationships between the electro-anatomy of cultured Aplysia neurons and the recorded field potentials. *Biosens Bioelectron* 23:811
86. Lu Z-L et al (2004) Electrocardiography in adult congenital heart disease. *Electrocardiology* 14:11
87. Reppel M et al (2004) Microelectrode arrays: a new tool to measure embryonic heart activity. *J Electrocardiol* 37:104
88. Fromherz P (2002) Electrical interfacing of nerve cells and semiconductor chips. *ChemPhysChem* 2:276
89. Spira ME, Hai A (2013) Multi-electrode array technologies for neuroscience and cardiology. *Nat Nanotechnol* 8:83
90. Xie C, Lin Z, Hanson L, Cui Y, Cui B (2012) Intracellular recording of action potentials by nanopillar electroporation. *Nat Nanotechnol* 7:185
91. Robinson JT et al (2012) Vertical nanowire electrode arrays as a scalable platform for intracellular interfacing to neuronal circuits. *Nat Nanotechnol* 7:180

92. Cui Y, Wei Q, Park H, Lieber CM (2001) Nanowire nanosensors for highly sensitive and selective detection of biological and chemical species. *Science* 293:1289
93. Duan X et al (2012) Intracellular recordings of action potentials by an extracellular nanoscale field-effect transistor. *Nat Nanotechnol* 7:174
94. Gao R et al (2012) Outside looking in: nanotube transistor intracellular sensors. *Nano Lett* 12:3329
95. Qing Q, Jiang Z, Xu L, Gao R, Mai L, Lieber CM (2014) Free-standing kinked nanowire transistor probes for targeted intracellular recording in three dimensions. *Nat Nanotechnol* 9:142
96. Jiang Z, Qing Q, Xie P, Gao R, Lieber CM (2012) Kinked p-n junction nanowire probes for high spatial resolution sensing and intracellular recording. *Nano Lett* 12:1711
97. Shalek AK et al (2010) Vertical silicon nanowires as a universal platform for delivering biomolecules into living cells. *Proc Natl Acad Sci U S A* 107:1870
98. Shalek AK et al (2012) Nanowire-mediated delivery enables functional interrogation of primary immune cells: application to the analysis of chronic lymphocytic leukemia. *Nano Lett* 12:6498
99. Yosef N et al (2013) Dynamic regulatory network controlling TH17 cell differentiation. *Nature* 496:461
100. Empedocles SA, Bawendi MG (1997) Quantum-confined stark effect in single CdSe nanocrystallite quantum dots. *Science* 278:2114
101. Michalet X et al (2005) Quantum dots for live cells, in vivo imaging, and diagnostics. *Science* 307:538
102. Langer R (1998) Drug delivery and targeting. *Nature* 392:5
103. Farokhzad OC, Langer R (2009) Impact of nanotechnology on drug delivery. *ACS Nano* 3:16
104. Retterer ST et al (2004) Model neural prostheses with integrated microfluidics: a potential intervention strategy for controlling reactive cell and tissue responses. *IEEE Trans Biomed Eng* 51:2063
105. Dvir T, Timko BP, Kohane DS, Langer R (2011) Nanotechnological strategies for engineering complex tissues. *Nat Nanotechnol* 6:13
106. Viventi J et al (2010) A conformal, bio-interfaced class of silicon electronics for mapping cardiac electrophysiology. *Sci Transl Med* 2:24ra22
107. Viventi J et al (2011) Flexible, foldable, actively multiplexed, high-density electrode array for mapping brain activity in vivo. *Nat Neurosci* 14:1599
108. Denk W, Strickler JH, Webb WW (1990) Two-photon laser scanning fluorescence microscopy. *Science* 248:73
109. Jones K, Campbell P, Normann R (1992) A glass/silicon composite intracortical electrode array. *Ann Biomed Eng* 20:423
110. Bradley K (2006) The technology: the anatomy of a spinal cord and nerve root stimulator: the lead and the power source. *Pain Med* 7:S27
111. Harnack D et al (2004) The effects of electrode material, charge density and stimulation duration on the safety of high-frequency stimulation of the subthalamic nucleus in rats. *J Neurosci Meth* 138:207
112. Kerns JM, Fakhouri AJ, Weinrib HP, Freeman JA (1991) Electrical stimulation of nerve regeneration in the rat: the early effects evaluated by a vibrating probe and electron microscopy. *Neuroscience* 40:93
113. Merrill DR, Bikson M, Jefferys JGR (2005) Electrical stimulation of excitable tissue: design of efficacious and safe protocols. *J Neurosci Meth* 141:171
114. Alivisatos AP et al (2012) The brain activity map project and the challenge of functional connectomics. *Neuron* 74:970
115. Alivisatos AP et al (2013) Nanotools for neuroscience and brain activity mapping. *ACS Nano* 7:1850

116. Ionescu LC, Lee GC, Sennett BJ, Burdick JA, Mauck RL (2010) An anisotropic nanofiber/microsphere composite with controlled release of biomolecules for fibrous tissue engineering. *Biomaterials* 31:4113
117. Cao HQ, Jiang X, Chai C, Chew SYJ (2010) RNA interference by nanofiber-based siRNA delivery system. *Cont Release* 144:203
118. Deisseroth K (2012) Optogenetics and psychiatry: applications, challenges, and opportunities. *Biol Psychiatry* 71:1030
119. Zamft BM et al (2012) Measuring cation dependent DNA polymerase fidelity landscapes by deep sequencing. *PLoS ONE* 7:e43876
120. Lee JH et al (2014) Highly multiplexed subcellular RNA sequencing in situ. *Science* 343:1360

Chapter 2

Three-Dimensional Macroporous Nanoelectronics Network

2.1 Introduction

Seamlessly merging functional electronic circuits as embedded systems in a minimally-invasive manner with host materials in 3D could serve as a pathway for creating “very smart” systems because those embedded systems would transform conventional inactive materials into active systems. The embedded electronic sensor circuitry could monitor chemical and physical changes throughout a host material, thus providing detailed information about the host material’s response to external environments as well as desired feedback to the host and external environment [1, 2]. To achieve this goal, the addressable electronics should be firstly macroporous, not planar, to enable 3D interpenetrations with the host materials. Second, to minimize invasiveness of the macroporous electronic network it must have (1) microscale to nanoscale feature sizes, (2) a small filling fraction with respect to the host (e.g., $\leq 1\%$), (3) comparable or softer mechanical properties than the host, and (4) an inert chemical response within the host material.

The constraints outlined above require the utilization of 3D nanoelectronic networks that are macroporous and have active elements (nanodevices). Previously, two basic methods have been used to fabricate 3D integrated electronic circuits. The first involves bonding 2D substrates, each containing 2D devices/circuits network, together in a 3D stack [3, 4]. The second exploits bottom-up assembly of nanoelectronic elements in a layer-by-layer manner [5, 6]. However, both methods yield solid or nonporous 3D structures that only allow the top-most layer of electronic elements to be interfaced directly with a second material/object and thus precluding integration of all of the electronic elements seamlessly with a host material in 3D. Here, we introduce a general mechanics-driven strategy for patterning macroporous nanoelectronic networks that contains regular arrays of addressable nanowire nanoelectronic elements in 3D structure.

2.2 Experimental

2.2.1 3D Macroporous Nanowire Nanoelectronic Network Fabrication

Uniform 30 nm p-type single-crystalline silicon nanowires were synthesized as report [7, 8]. The 3D macroporous nanowire nanoelectronic networks were initially fabricated on the oxide or nitride surfaces of silicon substrates prior to relief from the substrate. A mechanics-driven fabrication process was (Fig. 2.1) used in the fabrication of the 3D macroporous nanowire nanoelectronic networks that were reported in ref 2 and 7 briefly: (1) lithography and thermal deposition were used to pattern nickel metal relief layer for the 2D free-standing macroporous nanowire

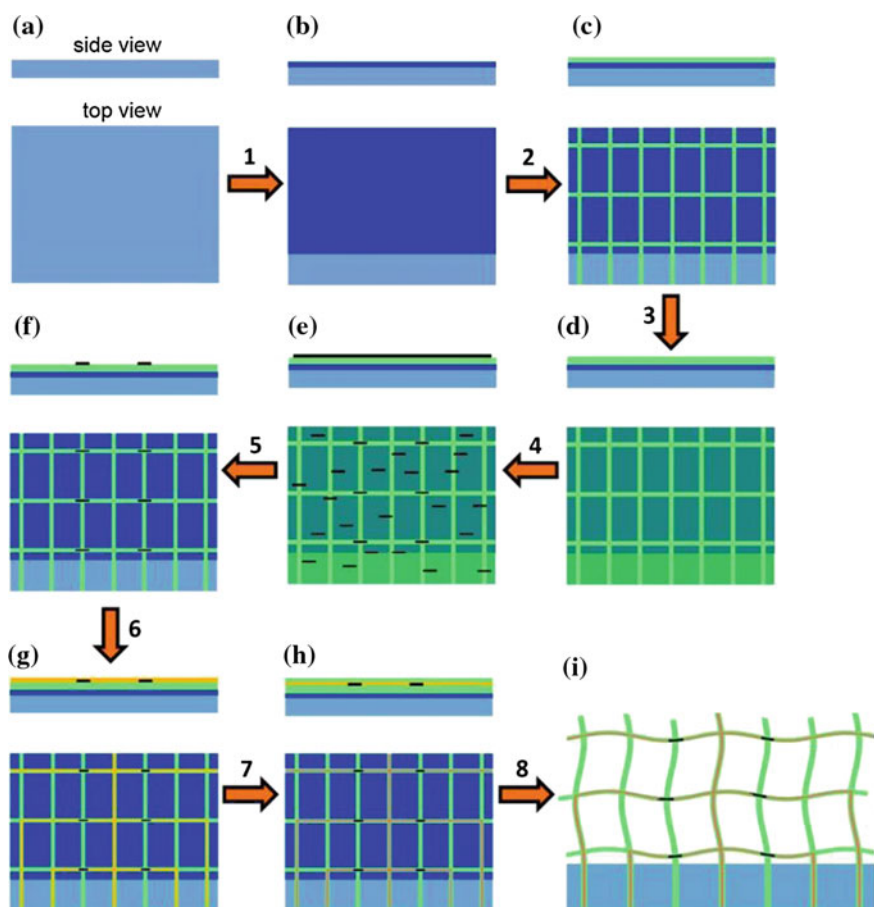


Fig. 2.1 Schematic of macroporous nanoelectronics fabrication. Components include silicon wafer (cyan), nickel sacrificial layer (blue), polymer (green), metal interconnects (gold) and silicon nanowires (black)

nanoelectronic networks. (2) A 300–500 nm layer of SU-8 photoresist was deposited over the entire chip, then (3) the synthesized nanowires were directly printed from growth wafer over the SU-8 layer by the contact printing methods reported previously [6]. (4) Lithography (photolithography or electron beam lithography) was used to define regular patterns on the SU-8. Those nanowires on the non-exposed area will be removed by washing away in SU-8 developer and isopropanol solution for leaving those selected nanowires on the regular pattern SU-8 structure. (5) A second 300–500 nm layer of SU-8 photoresist was deposited over the entire chip. Then lithography was used to pattern the bottom SU-8 layer for passivating and supporting the whole device structure. (6) Lithography and thermal deposition were used to define and deposit the metal contact to address each nanowire device and form interconnections to the input/output pads for the array. (7) A third 300–500 nm layer of SU-8 photoresist was deposited over the entire chip. Then lithography was used to pattern the top SU-8 layer for passivating the whole device structure. (8) The 2D macroporous nanowire nanoelectronic networks were released from the substrate by etching of the nickel layer. (9) The 3D macroporous nanowire nanoelectronic networks were dried by a critical point dryer and stored in the dry state prior to use.

2.2.2 Three-Layer Interconnect Ribbon for Mechanical Simulation

SU-8/metal/SU-8 ribbons with 100 μm long and 5 μm wide segments over the Ni-layer and wider segments directly on substrate were defined by EBL using the same approach described above. A schematic and an optical image of the resulting sample element are shown in Fig. 2.2a, b, respectively. An atomic force microscope was used to measure force versus displacement curves for the ribbon (Fig. 2.2c). The spring constant of the AFM cantilever/tip assemblies used in the measurements were calibrated by measuring the thermal vibration spectrum [9].

The self-organization of the macroporous structure due to residual stress was simulated by the commercial finite element software ABAQUS. Ribbons were modeled as beam elements. The equivalent bending moment on SU-8/metal ribbons was calculated using the residual stress measured by MET-1 FLX-2320-S thin film stress measurement system, which were 1.35 and 0.12 Gpa for Cr (50 nm) and Pd (75 nm), respectively.

2.2.3 Characterization and Measurement of Macroporous Nanoelectronics

Scanning electron microscopy (SEM), Bright-field and dark-field optical microscopy, and confocal fluorescence microscopy were used to characterize the

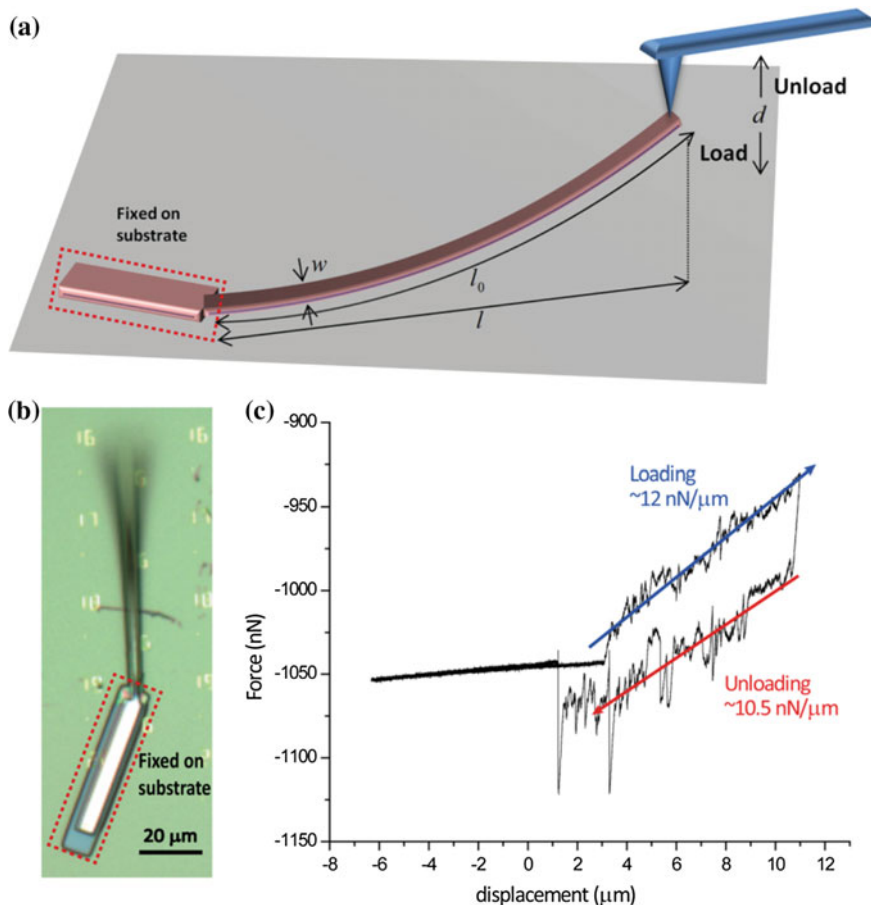


Fig. 2.2 Bending stiffness measurements. **a** Schematic illustrating the measurement of the bending stiffness of a representative SU-8/metal/SU-8 ribbon in the macroporous nanoelectronic networks. The tip of the AFM is placed at the free end of the ribbon, and then translated vertically downward (loading) and upward (unloading) to yield the force-displacement curves. In the scheme, w : the width of the ribbon, l_0 : the length of the ribbon, l : the projected length of the ribbon and d : the displacement of the AFM tip. **b** Optical micrograph of the fabricated structural element, where the substrate fixed portion is highlighted by the red dashed rectangle and the free beam is in the upper portion of the image with a width of $5\ \mu\text{m}$ and a length of $100\ \mu\text{m}$. **c** A typical force—displacement curve with F/d for loading and unloading of 12 and $10.5\ \text{nN}/\mu\text{m}$, respectively

macroporous nanoelectronic networks. *ImageJ* (ver. 1.45i) was used for 3D reconstruction and analysis of the confocal and epi-fluorescence images.

Silicon nanowire device in the 3D macroporous nanoelectronic network recording was carried out with a $100\ \text{mV}$ DC source voltage. The current was amplified by a home-built multi-channel current/voltage preamplifier with a typical gain of $10^6\ \text{A/V}$. The amplified signals were filtered through a home-built conditioner with band-pass of $0\text{--}3\ \text{kHz}$, digitized at a sampling rate of $20\ \text{kHz}$ and

recorded using Clampex 10 software. The nanowire FET conductance and transconductance (sensitivity) were measured and calculated in $1 \times \text{PBS}$ as described previously [10].

2.3 Results and Discussion

2.3.1 3D Macroporous Nanoelectronic Network

We combine both “bottom-up” and mechanics-driven approaches to realize 3D macroporous nanoelectronic networks (Fig. 2.3). In this approach, we utilize functional nanowires as nanoelectronic elements (Fig. 2.3a). The variations of nanowires in composition, morphology and doping encoded during synthesis [11–19] define diverse functionality including devices for logic and memory [20, 21], sensors [18, 23], light-emitting diodes [17], and energy production and storage [24, 25]. Through a combination of nanowire assembly and conventional 2D lithography carried out on a sacrificial substrate (see below), we can first realize 2D mesh nanoelectronic networks with multiple functions. Then, we remove the sacrificial layer to yield a free-standing and flexible 2D mesh nanoelectronic network as precursor for 3D macroporous electronics (Fig. 2.3b). Third, we implemented internal stress into the metal interconnects of 2D mesh electronic network during fabrication. This stress, due to its designed distribution, creates forces to organize the freestanding 2D mesh nanoelectronic precursor into a regular 3D macroporous structure.

The key steps for this “bottom-up” fabrication process are outlined in Fig. 2.4. First, nanowires were uniaxially-aligned by contact printing [14] on the surface of a layer of SU-8 negative resist (Fig. 2.4a, I). Second, the SU-8 layer with aligned nanowires was patterned to define a periodic array by lithography, and the excess nanowires on unexposed regions of the SU-8 were removed when the pattern was developed (Fig. 2.4a, II). The nanowire density and feature size in periodic arrays

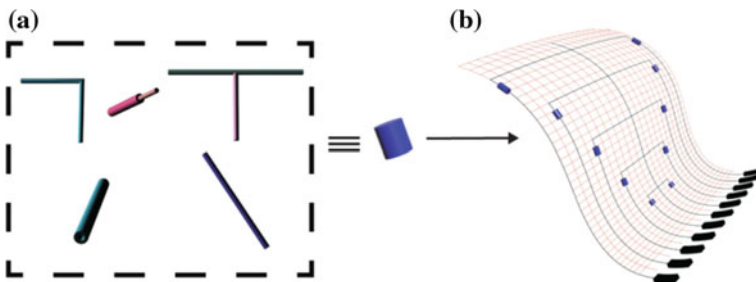
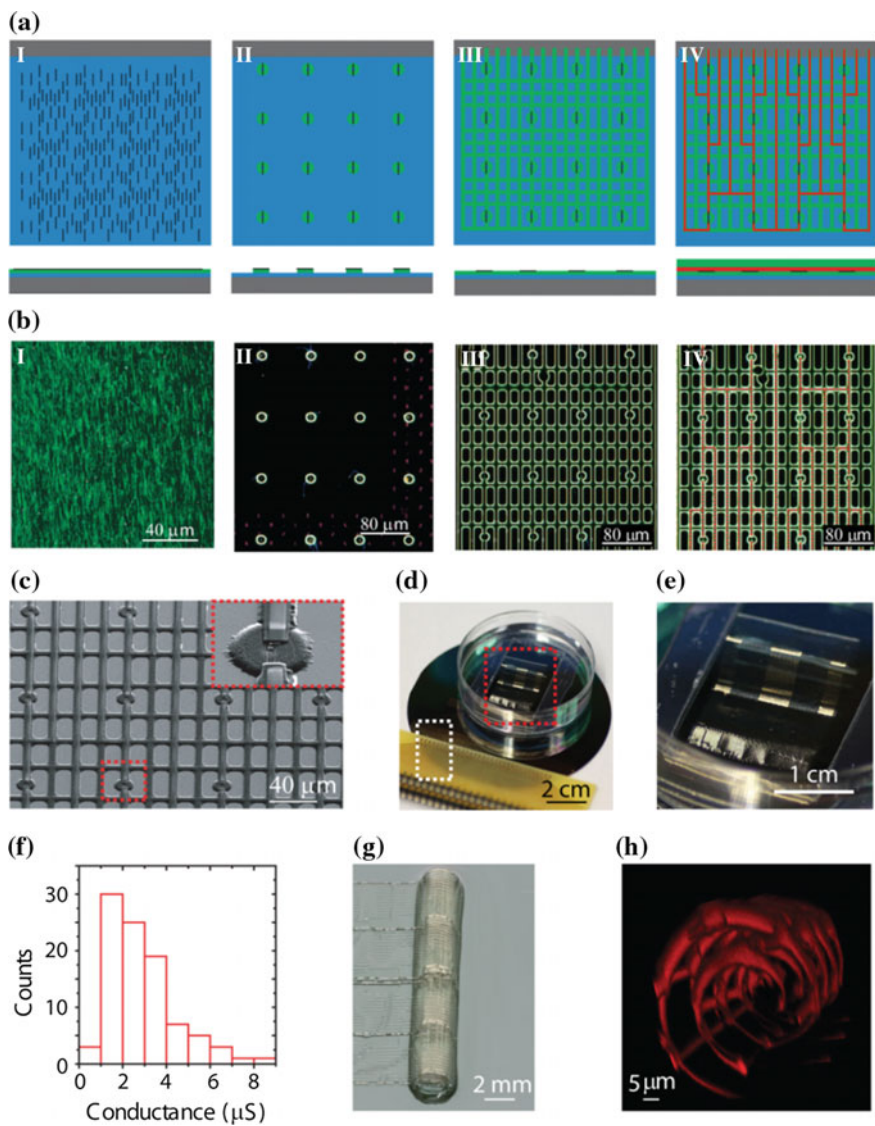


Fig. 2.3 Strategy for preparing 3D macroporous nanoelectronic networks. **a** Different nanowire nanoelectronic elements such as kinked nanowire, nanotube, core-shell, straight and branched nanowire. **b** Freestanding 2D macroporous nanowire nanoelectronic “precursor”. Blue: nanoelectronic element, orange: passivation polymer, black: metal contact and input/output (I/O)



◀**Fig. 2.4** Organized 2D and 3D macroporous nanoelectronic networks. **a** Schematics of nanowire registration by contact printing and SU-8 patterning. Gray: Silicon wafer, blue: Ni sacrificial layer, black ribbon: nanowire, green: SU-8, red: metal contact. (Top) shows top view and (bottom) shows side view. **(I)** Contact printing nanowire on SU-8. **(II)** Regular SU-8 structure was patterned by lithography to immobilize nanowires. Extra nanowires were washed away during the develop process of SU-8. **(III)** Regular bottom SU-8 structure was patterned by spin-coating and lithography. **(IV)** Regular metal contact was patterned by lithography and thermal evaporation, followed by top SU-8 passivation. **b** Dark field optical images corresponding to each step of schematics in **(a)**. **c** SEM image of a 2D macroporous nanoelectronic network prior to release from the substrate. Inset, corresponds to zoom-in of the region enclosed by the red dashed box containing a single nanowire device. **d** Photograph of wire-bonded free-standing 2D macroporous nanoelectronic network in petri-dish chamber for aqueous solution measurements. The red dashed box highlights the free-standing portion of the nanoelectronic network and the white-dashed box encloses the wire-bonded interface between the input/output (I/O) and PCB connector board. **e** Zoom-in of the region enclosed by the red-dashed box in **(d)**. **f** Histogram nanowire device conductance in the free-standing 2D macroporous nanoelectronic networks. **g** Photograph of a manually scrolled-up 3D macroporous nanoelectronic network. **h** 3D reconstructed confocal fluorescence images of a representative self-organized 3D macroporous nanoelectronic network viewed along the x-axis

were chosen such that each element contained on average 1–2 nanowires. Third, a second SU-8 layer was deposited and patterned in a mesh structure by lithography (Fig. 2.4a, III). This SU-8 mesh serves to interconnect the nanowire/SU-8 periodic features and provides an adjustable support structure to tune the mechanical properties. Fourth, metal interconnects were defined by standard lithography and metal deposition on top of the appropriate regions of the SU-8 mesh, such that the end of nanowires were contacted and the nanowire elements were independently addressable (Fig. 2.4a, IV). Last, a third SU-8 layer was lithographically patterned to cover and passivate the metal interconnects.

Dark-field optical microscopy images obtained from a typical nanoelectronic network fabrication corresponding to the steps described above (Fig. 2.4b) highlight several important features. First, the images recorded after contact printing (Fig. 2.4b, I) confirm that nanowires are well-aligned over areas where nanowire devices are fabricated. We can achieve good nanowire alignment on length scales up to at least several centimeters as reported elsewhere [6, 7, 14]. Second, a representative dark-field image of the patterned periodic nanowire regions (Fig. 2.4b, II) shows that this process removes nearly all of the nanowires outside of the desired features. Nanowires can be observed to extend outside of the periodic circular feature (i.e., an end is fixed at the feature) at some points; however, these are infrequent and do not affect subsequent steps defining the nanodevice interconnections. Third, images of the underlying SU-8 mesh (Fig. 2.4b, III) and final device network with SU-8 passivated metal contacts and interconnects (Fig. 2.4b, IV) highlight the regular array of addressable nanowire devices realized in our fabrication process. Last, scanning electron microscopy (SEM) images (Fig. 2.4c) show that these device elements have on average 1–2 nanowires in parallel.

The 2D macroporous nanoelectronic structures were converted to free-standing macroporous networks by dissolution of the sacrificial Ni layers over a period of 1–

2 h (ref 7). Representative images of a free-standing nanoelectronic network (Fig. 2.4d, e) highlight the 3D and flexible characteristics of the structure and show how input/output (I/O) to the free-standing network can be fixed at one end outside of a solution measurement petri-dish chamber. Electrical characterization of individually-addressable nanowire device elements in a free-standing mesh demonstrates that the device-yield is typically $\sim 90\%$ (from 128 device design) for the free-standing nanoelectronic mesh structures fabricated in this way. The average conductance of the devices from a representative free-standing mesh (Fig. 2.4f), $2.85 \pm 1.6 \mu\text{S}$, is consistent with 1–2 nanowires/device based on measurements of similar (30 nm diameter, 2 μm channel length) *p*-type Si single nanowire devices [26], and thus also agrees with the structural data discussed above. In addition, by varying the printed nanowire density and S/D metal contact widths, it is possible to tune further the average number of nanowires per device element.

These 2D freestanding macroporous nanoelectronic networks can be transformed into 3D structures by manually rolled-up into 3D arrays (Fig. 2.4g). To better control the microstructure of the 3D macroporous structure, a mechanics-driven approach was demonstrated through introducing built-in stress in metal interconnects with a tri-layer metal stack, which self-organize the 2D macroporous network into a scrolled structure [13, 27]. Importantly, the reconstructed 3D confocal fluorescent image of a 3D macroporous nanoelectronic network produced in this manner (Fig. 2.4h) shows a clearly scrolled 3D structure that separate each layer of nanowire devices and distribute the nanowire devices evenly in 3D space with a $>99\%$ free volume. More generally, these mechanics-driven 3D macroporous nanoelectronic structures could be readily diversified to meet goals for different hybrid materials using established mechanical design and bifurcation strategies [28].

2.3.2 Mechanics Analysis

The 3D macroporous nanoelectronic networks consist of single-layer polymer (SU-8) structural and three-layer ribbon (SU-8/metal/SU-8) interconnect elements. The effective bending stiffness per unit width of the 3D macroporous nanoelectronic networks can be estimated [29] by Eq. (2.1)

$$\bar{D} = \alpha_s D_s + \alpha_m D_m \quad (2.1)$$

where α_s and α_m are the area fraction of the single-layer polymer and three-layer interconnect ribbons in the networks. $D_s = E_s h^3/12$ is the bending stiffness per unit width of the single-layer polymer, where $E_s = 2 \text{ GPa}$ and h are the modulus and thickness of the SU-8. For a SU-8 ribbon with 500 nm thickness, D_s is 0.02 nN m. D_m is the bending stiffness per unit width of a three-layer structure, which includes 500 nm lower and upper SU-8 layers and 100–130 nm metal layer, and was measured experimentally as described below and shown in Fig. 2.2.

Qualitatively, the facile manipulation of the macroporous nanoelectronic networks to form 3D structures suggests a very low effective bending stiffness. We have evaluated the effective bending stiffness, \bar{D} , using a combination of calculations and experimental measurements. Due to the residual stress, the SU-8/metal/SU-8 elements bend upward from the substrate (due to internal stress of the asymmetric metal layers) with a constant curvature, K_0 , and projected length, l , where l_0 is the free length defined by fabrication. We use the curvilinear coordinate, s , to describe the distance along the curved ribbon from the fixed end, and the coordinate, χ , to describe the projection position of each material point of the ribbon (Fig. 2.5a). For a specific material point with distance s , the projection position χ can be calculated as $x = \int \cos \psi ds$, where $\psi = K_0 s$ is the angle between the tangential direction of the curvilinear coordinate s and the horizontal direction (Fig. 2.5b). Integration yields $x = \sin(K_0 s)/K_0$ and when $\chi = l$ and $s = l_0$, $K_0 = 0.0128 \mu\text{m}^{-1}$ for typical experimental parameters $l_0 = 100 \mu\text{m}$ and $l = 75 \mu\text{m}$.

As the element is deflected a distance, d , by the AFM tip with a force, F , each material point is rotated by an angle, φ , (Fig. 2.5b), where the anti-clockwise direction is defined as positive. Assuming a linear constitutive relation between the moment M and curvature change $d\varphi/ds$ [30] yields

$$\frac{d\varphi}{ds} = \frac{M}{wD_m} \quad (2.2)$$

where M is the moment as a function of position, x (Fig. 2.5), and w is the width.

$$M(x) = -F(l - x) \quad (2.3)$$

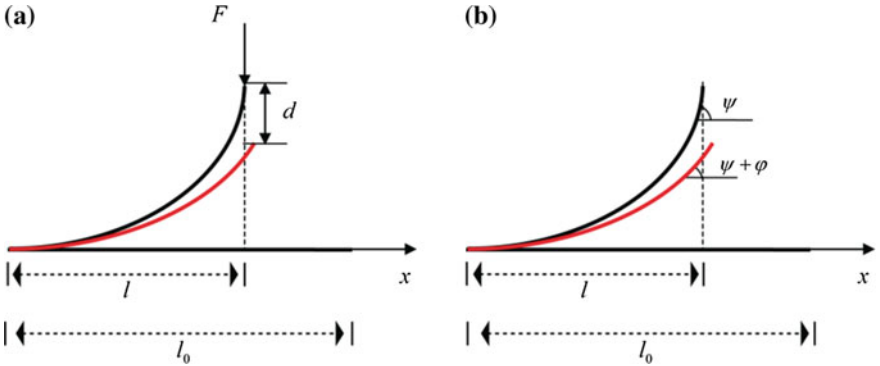


Fig. 2.5 Schematics for bending stiffness calculation. **a** A schematic of the position of the substrate free beam before (black) and after (red) applying a calibrated force, F , and vertical displacement, d , at the end of the beam with the AFM. **b** The angle between the tangential direction of a material point on the beam and the horizontal direction, ψ , of the ribbon before (black) and after displacement, $\psi + \varphi$, (red). l_0 : the total length of the ribbon. l : projection of the ribbon

Solving for the bending stiffness, D_m , with the assumption that φ is small so that $\sin \varphi \approx \varphi$ yields:

$$D_m = \frac{F}{wd} \left(\frac{ll_0 \sin(K_0 l_0)}{K_0} + \frac{1}{K_0^2} \left(l \cos(K_0 l_0) - l + \frac{l_0}{2} \right) + \frac{1}{K_0^3} \left(\frac{\sin(2K_0 l_0)}{4} - \sin(K_0 l_0) \right) \right) \quad (2.4)$$

The slope of a representative loading force-deflection curve, yields $F/d = 12 \text{ nN}/\mu\text{m}$ (Fig. 2.2c), and using Eq. (2.4) the calculated bending stiffness per width ($w = 5 \mu\text{m}$) is $D_m = 0.358 \text{ nN m}$. For typical 3D macroporous nanoelectronic networks the area fraction for both types of elements (i.e., SU-8 and SU-8/metal/SU-8) can range from 1 to 10%, yielding values of the effective bending stiffness from 0.0038 to 0.0378 nN m.

2.4 Conclusions

We have demonstrated a general strategy combining bottom-up and mechanics-driven approaches for preparing regular 3D interconnected and addressable macroporous nanoelectronic networks from 2D nanoelectronic “precursors” that are fabricated by conventional lithography. The 3D networks have porosities larger than 99%, contain 100’s of addressable nanowire devices, and have feature sizes from the 10 micron scale for electrical and structural interconnections to the 10 nm scale for the functional nanowire device elements. The network is extremely flexible with the bending stiffness from 0.0038 to 0.0378, which is the most flexible electronics reported.

Bibliography

1. Reuss RH, Hopper DG, Park JG (2006) Macroelectronics. *MRS Bull* 31:447
2. Tian B et al (2012) Macroporous nanowire nanoelectronic scaffolds for synthetic tissues. *Nat Mater* 11:986
3. Al-sarawi SF, Abbott D, Franzon PD (1998) A review of 3-D packaging technology. *IEEE Trans Compon Packag Manuf Technol* 21:2
4. Benkart P et al (2005) 3D chip stack technology using through-chip interconnects. *IEEE Des Test Comput* 22:512
5. Ahn JH et al (2006) Heterogeneous three-dimensional electronics by use of printed semiconductor nanomaterials. *Science* 314:1754
6. Javey A, Nam S, Friedman RS, Yan H, Lieber CM (2007) Layer-by-layer assembly of nanowires for three-dimensional, multifunctional electronics. *Nano Lett* 7:773
7. Liu J et al (2013) Multifunctional three-dimensional macroporous nanoelectronic networks for smart materials. *Proc Natl Acad Sci USA* 110:6694–6699
8. Wu Y et al (2004) Controlled growth and structures of molecular-scale silicon nanowires. *Nano Lett* 4:433

9. Butt HJ, Jaschke M (1995) Calculation of thermal noise in atomic force microscopy. *Nanotechnology* 6:1
10. Tian B et al (2010) Three-dimensional, flexible nanoscale field-effect transistors as localized bioprobes. *Science* 329:831
11. Yang C, Zhong ZH, Lieber CM (2005) Encoding electronic properties by synthesis of axial modulation-doped silicon nanowires. *Science* 310:1304
12. Tian BZ, Xie P, Kempa TJ, Bell DC, Lieber CM (2009) Single-crystalline kinked semiconductor nanowire superstructures. *Nat Nanotechnol* 4:824
13. Fan Z et al (2008) Wafer-scale assembly of highly ordered semiconductor nanowire arrays by contact printing. *Nano Lett* 8:20
14. Lu W, Lieber CM (2007) Nanoelectronics from the bottom up. *Nat Mater* 6:841
15. Lieber CM, Wang ZL (2007) Functional nanowires. *MRS Bull* 32:99
16. Qian F, Gradecak S, Li Y, Wen Y, Lieber CM (2005) Core/multishell nanowire heterostructures as multicolor, high-efficiency light-emitting diodes. *Nano Lett* 5:2287
17. Tian B et al (2007) Coaxial silicon nanowires as solar cells and nanoelectronic power sources. *Nature* 449:885
18. Gao R et al (2012) Outside looking in: nanotube transistor intracellular sensors. *Nano Lett* 12:3329
19. Jiang X et al (2011) Rational growth of branched nanowire heterostructures with synthetically encoded properties and function. *Proc Natl Acad Sci USA* 108:12212
20. Yan H et al (2011) Programmable nanowire circuits for nanoprocessors. *Nature* 470:240
21. Xiang J et al (2006) High performance field effect transistors based on Ge/Si nanowire heterostructures. *Nature* 441:489
22. Cui Y, Wei Q, Park H, Lieber CM (2001) Nanowire nanosensors for highly sensitive and selective detection of biological and chemical species. *Science* 293:1289
23. Qin Y, Wang XD, Wang ZL (2008) Microfibre-nanowire hybrid structure for energy scavenging. *Nature* 451:809
24. Chan CK et al (2008) High-performance lithium battery anodes using silicon nanowires. *Nat Nanotechnol* 3:31
25. Zheng GF, Patolsky F, Cui Y, Wang WU, Lieber CM (2005) Multiplexed electrical detection of cancer markers with nanowire sensor arrays. *Nat Biotechnol* 23:1294
26. Leong TG et al (2009) Tetherless thermobiochemically actuated microgrippers. *Proc Natl Acad Sci USA* 106:703
27. Freund LB (2000) Substrate curvature due to thin film mismatch strain in the nonlinear deformation range. *J Mech Phys Solids* 48:1159
28. Kim DH et al (2011) Epidermal electronics. *Science* 333:838
29. Landau LD, Lifshitz EM (1986) *Theory of elasticity*, 3rd edn, Elsevier, pp 67–73

Chapter 3

Integration of Three-Dimensional Macroporous Nanoelectronics with Materials

3.1 Introduction

Seamless integration of embedded multifunctional electronics with host materials could transfer inactive materials into active systems, which allow the communication between the materials and external environment, and create a smart system [1, 2]. Traditional electronics are planar and rigid, however, most materials and systems in our daily life are three-dimensional (3D) and non-planar. To overcome this issue, flexible electronics have been developed to cover on the surface of other systems [3–5]. However, those surface electronics are still not able to detect the property change through the entire materials in 3D and provide a full range of control. While we can insert rigid devices into some soft host materials, this process are typically invasive. In addition, the mechanical mismatch between inserted rigid electronics and soft materials could cause break and separation between them during further movement [6–8]. Therefore, it is important to develop an approach to seamlessly integrate flexible electronics with host materials. Herein, we introduce a general strategy to 3D integration of electronics described in Chap. 2 with host materials and also show how these embedded electronics in the host materials can form optically addressable electronic networks and map chemical and mechanical changes induced by the external environment in 3D.

3.2 Experimental

3.2.1 *Optically Addressable 3D Macroporous Nanoelectronic Network*

Confocal microscopy was used to characterize the 3D macroporous nanoelectronic network with silicon nanowires as functional units. The SU-8 structure was doped with Rhodamine 6G for fluorescence imaging. The macroporous nanoelectronic

network was immersed into deionized (DI) water, individual devices were biased with 100 mV. The photocurrent signal was amplified, bandpass filtered, and synchronized with laser scanning position using an analog signal input box. The conductance signal from the resulting images was read out by *image J*, and the data were analyzed and fitted by *OriginPro*.

3.2.2 3D Macroporous Chemical Sensors Network

Agarose was dissolved into DI water and made as 0.5%, and heated up to 100 °C. The gel was drop casting onto the device and cooled down to room temperature. 4',6-diamidino-2-phenylindole (DAPI) was used to dope the gel for the confocal 3D reconstructed imaging. A PDMS fluidic chamber with input/output tubing and Ag/AgCl electrodes was sealed with the silicon substrate and the device or device-gel hybrid using silicone elastomer glue. The recorded device signals were filtered with a bandpass filter of 0–300 Hz.

3.2.3 3D Macroporous Strain Sensors Network

A freestanding 2D macroporous nanoelectronic network was suspended in water, and placed on a thin piece of cured silicone elastomer sheet. The hybrid macroporous nanowire network/silicon elastomer was rolled into a cylinder, infiltrated with uncured silicone elastomer under vacuum, and cured at 70 °C for 4 h. The resulting hybrid nanoelectronic/elastomer cylinders had volumes of ca. 300 mm [3] with volume ratio of device/elastomer of <0.1%. The structure of the macroporous electronic network/elastomer hybrid was determined using a HMXST X-ray micro-CT system with a standard horizontal imaging axis cabinet. The piezoelectric response to strain of the nanowire devices was calibrated using a mechanical clamp device under tensile strain, where the strain was calculated from the length change of the cylindrical hybrid structure. The bending strain field was determined in experiments where the cylindrical hybrid structure, with calibrated nanowire strain sensors, was subject to random bending deflections.

3.3 Results and Discussion

3.3.1 Imaging Nanowire Device in 3D Structure

The 3D macroporous nanoelectronics discussed in Chap. 2 can seamlessly merged with host materials samples using a solution casting process (Fig. 3.1). The semiconductor nanowire as functional units in these electronics can display multiple sensory functionalities, including photon [9], chemical, biochemical, and

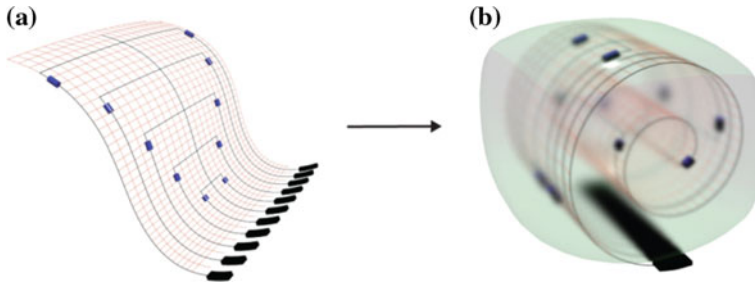


Fig. 3.1 Strategy for integration of 3D macroporous nanoelectronics with host materials. **a** Freestanding 2D macroporous nanowire nanoelectronic “precursor”. Blue: nanoelectronic element, orange: passivation polymer, black: metal contact and input/output (I/O). **b** 3D macroporous nanoelectronic networks integrated with host materials (Gray)

potentiometric [10, 11] as well as strain [12, 13] detection, which make them particularly attractive for preparing hybrid active materials. We have first characterized photoconductivity changes (i.e., photon detection) of nanowire elements (Figs. 3.2 and 3.3). As the focused laser is scanned across a sample (Fig. 3.2a, I), an increase of conductance due to the photocurrent [14] in semiconductor nanowire is recorded at the positions of the nanowire devices. We extend this approach as a general imaging technique to precisely determine the position of nanoelectronic sensing elements in a 3D network through imaging the nanoelectronic networks with a confocal microscope, recording photocurrent as a function of x-y-z coordinates and overlapping with simultaneously acquired fluorescence images. The resolution of this approach can be assessed in two ways. Conventionally, the plot of conductance versus position (Fig. 3.2a, II) can be fit with a Gaussian function and its full-width at half-maximum (FWHM) reflects the diffraction limited resolution of the illuminating light spot. Second and recognizing that the nanowire diameter (30 nm) is line-like; we can use methods similar to super-resolution imaging technologies [15, 16] to locate the nanowire to much higher precision by identifying the peak position from the Gaussian fit. We note that a similar concept as exploited in stochastic super-resolution fluorescence imaging to resolve close points can be implemented in our photoconductivity maps because individual semiconductor nanowire devices can be turned on and off as needed [15].

A typical high-resolution photoconductivity image of a single nanowire device (Fig. 3.2b, I) shows clearly the position of the nanowire. The conductance change versus x-position is perpendicular to the nanowire axis (Figs. 3.2b, II and 3.3b) yielding a FWHM is 314 ± 32 nm ($n = 20$) resolution consistent with confocal microscopy imaging resolution (202 nm) in this experiment. Moreover, the nanowire position determined from the peaks of Gaussian fits (Fig. 3.3c) yielded a standard deviation of 14 nm ($n = 20$), and shows that the position of devices can be localized with a precision better than the diffraction limit. In addition, we have acquired simultaneous photoconductivity and fluorescence confocal microscopy images to map the positions of nanowire devices in 3D macroporous nanoelectronic

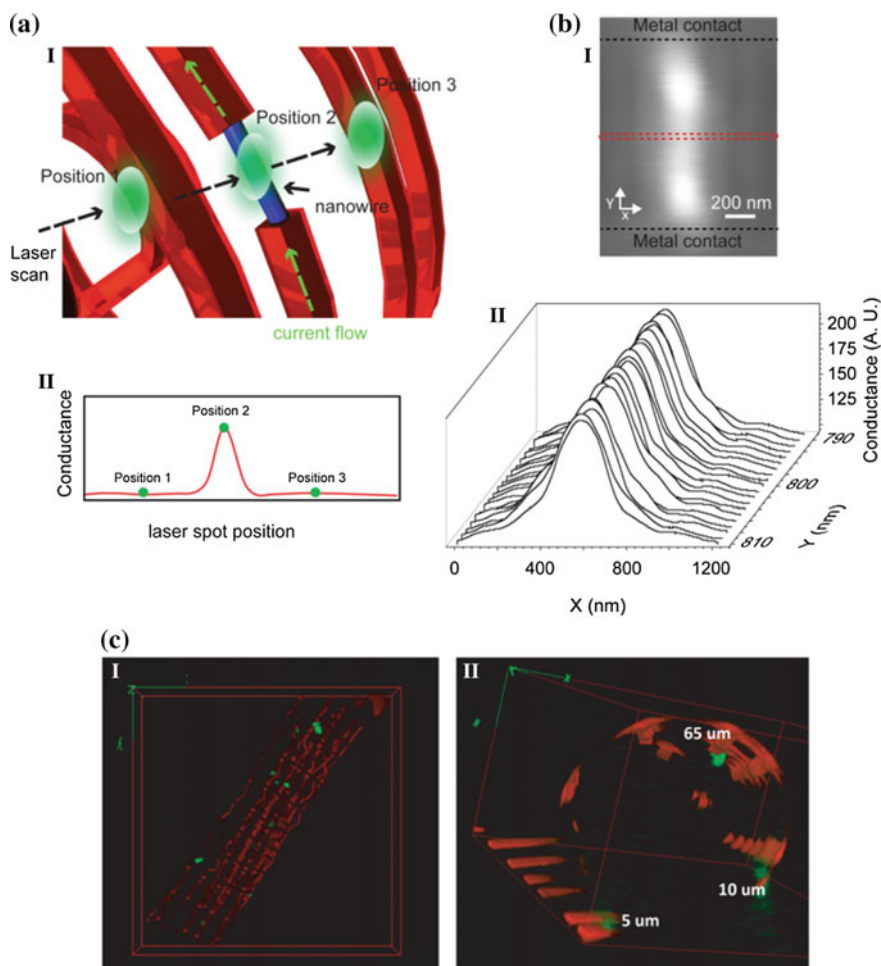


Fig. 3.2 3D macroporous photodetectors network and device localization. **a** Schematics of the single 3D macroporous nanowire photodetector characterization. The green ellipse: laser spot, blue cylinder: nanowire and orange: SU-8 mesh network. The illumination of the laser spot generated from confocal microscope on the nanowire device (**I**) makes the conductance change of nanowire, which could be (**II**) correlated with laser spot position. Green spots in (**II**) correlate to the laser spot positions in (**I**). **b** High-resolution (1 nm per pixel) photocurrent image (**I**) from single nanowire device (2 μm channel length) on substrate recorded with focused laser spot scanned in x-y plane. The black dash lines indicate the boundary of metal contact in the device. (**II**) 20 times photocurrent measurements from the central region (red dash box) of the nanowire device with high resolution (the distance for each trace in x-direction is 1 nm). **c** 3D reconstructed photocurrent imaging overlapped with confocal microscopy imaging shows the spatial correlation between nanowire photodetectors with SU-8 framework in 3D. Green: false color of the photocurrent signal, orange (rhodamine 6G): SU-8 mesh network. Dimensions in (**I**), x: 317 μm ; y: 317 μm ; z: 53 μm ; in (**II**), x: 127 μm ; y: 127 μm ; z: 65 μm . The white numbers in (**II**) indicate the heights of the nanowire photodetectors

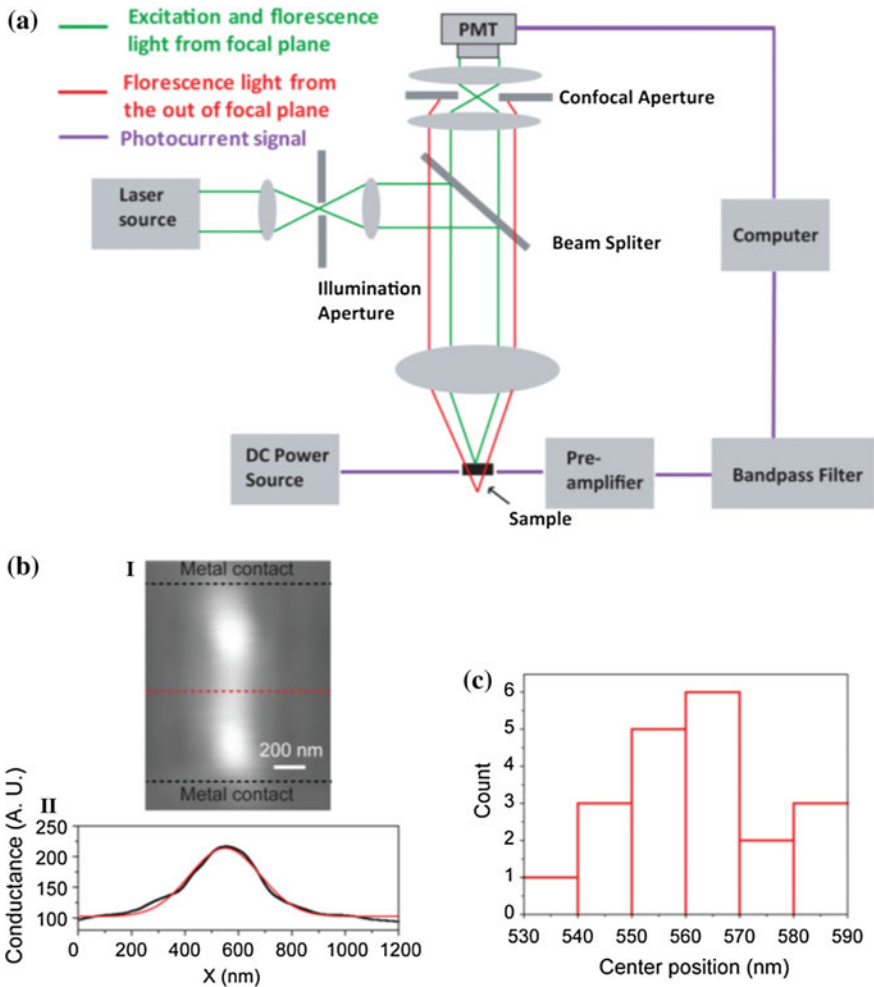


Fig. 3.3 Localization of 3D macroporous nanoelectronic devices. **a** Schematic of photocurrent detection from FET devices [25] and correlation with confocal microscopy laser spot scanning position. A 405 nm laser wavelength, 100X water immersion lens, and 0.1 mV source/drain device bias-voltage were used in the experiments. **b**, High-resolution (1 nm per pixel) photocurrent image (I) from a single nanowire device (2 μm channel length between upper/lower metal contacts) recorded scanning in x-y plane. The red dash line indicates the direction perpendicular to the nanowire axis. The black dash lines indicate the boundaries of metal contacts. (II) Photocurrent measured along the red dash line in (I). Experimental data are fit with a Gaussian distribution (red solid curve). **c** Distribution of the center point positions determined from the 20 independent scans in region of indicated in Fig. 3.2b and about the single scan line shown in (b, I)

networks. Reconstructed 3D images (Fig. 3.3c) show that the 12 active nanowire devices can be readily mapped with respect to x-y-z coordinated in the ‘scrolled-up’ macroporous structure. Given the complexity possible in 3D nanoelectric/host hybrid materials, this approach provides straightforward methodology for

determining at high-resolution the positions of the active nanoelectronic sensory elements with respect to detail structures within the host. In the future, we also note that the resolution could be even further improved by incorporating point-like transistor photoconductivity detectors [10, 17], *p-n* photodiodes [18] and *p-i-n* avalanche photodiodes [19] nanowire building blocks within the 3D macroporous nanoelectronic network.

3.3.2 Mapping Chemical Diffusion in Gel

We have used 3D macroporous nanoelectronic networks hybridized with agarose gel to map pH changes in 3D through the gel. The p-type nanowire FET device was used as chemical sensor. The hybrid nanoelectronic/gel material was prepared as description in experimental section. A reconstructed 3D fluorescence image of the hybrid material (Fig. 3.4a) shows clearly the 3D macroporous chemical sensors network fully embedded within an agarose gel block without phase separation. To carry out sensing experiments the 3D nanoelectronic/gel hybrid material was contained within a microfluidic chamber (Fig. 3.4b). Positions of nanowire transistor devices, which can function as very sensitive chemical/biological sensors [10, 11, 20], were determined by the photocurrent mapping method described above. As a comparison, 3D macroporous nanoelectronic chemical sensors network without gel was placed the chamber filled by aqueous solution. For both samples, we recorded signals simultaneously from 4 sensors chosen to span positions from upper to lower boundary of network or gel, where representative *z*-coordinates of the devices positions within the hybrid sample are highlighted in Fig. 3.4c; a similar *z*-range of devices for the free nanoelectronic network was also used.

Representative data recorded from chemical sensors in 3D macroporous nanoelectronic network without gel (Fig. 3.4d, I) and in the hybrid 3D nanoelectronic/agarose gel hybrid (Fig. 3.4d, II) highlight several important points. First, the device within the 3D macroporous nanoelectronic network without gel showed fast stepwise conductance changes (<1 s) with solution pH changes. The typical sensitivity of these devices was ca. 40 mV/pH, and is consistent with values reported for similar nanowire devices [21]. Second, the device within the 3D nanoelectronic/gel hybrid exhibited substantially slower transition times with corresponding changes of the solution pH; that is, signal change required on order of 2000 s to reach steady-state, and thus was 1000-fold slower than in free solution. Third, the time to achieve one-half pH unit change for the four different devices in 3D macroporous network without gel (Fig. 3.4e, I) is ca. 0.5 s and the difference between devices is only ca. 0.01 s. We note that the time delay in the data recorded from device d4 is consistent with the down-stream position of this device within the fluidic channel. In contrast, the time to achieve one-half for the four devices in the 3D nanoelectronic/gel hybrid (Fig. 3.4e, II) range from ca. 280 to 890 s for devices d1 to d4, respectively. The results show that the device response time within the agarose is ca. 500–1700 times slower than in solution and is proportional to the

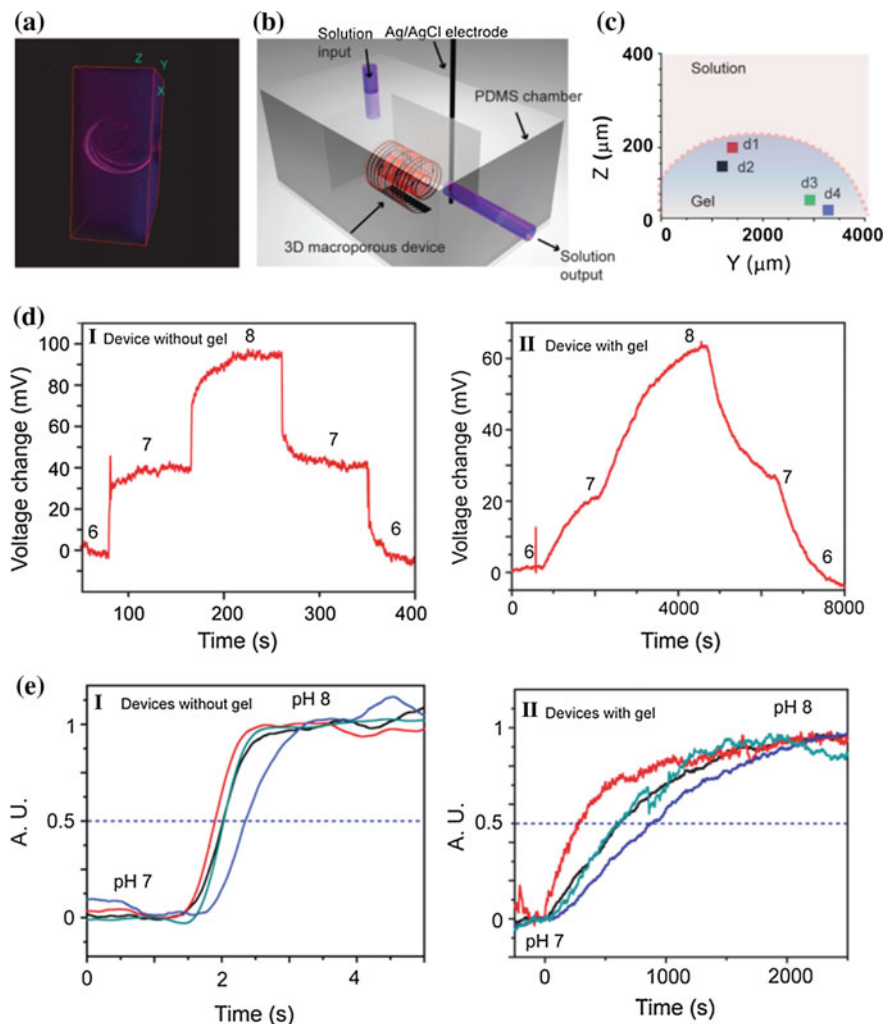


Fig. 3.4 3D macroporous chemical sensors. **a** x-z views of 3D reconstructed image of the 3D macroporous nanoelectronic network in gel. Red (rhodamine 6G): SU-8 mesh network and blue (DAPI): agarose gel. Dimensions: $x = 317 \mu\text{m}$; $y = 317 \mu\text{m}$; and $z = 144 \mu\text{m}$. **b** Schematics of the experimental set-up. **c** The projection of four nanowire devices in the y-z plane. Red dashed line corresponds to the approximate gel boundary, and the red and blue areas correspond to aqueous solution and agarose gel, respectively. **d** Representative change in calibrated voltage over time with pH change for 3D macroporous nanowire chemical sensors in solution (I) and embedded in agarose gel (II). **e** Calibrated voltage with one pH value change in solution for 4 different devices located in 3D space. (I) 4 devices without gel and (II) 4 devices embedded in agarose gel

distance from the solution/gel boundary, although the detailed variation suggests heterogeneity in the diffusion within the agarose gel. Significantly, the ability to map the diffusion of molecular and biomolecular species in 3D hybrid systems

using the macroporous nanoelectronic chemical sensor networks offers opportunities for self-monitoring of gel, polymers and tissue systems relevant to many areas of science and technology [22, 23].

3.3.3 Mapping Strain Distribution in Elastomer

We have used embedded 3D macroporous nanoelectronic networks to map strain distributions in elastomeric silicone host materials. Previous studies have shown that Si nanowires have a high piezoresistance response [12], making them as good

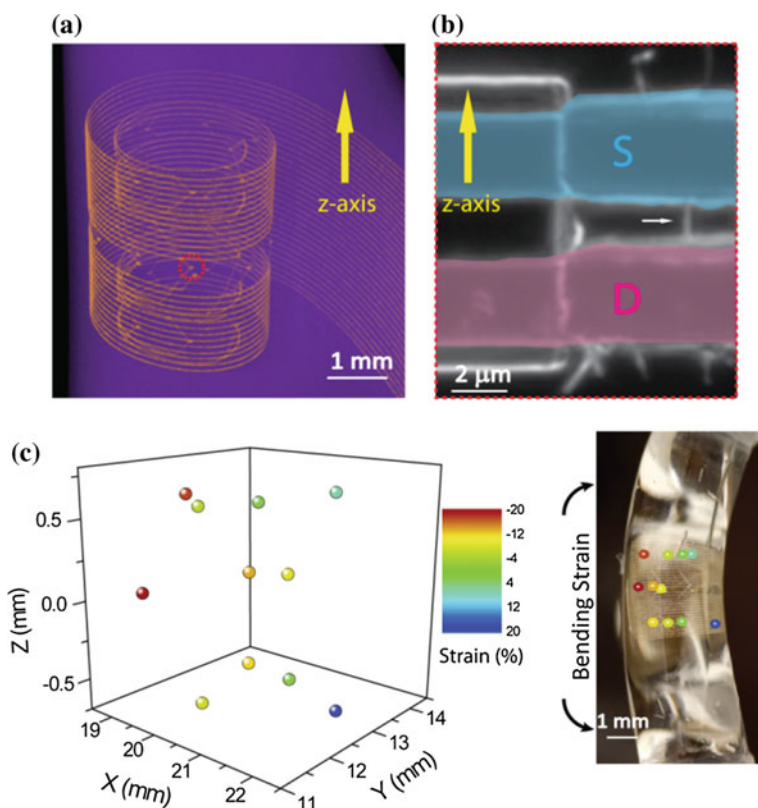


Fig. 3.5 3D macroporous strain sensors embedded in elastomer. **a** μ -CT 3D reconstruction of the macroporous strain sensor array embedded in a piece of elastomer. Pseudo-colors are applied: orange: metal, purple: elastomer. **b** Dark field microscopy image of a typical nanowire device indicated by red dash circle in (a). All the functional nanowires are intentionally aligned parallel to the axial axis of the elastomer cylinder. The white arrow points a nanowire. **c** A bending strain field was applied to the elastomer piece. The 3D strain field was mapped by the nanowire strain sensors using the sensitivity calibration of the nanowire devices. The detected strains are labeled in the cylinder image at the device positions

candidates for strain sensors [13]. To explore the potential of Si nanowire device arrays to map strain within materials, we have prepared and characterized 3D macroporous nanoelectronic/elastomer hybrid materials. The resulting hybrid macroporous nanoelectronic/elastomer cylinders had volumes of ca. 300 μm^3 [3] with volume ratio of device/elastomer of $<0.1\%$. X-ray micro-computed tomography (μCT) studies of the nanoelectronic/elastomer cylinders (Fig. 3.5a) were used

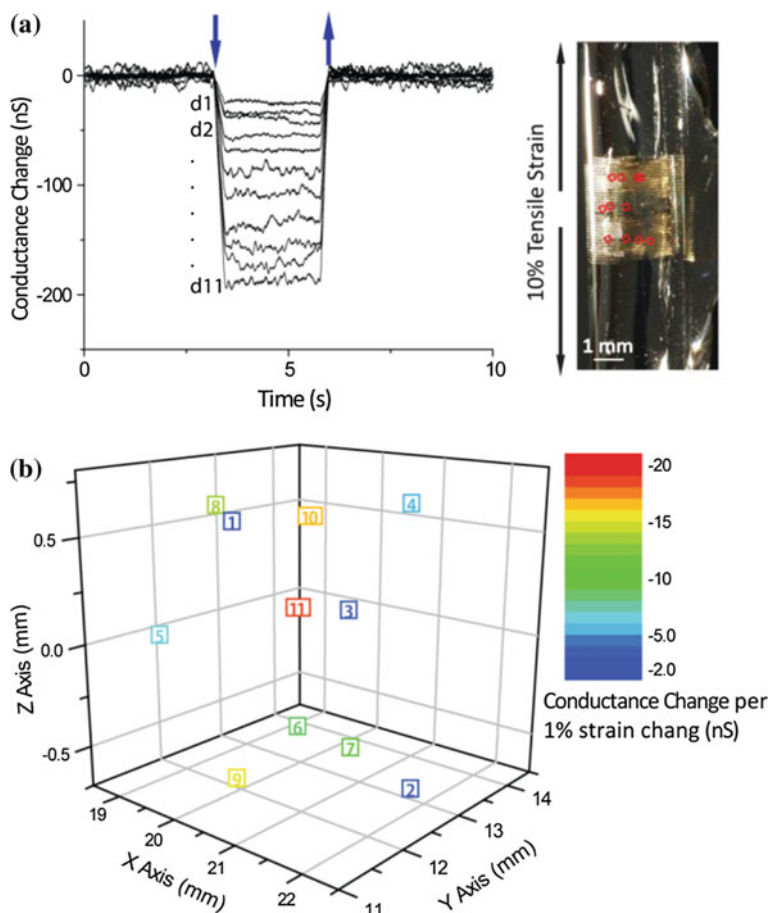


Fig. 3.6 Calibration of the 3D macroporous nanoelectronic strain sensors. **a** Conductance change versus time as a 10% tensile strain was applied to hybrid 3D macroporous nanoelectronic networks/PDMS cylindrical sample. The downward and upward pointing arrows denote the times when the strain was applied and released, respectively. The direction of strain on the cylindrical hybrid sample and projected position of the macroporous nanoelectronic networks are indicated in the right optical micrograph. The conductance changes of 11 measured nanowire devices (labeled arbitrarily in terms of increasing sensitivity) were recorded and used for the conductance change per strain calibration. **b** Strain sensitivity calibration of the nanowire devices is plotted in 3D. The data points are color coded by the sensitivity of the devices (**a**)

to determine the 3D metal interconnects and locations of nanowire devices within the cylindrical hybrid structures. The alignment of nanowire elements along the cylinder axis was confirmed by dark-field optical microscopy images (Fig. 3.5b), which show the nanowires lying along the cylinder (z) axis.

The good axial alignment of the nanowire devices was exploited to calibrate the strain sensitivity of each of elements with the 3D hybrid structure allows straightforward calibration of the device sensitivity in pure tensile strain field. Application of a 10% tensile strain along the cylinder axis (Fig. 3.6a) yielded decreases in conductance up to 200 nS for the individual devices, d1–d11. Because the conductance immediately returned to baseline when strain was released and under compressive loads the conductance change had the opposite sign, we can conclude that these changes do reflect strain transferred to the nanowire sensors. From the specific response of the devices within the hybrid structure we calculate and assign a calibrated conductance change/1% strain value for each of the eleven sensor elements (Fig. 3.6b), and use this for analysis of different applied strains. For example, we applied a bending strain to the cylinder and from the recorded conductance changes and calibration values were able to map readily the 3D strain field as shown in Fig. 3.5c. We note that the one-dimensional geometry of nanowires gives these strain sensors nearly perfect directional selectivity, and thus, by developing macroporous nanoelectronic network with nanowires device aligned parallel and perpendicular to the cylinder axis enable mapping all three components of the strain field in the future.

3.4 Conclusion

The macroporous nanoelectronic networks were merged with organic gels and polymers to form hybrid materials in which the basic physical and chemical properties of the host materials were not substantially altered with >90% active devices yield in nanoelectronic networks. We further demonstrated a simultaneous nanowire device photocurrent/confocal microscopy imaging measurement to determine the positions of the nanowire devices within 3D hybrid materials with ca. 14 nm resolution. This method also could be used for localizing device positions in macroporous nanoelectronic/biological samples, where it could provide the capability of determining positions of nanoscale sensors at the subcellular level. In addition, we explored functional properties of these hybrid materials. First, we showed that it was possible to map time-dependent pH changes throughout a nanowire network/agarose gel sample during external solution pH changes. These results suggest substantial promise of the 3D macroporous nanoelectronic networks for real-time mapping of diffusion of chemical and biological species through polymeric samples as well as biological materials such as synthetic tissue [23, 24]. Second we demonstrated that Si nanowire elements can function as well-defined strain sensors, and thereby characterize the strain field in a hybrid nanoelectronic elastomer structures subject to uniaxial and bending forces. More generally, we

believe our approach to fabrication of multi-functional 3D electronics and integration with host materials suggests substantial promise for (1) general fabrication of truly 3D integrated circuits based on conventional fabrication processes via assembly from a 2D “precursor”, (2) seamless 3D incorporation of multi-functional nanoelectronics into host systems leading to make “very smart” material systems.

Bibliography

1. Reuss RH, Hopper DG, Park JG (2006) Macroelectronics. *MRS Bull* 31:447
2. Thakor, NV (2013) Translating the brain-machine interface. *Sci Transl Med* 5, 210ps17
3. Kim DH et al Epidermal electronics. (2011) *Science* 33:838
4. Lu N, Kim DH (2013) Flexible and stretchable electronics paving the way for soft robotics. *Soft Robot* 1:53
5. Kim DH et al (2010) Dissolvable films of silk fibroin for ultrathin, conformal bio-integrated electronics. *Nat Mater* 9:511
6. Wise G, Eng KDIEEE (2005) Silicon microsystems for neuroscience and neural prostheses. *Med Biol Mag* 24:22
7. Normann RA (2007) Technology insight: future neuroprosthetic therapies for disorders of the nervous system. *Nat Clin Pract Neuro* 3:444
8. Seymour JP, Kipke DR (2007) Neural probe design for reduced tissue encapsulation in CNS. *Biomaterials* 28:3594
9. Fan Z, Ho JC, Jacobson ZA, Razavi H, Javey A (2008) Large-scale, heterogeneous integration of nanowire arrays for image sensor circuitry. *Proc Natl Acad Sci U S A* 105:11066
10. Cui Y, Wei Q, Park H, Lieber CM (2001) Nanowire nanosensors for highly sensitive and selective detection of biological and chemical species. *Science* 293:1289
11. Zheng GF, Patolsky F, Cui Y, Wang WU, Lieber CM (2005) Multiplexed electrical detection of cancer markers with nanowire sensor arrays. *Nat Biotechnol* 23:1294
12. He R, Yang P (2006) Giant piezoresistance effect in silicon nanowires. *Nat Nanotechnol* 1:42
13. Lee CH, Kim DR, Zheng X (2009) Fabricating nanowire devices on diverse substrates by simple transfer-printing methods. *Proc Natl Acad Sci U S A* 107:9950
14. Tsen AW, Donev LAK, Kurt H, Herman LH, Park J (2009) Imaging the electrical conductance of individual carbon nanotubes with photothermal current microscopy. *Nat Nanotechnol* 4:108
15. Huang B, Wang WQ, Bates M, Zhuang XW (2008) Three-dimensional super-resolution imaging by stochastic optical reconstruction microscopy. *Science* 319:810
16. Toprak E, Balci H, Blehm BH, Selvin PR (2007) Three-dimensional particle tracking via bifocal imaging. *Nano Lett* 7:2043
17. Cohen-Karni T et al (2012) Synthetically encoded ultrashort-channel nanowire transistors for fast, pointlike cellular signal detection. *Nano Lett* 12:2639
18. Jiang Z, Qing Q, Xie P, Gao R, Lieber CM (2012) Kinked p–n junction nanowire probes for high spatial resolution sensing and intracellular recording. *Nano Lett* 12:1711
19. Hayden O, Agarwal R, Lieber CM (2006) Nanoscale avalanche photodiodes for highly sensitive and spatially resolved photon detection. *Nat Mater* 5:352
20. Patolsky F, Timko BP, Zheng G, Lieber CM Nanowire-based nanoelectronic devices in the life sciences. (2007) *MRS Bulletin* 32:142
21. Tian B et al (2010) Three-dimensional, flexible nanoscale field-effect transistors as localized bioprobes. *Science* 329:831
22. Griffith LG, Swartz MA (2006) Capturing complex 3D tissue physiology in vitro. *Nat Rev Mol Cell Biol* 7:211

23. Sanger F, Nicklen S, Coulson AR (1977) DNA sequencing with chain-terminating inhibitors. *Proc Natl Acad Sci U S A* 74:5463
24. Glicklis R, Merchuk JC, Cohen S (2004) Modeling mass transfer in hepatocyte spheroids via cell viability, spheroid size, and hepatocellular functions. *Biotechnol Bioeng* 86:672
25. Ahn Y, Dunning J, Park J (2005) Scanning photocurrent imaging and electronic band studies in silicon nanowire field effect transistors. *Nano Lett* 5:1367

Chapter 4

Three-Dimensional Macroporous Nanoelectronics Scaffold Innervated Synthetic Tissue

4.1 Introduction

Functional synthetic 3D macroporous biomaterials as extracellular matrices (ECMs) are crucial for areas ranging from biophysics to regenerative medicine because they allow for studies of cell/tissue development in the presence of spatiotemporal biochemical stimulants [1–6], and the understanding of pharmacological response of cells within synthetic tissues models is expected to provide a more robust link to in vivo disease treatment than that from 2D cell cultures [6–8]. Advancing further such biomaterials requires capabilities for monitoring cells at single cell resolution throughout the whole 3D microenvironment [6]. While electrical sensors are attractive tools, it has not been possible to integrate such elements within biomaterials for real-time monitoring of cellular activities and physicochemical change without interrupting interconnections among those cells. Such integration, if possible, could lead to new lab-on-a-chip pharmacological platforms [9, 10] and hybrid 3D electronics-tissue materials for synthetic biology and prosthetics [11, 12].

The emergence of flexible electronics has significantly advanced the electronics-biology interface through the coupling of electronics and tissues using flexible planar devices [13–17]. These planar devices have been used to probe electrical activities near surfaces of various tissues through conform to nature tissue surfaces [13–17]. However, a seamless 3D integration of such flexible electronics within 3D biomaterials and synthetic tissues has not been achieved. To be succeed, it is important to implement a biomimetic design into electronics, which should include following points: (1) the electronic structures must be macroporous, not planar, to enable 3D interpenetration with biomaterials and cellular network; (2) the electronic network should have nanometer to micrometer scale features comparable to biomaterial scaffolds and cellular components; and (3) the electronic network must have a 3D interconnectivity and (4) the electronic network must have chemical and physical properties similar to biomaterials.

Here we introduce a conceptually new approach that meets this challenge by integrating nanoelectronics throughout biomaterials and synthetic tissues in 3D using macroporous nanoelectronic networks that we introduced in Chap. 2 as nanoelectronic scaffolds (nanoES). We use silicon nanowire field effect transistor (FET) as the functional element, given their capability for recording both extracellular and intracellular signals with subcellular resolution [18–21]. FET detectors respond to variations in potential at the surface of the transistor channel region. The sensitivity of FET is independent from the surface impedance, which allows FET sensors to be scaled down to nanoscale size while maintaining their sensitivity. This unique property is considered as active device [21]. Metal-electrode [22, 23] or carbon nanotube/nanofiber [24, 25] based passive detectors are not considered in our work because impedance limitations (i.e., signal/noise and temporal resolution degrade as the area of the metal or carbon electrodes is decreased) make it difficult to reduce the size of individual electrodes to the subcellular level [21–23], a size regime necessary to achieve noninvasive 3D interface of electronics with cells in tissue.

Figure 4.1 shows stepwise incorporation of biomimetic and biological elements into nanoelectronic networks across nanometer to centimeter size scales. First,

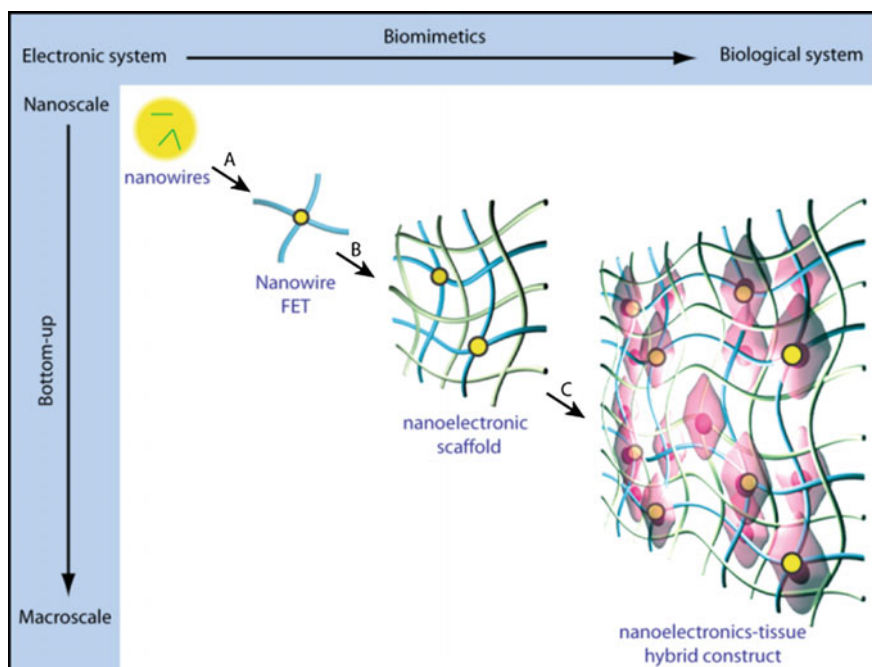


Fig. 4.1 Integrating nanoelectronics with cells and tissue. New concept for an integrated system from the discrete electronic and biological building blocks. A biomimetic and bottom-up process have been designed: **a** building nanoelectronic network. **b** Forming a 3D macroporous nanoelectronic scaffold (nanoES) by self- or manual organization and hybridization with traditional extracellular matrices, and **c** incorporation of cells and growth of synthetic tissue via biological processes. Yellow dots: nanowire nanoelectronic components, blue ribbons: metal and epoxy interconnects, green ribbons: traditional extracellular matrices, pink: cells

nanowires were deposited for single nanowire FETs (Step A, Fig. 4.1). Second, individual nanowire FET devices were lithographically patterned and integrated into free-standing macroporous scaffolds (Step B, Fig. 4.1), the nanoES. The nanoES were designed to mimic ECM structures, and specifically, to be 3D, to have nanometer to micrometer features with high (>99%) porosity, and to be highly flexible and biocompatible. NanoES were then combined with synthetic or natural macroporous ECMs. Finally, cells were cultured within the nanoES (Step C, Fig. 4.1) to yield 3D nanoelectronics innervated synthetic tissue, in which nanoelectronic devices innervates cells at the subcellular level throughout whole 3D tissue. The nanoES are distinct from conventional 2D multi-electrode arrays (MEA) [23], carbon nanotube/nanofiber arrays [24, 25], implantable microelectrodes [23] and flexible or stretchable electrodes [13–17] in that the sensors are nanoscale semiconductors, and critically, that the sensor network is flexible, macroporous and 3D.

4.2 Experimental

4.2.1 *NanoES/Tissue Scaffold*

NanoES: Kinked and uniform silicon nanowires were synthesized by the methods described previously. The fabrication for nanoES with uniform nanowire as nanoFET device was described in Chaps. 2 and 3. The fabrication for nanoES with kinked and modulated doped nanowire as nanoFET device employs electron beam lithography (EBL) to pattern SU-8 supporting and passivation layer, and metal contact and interconnects. All the other processes are the same as that for fabrication of uniform nanowire nanoES.

NanoES/collagen (Matrigel™) hybrid matrix: Prior to gel casting, collagen type-I (Sigma-Aldrich Corp., St. Louis, MO) was diluted (1:2–1:5) with culture media or phosphate buffered saline solution (PBS) and the pH was adjusted to ~7.4. Matrigel™ was used as received or diluted (1:2–1:5). The Matrigel™ solutions were allowed to form gels around nanoES.

NanoES/alginate hybrid scaffold: The 3D nanoES/alginate scaffolds were prepared from pharmaceutical-grade alginate, Protanal LF5/60, which has a high guluronic acid (G) content (65%). Sodium alginate solutions were drop casted on nanoES, frozen and treated by lyophilization to produce sponge like scaffolds.

NanoES/PLGA hybrid scaffold: Poly(lactic-co-glycolic acid) (PLGA) electrospun fibers were used as a secondary scaffold in general experiments. The PLGA fibers were prepared based on reported procedures [26]. To prepare hybrid scaffolds, a sheet of PLGA fibers with diameters of ~1–3 μm was deposited on both sides of the mesh nanoES.

4.2.2 Scaffold Mechanical Properties

The effective bending stiffness per unit width of the mesh scaffold, \bar{D} , can be estimated by [17]

$$\bar{D} = \alpha_s D_s + \alpha_m D_m \quad (4.1)$$

where α_s and α_m are the area fraction of the single-layer polymer (SU-8) ribbon (without metal layer and top polymer passivation layer) and three-layer ribbon (bottom polymer layer, metal layer and top passivation layer) in the whole mesh structure. $D_s = E_s h^3/12$ is the bending stiffness per unit width of the single-layer polymer, where $E_s = 2$ GPa and h are the modulus and thickness of the SU-8. D_m is the bending stiffness per unit width of a three-layer structure, which can be calculated by [27]

$$D_m = \frac{E_m b_m h_m^3}{12b} + \frac{E_s}{b} \left(\frac{(b - b_m)(2h + h_m)^3}{12} + \frac{1}{6} b_m h^3 + 2b_m h \left(\frac{h}{2} + \frac{h_m}{2} \right)^2 \right) \quad (4.2)$$

where $E_m = 121$ GPa and h_m are the modulus and thickness of the palladium, b is the width of the single-layer ribbon and the total width of the three-layer ribbon, b_m is the width of the palladium layer. In addition, the chromium layers are so thin (1.5 nm) that their contribution to the bending stiffness is negligible. When $h_m = 75$ nm, $h = 0.5$ μm , $b = 10$ μm , $b_m = 5$ μm , $\alpha_s = 2.51\%$ and $\alpha_m = 3.57\%$, we can calculate $\bar{D} = 0.006$ nN m. When $h_m = 75$ nm, $h = 2$ μm , $b = 40$ μm , $b_m = 20$ μm , $\alpha_s = 10.06\%$ and $\alpha_m = 13.31\%$, we can calculate $\bar{D} = 1.312$ nN m.

To calculate the strain in tubular constructs, we used the equation $\varepsilon = y/R$, where y is the distance from the neutral plane, and R is the radius of curvature [27]. For the symmetric mesh scaffold, since the neutral plane is the middle plane, the maximum strains of metal and SU-8 appear at $y = h_m/2$ and $y = h_m/2 + h$, respectively. When $h_m = 75$ nm, $h = 2$ μm , $R = 0.75$ μm^{-1} , the maximum strains of metal and SU-8 are 0.005 and 0.272%, respectively.

The self-organized structure of nanoES was simulated by the commercial finite element software ABAQUS following the same parameters and procedure as described in Chap. 2.

4.2.3 Cell Culture

Neuron culture: Device chips were cleaned by oxygen plasma, and fixed onto a temperature controlled chamber with double-sided tape (Fig. 4.2a). A 1 mm thick polydimethylsiloxane (PDMS) membrane was placed over the device area, followed by wire-bonding of individual devices (Fig. 4.2b). An autoclaved glass ring was placed and fixed over this PDMS chamber (Fig. 4.2c). The whole chip was sterilized

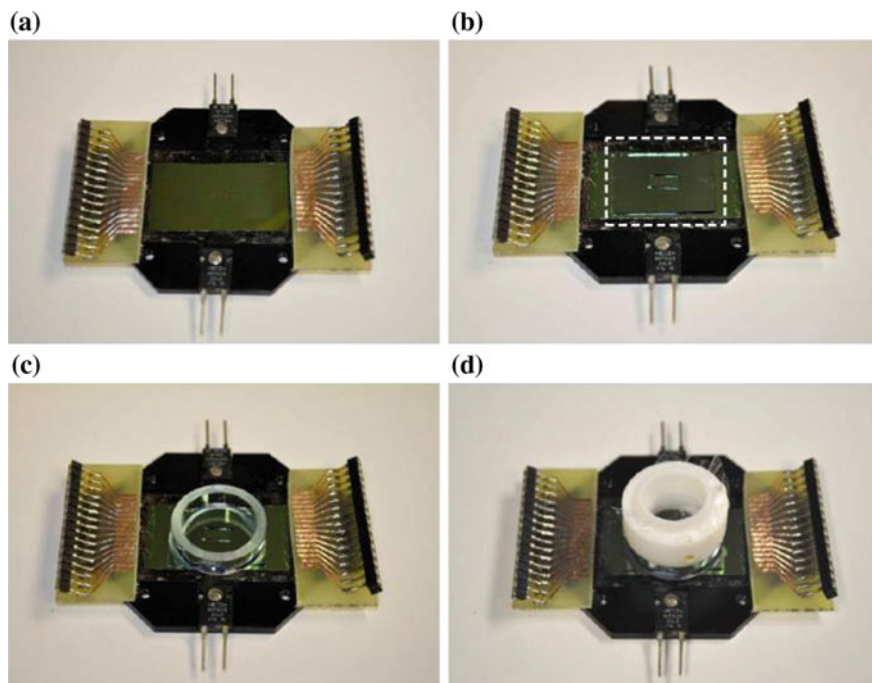


Fig. 4.2 Chip assembly for neuronal 3D cultures. **a** A scrolled-up nanoES chip was sterilized and assembled onto a temperature controlled chip carrier. **b** A shallow PDMS chamber (dashed box) was cleaned and placed over the assembled chip. **c** A glass ring was fixed over the PDMS chamber. **d** A gas-permeable, water-impermeable membrane cover was used for neuron cultures

and filled by polylysine solution for surface modification overnight at 37 °C. Finally, the chamber was filled with culture medium for cell culture. Hippocampal neurons were prepared using a standard protocol [28]. After 1 day, medium was changed to Neurobasal™ medium supplemented with B27 Serum-Free Supplement, Glutamax™ and 0.1% Gentamicin reagent solution [29]. A gas-permeable/water-impermeable membrane covers were used to avoid evaporation while allowing for diffusion of gases (Fig. 4.2d).

Cardiomyocyte culture: Hybrid scaffolds (Fig. 4.3b) consisting of nanoES (Fig. 4.3a, g) sandwiched between two electrospun PLGA fiber layers were used in all experiments. The device chip was wire-bonded (Fig. 4.3c, h), and assembled with a petri-dish (Fig. 4.3d). The device chamber was cleaned by O₂ plasma and sterilized by UV-light and ethanol solution. The hybrid scaffolds were coated with fibronectin/gelatin solution overnight prior to cell seeding. Cardiac cells were isolated from intact ventricles of 1 to 3-day-old neonatal Sprague/Dawley rats as described elsewhere [30]. The cardiac cells were finally seeded with 5–10 mg/mL Matrigel™ onto fibronectin/gelatin coated PLGA/nanoES at an initial cell density of $3\text{--}6 \times 10^7 \text{ cm}^{-2}$ (Fig. 4.3e). After 1–2 days, the cell-seeded nanoES was manually folded into a construct, and was maintained in incubator for an additional 3–8 days

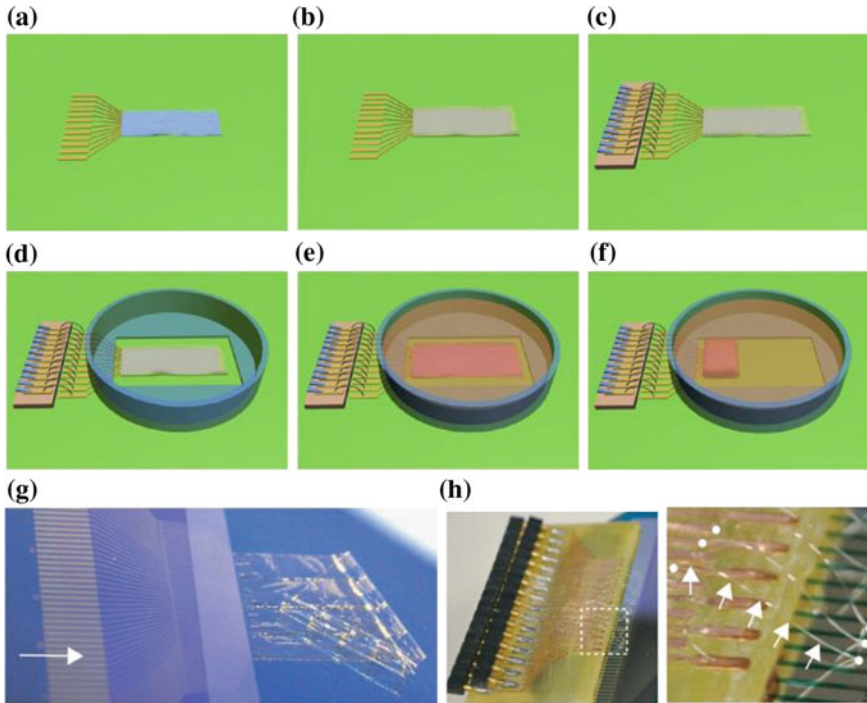


Fig. 4.3 Schematic of cardiomyocyte 3D culture. **a** A free-standing mesh-like nanoES. **b** Hybrid of PLGA electrospun fibers and mesh-like nanoES. **c** Individual devices were wire-bonded to PCB connectors. **d** A culture chamber was fixed over the scaffold. **e** The hybrid scaffold was seeded with cardiomyocytes/Matrigel. **f** The cardiac sheet (**e**) was folded and cultivated for an additional 3–10 days. **g** A mesh device showing the free-standing part (the right half) and the fixed part on the wafer (the left half). The arrow marks the outer-electrode pins for wire-bonding. **h** Printed circuit board (PCB) with wire-bonding. The wires connected the PCB copper pads (left) and the rectangular electrodes on the supported end of the mesh-like nanoES (right). White dots highlight bonding points. Arrows highlight one wire-bonded aluminum wire

(Fig. 4.3f). All animal procedures conformed to US National Institutes of Health guidelines and were approved by Harvard University’s Animal Care and Use Committee.

Vascular construct: Synthetic vascular constructs were produced in a manner similar to the sheet-based tissue engineering approach described previously [31] (Fig. 4.4). First, the mesh nanoES were coated with gelatin/fibronectin solution overnight (Fig. 4.4a–c). Second, human aortic smooth muscle cells were seeded at a density of $1 \times 10^4 \text{ cm}^{-2}$ on the gelatin/fibronectin-coated devices and cultured in Medium 231 supplemented with smooth muscle growth supplement (Fig. 4.4d). Sodium L-ascorbate was added to the culture medium to stimulate extracellular matrix (ECM) synthesis as previous report [31]. Human aortic smooth muscle cells (HASMCs) were maintained in incubator until their secreted ECM proteins formed a cohesive tissue sheet [31] that can be easily peeled off from the silicon substrate.

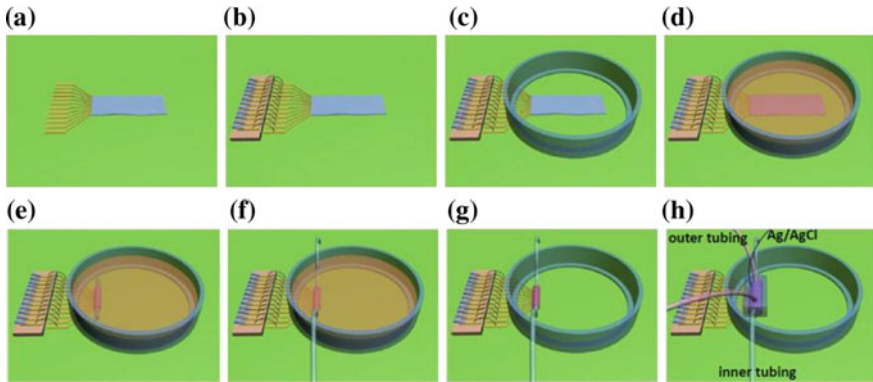


Fig. 4.4 Schematic of vascular nanoES construct preparation and pH sensing. **a** A free-standing mesh-like nanoES. **b** Individual devices were wire-bonded to PCB connectors. **c** A modified petri-dish was fixed over the scaffold with silicone elastomer. **d** The hybrid scaffold was sterilized with UV-light illumination for 1 h and soaking in 70% ethanol solution for 0.5 h, coated with fibronectin/gelatin solution overnight and seeded with HASMCs. **e** After 7–14 days in culture, the HASMC-seeded nanoES (**d**) was rolled against a tubular support and cultivated for further days. **f** The tubular support was removed and tubing was connected to the ends of the lumen of the HASMC construct. **g** The medium was removed while keeping the construct moist. **h** A PDMS chamber was assembled around the construct, attached to tubing to bathe the outside of the construct and Ag/AgCl electrodes to measure pH in the bathing fluid

The cell-coated mesh nanoES was then gently lifted from the SiO₂ substrate using fine forceps, rolled onto a polystyrene or glass tubular support 1.5 mm in diameter, then maintained in incubator for another 2 weeks for maturation of the vascular structure (Fig. 4.4e). For pH sensing experiment, the temporary tubular support was removed, and segments of polystyrene tubing were connected to the open ends of the vascular construct (Fig. 4.4f), and a PDMS fluidic chamber with input/output tubing and Ag/AgCl as shown in Fig. 4.4h.

4.2.4 Staining

Immunostaining: First, cells were fixed with 4% paraformaldehyde, pre-blocked by 1% bovine serum albumin (BSA) in PBS and permeabilized by 0.2–0.25% Triton X-100 and 1% bovine serum albumin (BSA) in PBS. Second, cells were incubated with primary antibodies in 1% BSA in 1X PBS with 0.1% (v/v) Tween 20 (PBST) overnight at 4 °C. Finally, cells were incubated with the secondary antibodies with fluorophores. Hoechst 34580 was used for staining nuclei. Neuronal class III β -Tubulin (TUJ1) mouse monoclonal antibody, anti- α -actinin mouse monoclonal antibody, anti-smooth muscle α -actin rabbit polyclonal antibody and corresponding secondary antibody were used for staining neuron, cardiomyocytes and HASMC.

Labelling nanoES/tissue scaffold: SU-8 resist for nanoES fabrication was doped with rhodamine 6G before deposition and patterning. PLGA electrospun

fiber scaffolds were labeled by physical absorption of rhodamine 6G from an aqueous solution.

Hematoxylin-eosin and Masson trichrome staining: The vascular constructs were cut and fixed in formalin solution and then infiltrated with molten paraffin. The infiltrated tissues were embedded into paraffin blocks and cut into 5–6 μm sections. Then the sections were rehydrated. Standard hematoxylin and eosin staining [33] was carried. Collagen secretion by HASMCs was assessed on deparaffinized sections using a Masson's trichrome staining kit according to a standard protocol [34].

4.2.5 Characterization

Confocal and epi-fluorescence imaging was carried out using an Olympus Fluoview FV1000 confocal laser scanning microscope. *ImageJ* was used for 3D reconstruction and analysis of the confocal and epi-fluorescence images. Bright-field optical micrographs of histological samples were acquired on an Olympus FSX100 system. HMXST Micro-CT X-ray imaging system was used for imaging metal interconnects in synthetic vascular construct. *VGStudio MAX* was used for 3D reconstruction and analysis of the micro-CT images. LIVE/DEAD[®] Viability/Cytotoxicity Kit was used to evaluate hippocampal neuron viability on days 7, 14 and 21 of the culture. CellTiter 96[®] AQueous One Solution Cell Proliferation Assay was used for evaluate the mitochondrial metabolic activity of cardiomyocyte on days 2, 4, 6, 8, 10 and 12 of the culture.

4.2.6 Electrical Measurement

The nanowire FET conductance and transconductance were measured and calibrated in $1 \times \text{PBS}$ as described previously [18]. For nanowire FET stability tests, nanoES were maintained under neuron culture conditions for predetermined intervals. Electrical transport measurements and recordings were obtained in culture medium (for neuron), tyrode solution (for cardiac construct) and PBS solution with different pH value (for vascular construct) by home-built amplifiers as described previously [18, 20].

4.3 Results and Discussion

4.3.1 NanoES Characterization

We have designed two nanoES (Fig. 4.5) that are free-standing, flexible and contain similar components. 3D self-organized nanoES (Fig. 4.5a) were made by electron

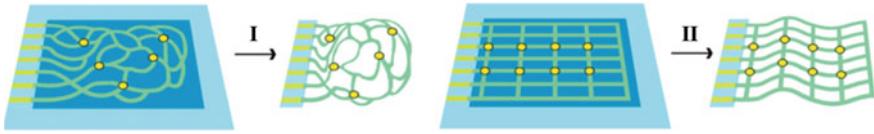


Fig. 4.5 Macroporous and flexible nanowire nanoES. Device fabrication schematics. **I:** 3D self-organized nanowire FET devices. **II:** mesh nanowire FET devices. Light blue: silicon oxide substrates, blue: nickel sacrificial layers, green: nanoES, yellow dots: individual nanowire FETs

beam lithography. Previously discussed mechanics-driven self-organization created a random or regular network of 3D features that mimic the size scale and morphology of submicron ECM features, such as the fibrous meshwork of brain ECM [36]. Open mesh nanoES (Fig. 4.5b) were made by photolithography with a regular structure, similar to the ECM of the ventricular myocardium [37, 38]. The planar design and initial fabrication of these 3D nanoES use existing capabilities developed for conventional planar nanoelectronics, and could enable integration of additional device components (for example, memories and logic gates) [39, 40] and substantial increases in device number and overall scaffold size.

Reconstructed 3D confocal fluorescence images of typical 3D self-organized scaffolds viewed along y - and x -axes (Fig. 4.6a, I and II respectively) showed that the framework was 3D with a highly curvilinear and interconnected structure. The porosity (calculated from the initial planar device design and the final 3D construct volume) was $>99.8\%$, comparable to that of hydrogel biomaterials [6–8]. Scanning electron microscopy (SEM) of the 3D self-organized nanoES (Fig. 4.6b) revealed sub-micrometer feature sizes of individual device. Kinked nanowires and metallic interconnects contained within the SU-8 backbone have 80 nm and $0.7\ \mu\text{m}$ feature sizes in diameter, which are comparable to those of synthetic and natural ECMs [3, 8], and are several orders of magnitude smaller than those for electronic structures [23] that is used to directly insert into tissue.

Figure 4.6c shows the 3D distribution of nanowire FET devices (Fig. 4.6a, II) within the scaffold. They are spanned separations of $7.3\text{--}324\ \mu\text{m}$ in 3D (Fig. 4.6c), and can be made closer together (for example, $<0.5\ \mu\text{m}$) by printing denser nanowires on the substrate [40] to improve spatial resolution of nanoelectronic sensors. We evaluated the performance of devices through water-gate measurements for the nanowire FET elements in the 3D scaffolds in phosphate buffered saline (PBS). The results show device yields ($\sim 80\%$), conductances ($1.52 \pm 0.61\ \mu\text{S}$; mean \pm SD) and sensitivities ($8.07 \pm 2.92\ \mu\text{S/V}$), comparable to measurements from planar devices using similar nanowires [18].

3D mesh nanoES were realized by manual folding and rolling of free-standing device arrays as discussed in previous chapters. Mesh structures (Fig. 4.5a, II) were fabricated such that the nanoES maintained an approximately planar configuration following relief from the substrate. A typical $3.5\ \text{cm} \times 1.5\ \text{cm} \times \sim 2\ \mu\text{m}$ mesh nanoES, was approximately planar with 60 nanowire FET devices in regular array with a 2D open porosity of 75% (Fig. 4.7a). This mesh porosity is comparable to that of honeycomb-like synthetic ECM engineered for cardiac tissue culture [38]. In

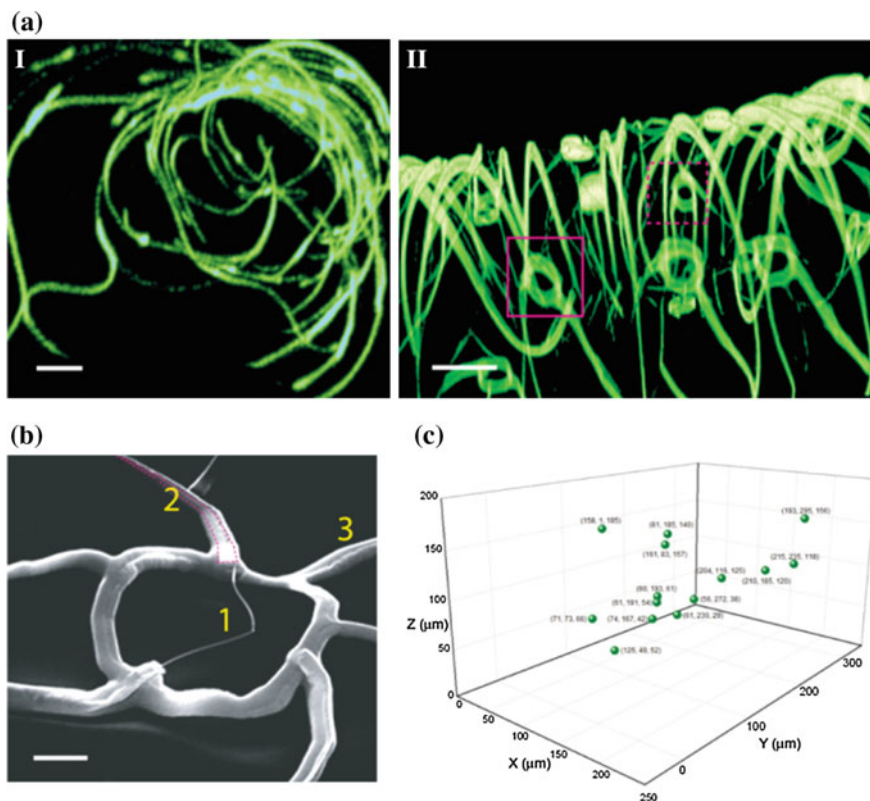


Fig. 4.6 3D self-organized nanowire nanoES. **a** 3D reconstructed confocal fluorescence images of self-organized nanoES viewed along y (**I**) and x (**II**) axes. x - y - $z = 300$ – 400 – 200 μm . Solid and dashed open magenta boxes indicate two nanowire FET devices located on different planes along x axis. Scale bars, 20 μm . **b** SEM image of a single kinked nanowire FET within a self-organized scaffold, showing (1) kinked nanowires, (2) metallic interconnects (magenta lines) and (3) the SU-8 backbone. Scale bar, 2 μm . **c** 14 nanowire FETs were distributed in the construct shown in (**a**)

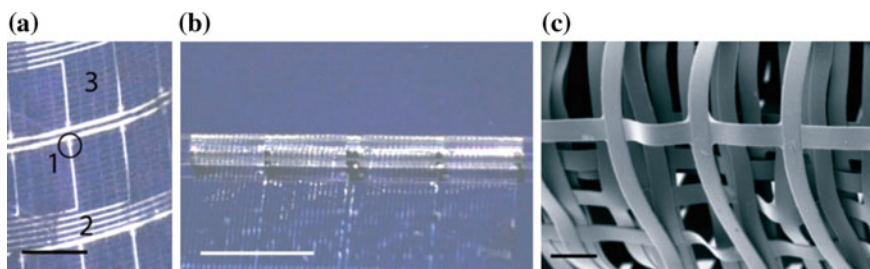


Fig. 4.7 Mesh nanowire nanoES. **a** Photograph of a mesh device, showing (1) nanowires, (2) metal interconnects, (3) SU-8 structural elements. The circle indicates the position of a single nanowire FET. Scale bar, 2 mm. **b** Photograph of a partially rolled-up mesh device. Scale bar, 5 mm. **c** SEM image of a loosely packed mesh nanoES, showing the macroporous structure. Scale bar, 100 μm

addition, the nanowires (Fig. 4.7a, 1), metal interconnects (Fig. 4.7a, 2), and SU-8 structural elements (Fig. 4.7a, 3) had an areal mass density of $<60 \mu\text{g}/\text{cm}^2$, the lowest value reported so far for flexible electronics, which reflects our macroporous architecture. The mesh nanoES was flexible and can be manually rolled into tubular constructs with inner diameters at least as small as 1.5 mm (Fig. 4.7b), and folded. Macroporous structures of the open mesh nanoES were formed either by loosely stacking adjacent mesh layers (Fig. 4.7c) or by shaping it with other biomaterials. These capabilities were consistent with the estimated ultralow effective bending stiffness, which was tuned between 0.006 and 1.3 nN m for this mesh and is comparable to recent planar epidermal electronics [17].

We evaluated the electrical transport characteristics of the mesh nanoES in PBS. Yield (90–97%), average conductance ($\sim 3 \mu\text{S}$) and sensitivity ($\sim 7 \mu\text{S}/\text{V}$) (Fig. 4.8a) of mesh electronics are comparable to planar nanowire FET device [18]. Representative conductance (G) data (Fig. 4.8b) from single nanowire FET (Fig. 4.8b, yellow dots, upper panel) during the rolling process showed a $<0.17 \mu\text{S}$ conductance change (ΔG) or $<2.3\%$ total change for 6 revolutions. Device sensitivity (S) remained stable with a maximum change (ΔS) of $0.031 \mu\text{S}/\text{V}$, or 1.5% variation. Furthermore, 14 devices evenly distributed on 6 layers of a rolled-up scaffold (Fig. 4.8c) showed maximum differences of $\Delta G = 6.8$ and $\Delta S = 6.9\%$ versus the unrolled state, demonstrating device robustness. Repetitive rolling and relaxation to the flat state did not degrade nanowire FET performance. These findings suggest potential for reliable sensing/recording of dynamic and deformable systems.

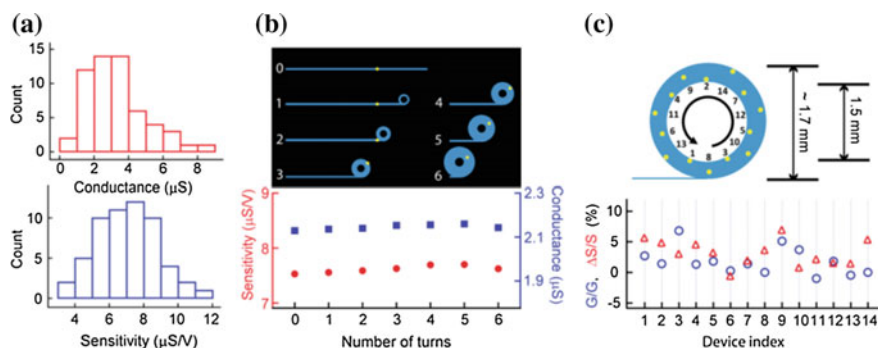


Fig. 4.8 Device performance characterization. **a** Histograms of nanowire FET conductance and sensitivity in one typical mesh nanoES. **b** Water-gate sensitivity and conductance of a nanowire FET device in a mesh device during the rolling process. Upper panel, schematic of nanowire FET position (yellow dot) during rolling process; 0–6 denote the number of turns. **c** Relative change in conductance and sensitivity of 14 nanowire FETs evenly distributed throughout a fully rolled-up mesh device. Upper panel, schematic of nanowire FET position (yellow dots). In **b** and **c** the thicknesses of the tubular structures have been exaggerated for schematic clarity

4.3.2 Mechanics-Driven 3D Self-organization

We have carried out simulations of a subunit of the self-organized structure (Fig. 4.9a–c). Measurements of bending for the corresponding experimental structures (Fig. 4.9c, open red squares) are consistent with the simulation (Fig. 4.9c). Additionally, changes in structural parameters (for example, total length of subunit and thicknesses of SU-8 or metals) yield predictable changes in the bending angle of the subunit (Fig. 4.10). Gradually increasing the bending angle along the bending ribbon of nanoES allows it to scroll-up into a 3D structure, with each layer separated with each other evenly. In this way, an ordered 3D nanowire FET arrays can be designed and fabricated with nanoFET evenly distributed in 3D space, which is particularly important for sensing experiment across the whole 3D space (Fig. 4.10).

Finally, we have these self-organized electronic domains in mesh-like structures (Fig. 4.11a), which could realize a hierarchical structure for nanoES design. Images of the self-organized domains (Fig. 4.11b, c) show that regular nanowire FET devices with distinct device positions can be realized by varying the structural parameters of individual elements. Overall, this approach yields hierarchical 3D nanoES with sub-micrometer to micrometer scale control in self-organized domains and millimeter to centimeter scale in the mesh matrix by folding or rolling as shown above (Fig. 4.7).

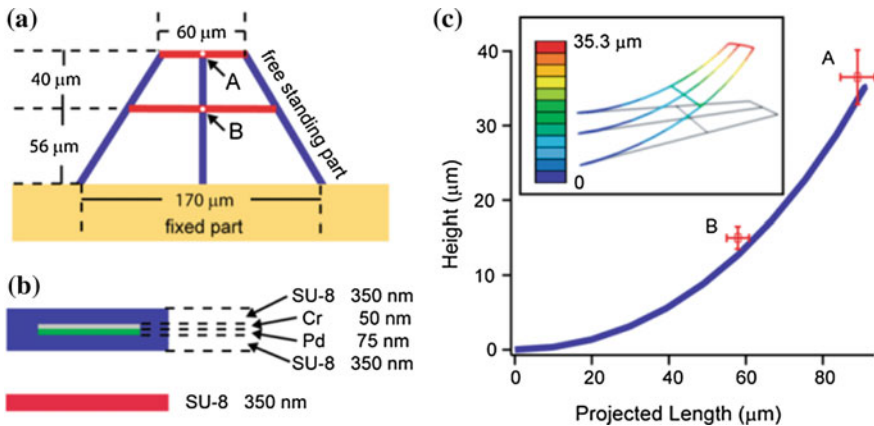


Fig. 4.9 Geometry control by design in nanoES. **a**, **b** represent the basic design and structural subunit for mechanical simulation. **a** Top-down view of the entire subunit. Blue ribbons are stressed metal lines with SU-8 passivation. Red lines are single SU-8 ribbons without residual stress. **b** Cross-sectional views of those two key structural elements used for simulation. **c** Plot of projected (on x - y plane) length versus height (in z direction) for the vertical blue ribbon in **(a)** as determined from the simulation. Open red squares with error bars are experimental data recorded in air for point A and B in **(a)**. Inset shows a 3D view of the simulated structure, and the scale bar shows different height in z direction

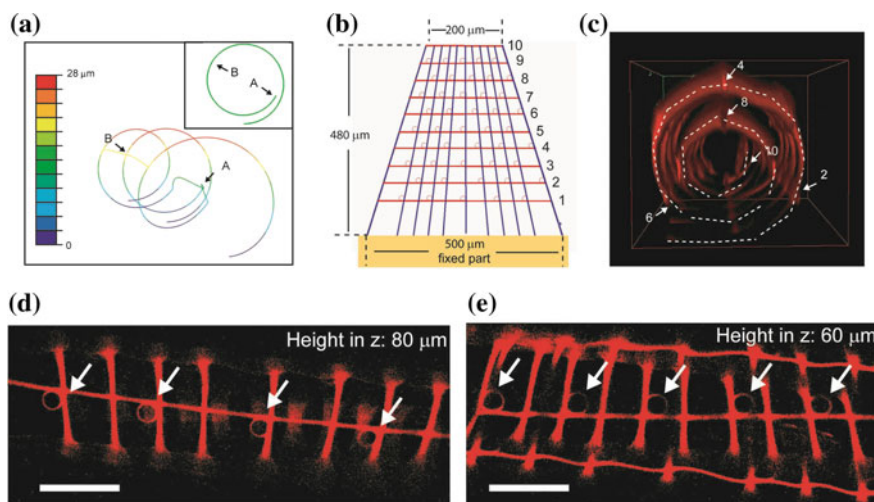


Fig. 4.10 Design and fabrication of self-organized nanoES. **a** Simulation shows that when the equivalent bending moment is increased by 10 times, the subunit structure scrolls up on itself. Inset shows the curve of the central blue ribbon in Fig. 4.9a, demonstrating that devices were scrolled up and different layers were separated. A and B are the two points in Fig. 4.9a. **b** The blue lines indicate stressed metal lines with SU-8 as passivation, red lines indicate non-stressed metal lines for interconnection with SU-8 as passivation or SU-8 ribbon as framework, and the circles mark positions for devices. **c** 3D reconstructed confocal fluorescence image of the corresponding fabricated self-organized construct following the design in (b). The dashed lines (c) highlight the edge of the ‘scrolled-up’ self-organized nanoES construct. The white numbers and arrows indicate the position of 5 horizontal lines corresponding to those numbered in (b). **d, e** Confocal fluorescence images scanned across the interior of the scaffold at different heights. The images demonstrate that the device regions (circles) are located in planes (heights of 80 and 60 μm are shown) are aligned, and thus demonstrate the regular arrangement in 3D. Scale bars in **d** and **e** are 50 μm

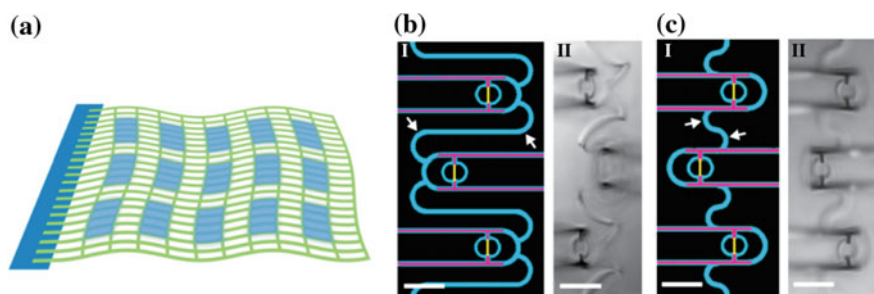


Fig. 4.11 Hierarchical nanoES. **a** Schematic showing the integration of periodic self-organized electronic domains (light blue) into a flexible mesh (green). In individual self-organized domains, the 3D device positions relative to the global flexible mesh can be controlled by their geometry designs. **b, c** Design patterns (I) and experimental data (II) for two self-organized units. SU8, metal and nanowires are shown in blue, pink and yellow in (b). Scale bars in **b** and **c**, 20 μm

4.3.3 NanoES/Tissue Scaffold Hybrids

The self-organized and mesh nanoES also were merged with conventional macroporous biomaterials. Specifically, gel casting, lyophilization and electrospinning were used to deposit and construct macroporous collagen (Fig. 4.12a), alginate (Fig. 4.12b), and poly(lactic-co-glycolic acid) (PLGA) (Fig. 4.12c), respectively, around nanoES. A confocal fluorescence microscopy image of a hybrid self-organized nanoES/collagen scaffold (Fig. 4.12a) shows clearly that the collagen nanofibers (green) are fully entangled with the nanoES, with no evidence of phase separation. SEM images of the open mesh nanoES/alginate hybrid scaffold produced by lyophilization (Fig. 4.12b) show that the flexible nanoES mesh is intimately anchored to the alginate framework, which has a similar pore structure as

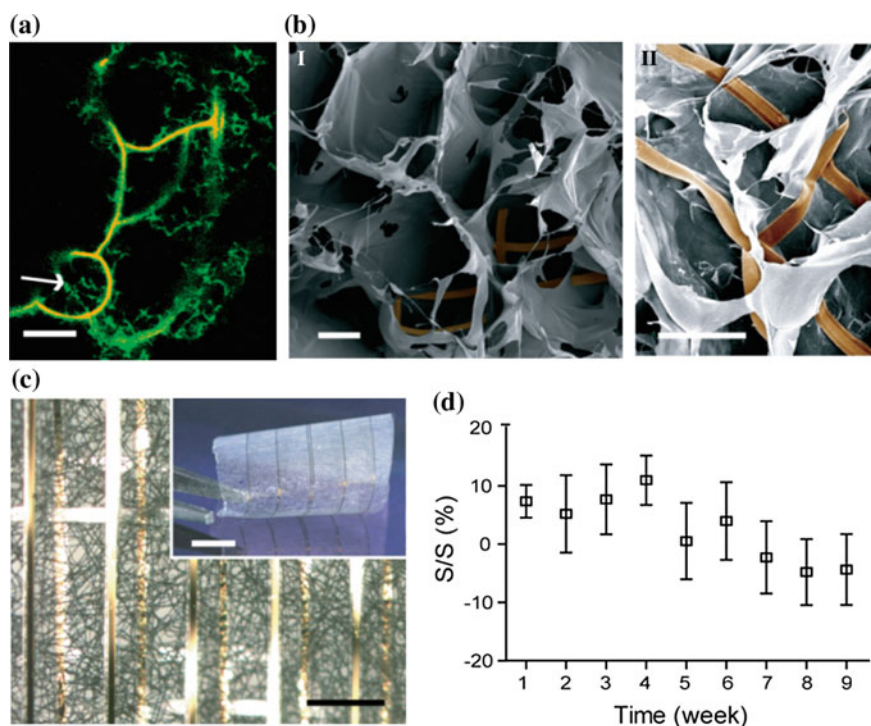


Fig. 4.12 Hybrid macroporous nanoelectronic scaffolds. **a** Confocal fluorescence micrograph of a hybrid 3D self-organized nanoES/collagen matrix. Green (Fluorescein isothiocyanate): collagen type-I, orange (rhodamine 6G): epoxy ribbons. White arrow marks the position of nanowire. Scale bar, 10 μm . **b** SEM images of mesh nanoES/alginate scaffold, top (**I**) and side (**II**) views. The epoxy ribbons from nanoES are false-colored in brown for clarity. Scale bars, 200 μm (**I**) and 100 μm (**II**). **c** A bright-field optical micrograph of the folded scaffold, showing multilayered structures of PLGA and nanoelectronic interconnects. Inset shows the photograph of the hybrid sheet before folding. Scale bars, 200 μm and 5 mm (inset). **d** Relative changes in nanowire FET sensitivity over time in culture. $n = 5$

the pure alginate scaffold prepared under similar conditions. Finally, optical microscopy images of a multilayered mesh nanoES/PLGA scaffold (Fig. 4.12c), which was prepared by electrospinning PLGA fibers on both sides of the nanoES and subsequent folding of the hybrid structure, highlights the intimate contact between nanoES mesh and PLGA fibers. The hybrid nanoES/biomaterial 3D scaffolds retain the original nanowire FET device characteristics. For example, measurements in $1 \times$ PBS solution showed that $\Delta G/G$ and $\Delta S/S$ were less than $\pm 9\%$ for mesh nanoES/PLGA composite versus bare nanoES. Hybrid nanoES were stable under cell culture conditions. For example, nanowire FET devices in the hybrid self-organized nanoES/Matrigel™ scaffold in neuron culture media (Fig. 4.12d) had $\Delta S/S < \pm 11\%$ over a 9 week period, suggesting a capability for long-term culture and monitoring with the nanoES. These results show that nanoES can be combined with conventional biomaterials to produce hybrid scaffolds that now provide nanoscale electrical sensory components distributed in 3D.

4.3.4 Characterization of NanoES/Tissue Interface

The hybrid nanoES were evaluated in 3D culture [29, 30] for several cell types. Embryonic rat hippocampal neurons were cultured in the self-organized nanoES/Matrigel™ for 7–21 days (Fig. 4.2). Reconstructed 3D confocal microscopy images from a 2-week culture (Fig. 4.13) showed neurons with a high density of spatially interconnected neurites that penetrated the self-organized nanoES (Fig. 4.13a), showing an integration between neural tissue and nanoES at subcellular scale (Fig. 4.13b–d). Notably, the widths of the scaffold elements (passivated metal interconnects and structural ribbons) were similar to those of the neurite projections, demonstrating the combination of electronics with biological systems at an unprecedented similarity in scale (Fig. 4.14).

3D nanoelectronic cardiac culture was achieved from hybrid mesh nanoES/PLGA scaffolds (Fig. 4.14). Confocal fluorescence microscopy of a cardiac 3D culture (Fig. 4.14b–d) revealed a high density of cardiomyocytes in close contact with nanoES components. Epi-fluorescence images of cardiac cells on the surface of the nanoES cardiac patch showed striations characteristic of cardiac tissue [30, 38] (Fig. 4.14e). In addition, the in vitro cytotoxicity of nanoES in 3D neural and cardiac culture was evaluated (Fig. 4.15). Differences between hippocampal neurons in self-organized nanoES/Matrigel™ versus Matrigel™ over 21 days, assessed with a standard live/dead cell assay [29] (Fig. 4.15a), and between cardiac cells in hybrid mesh nanoES/Matrigel™/PLGA and Matrigel™/PLGA from 2 to 12 days, measured with a metabolic activity assay (Fig. 4.15b) were minimal. These studies show that on 2–3 week time scale, the nanoES component of the scaffolds has little effect on cell viability, and thus could be exploited for a number of in vitro studies, including drug screening assays with these synthetic neural and cardiac tissues.

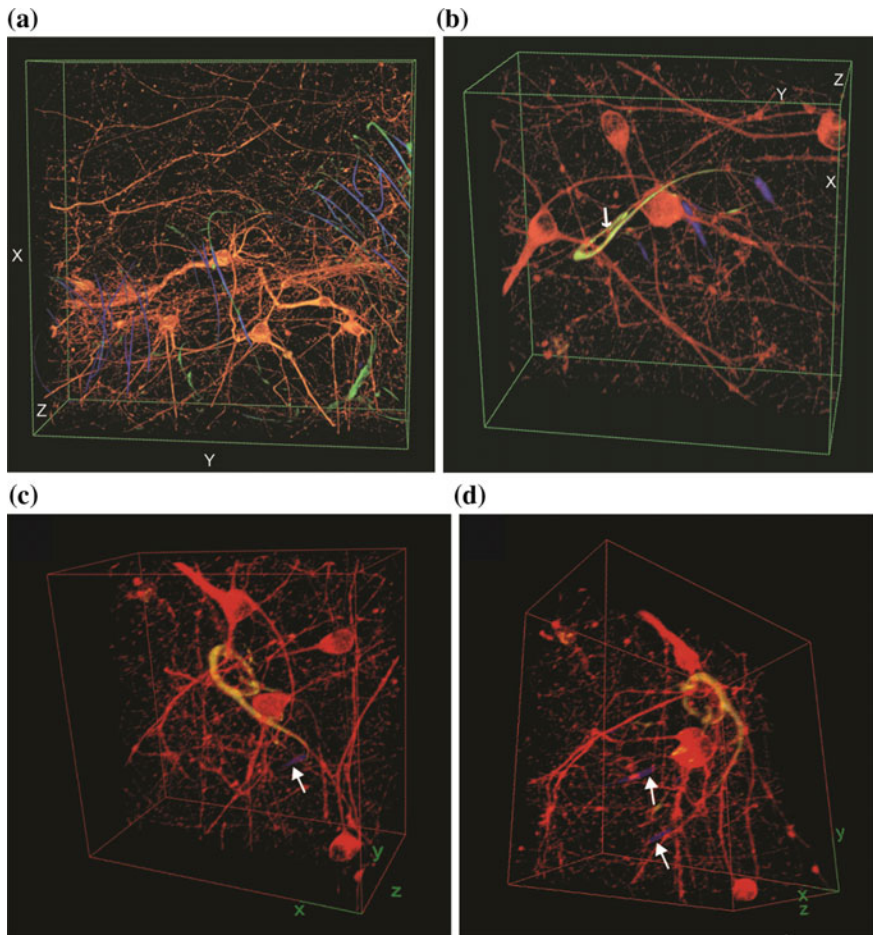


Fig. 4.13 NanoES innervated synthetic neural tissue. 3D reconstructed confocal images of rat hippocampal neurons after 2 week culture in Matrigel™ on self-organized nanoES. Red (Alexa Fluor® 546): neuronal β -tubulin, yellow (rhodamine 6G): epoxy ribbons. The metal interconnects are false-colored in blue, and are imaged in reflected light mode. White arrow highlights a neurite passing through a ring-like structure supporting a nanowire FET. Dimensions in **a** x: 317 μm ; y: 317 μm ; z: 100 μm ; in **b** x: 127 μm ; y: 127 μm ; z: 68 μm . **c, d** The images were rotated from the view shown in **(b)** approximately as follows: (left image) 90° about z-axis, -10° about y-axis; (right image) 90° about z-axis, 100° about y-axis, 40° about x-axis. Together, these images show unambiguously that neurites pass through the ring-like structures supporting individual nanowire FETs

Extended studies will be needed to evaluate the nanoES for longer-term implants, although the major component of nanoES, SU-8, has demonstrated long-term chronic biocompatibility suitable for in vivo recording [42, 43].

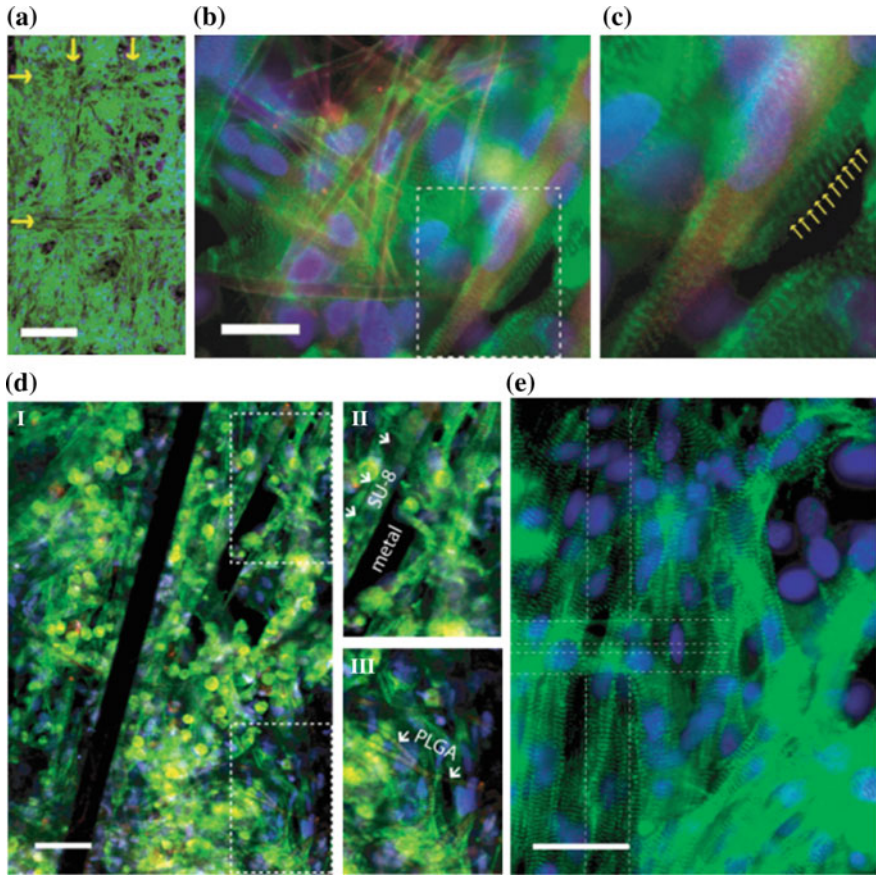


Fig. 4.14 NanoES innervated synthetic cardiac patch. **a, b** Images showing α -actinin of cardiomyocytes (green in **a–e**, Alexa Fluor[®] 488), cell nuclei (blue in **a–e**, Hoechst 34580) and PLGA fibers (red in **b–d**, rhodamine 6G). Dense cardiomyocyte growth was supported by both nanoES (marked by yellow arrows in **(a)**) and electrospun PLGA fibers in hybrid PLGA/nanoES in **(b)**. **c** is a zoomed view of the rectangular box in **(b)**, showing (yellow arrows) striated patterns of α -actinin (green). **d** Confocal fluorescence images of synthetic cardiac patch. **II** and **III** zoomed-in view of the upper and lower dashed regions in **I** showing metal interconnects, SU-8 scaffold (arrows in **II**), electrospun PLGA fibers (arrows in **III**). **e** Epi-fluorescence image of the surface of the cardiac patch. Green (Alexa Fluor[®] 488): α -actinin, blue (Hoechst 34580): cell nuclei. The position of the source-drain electrodes is outlined with dashed lines. Scale bar, 200 μm (**a**), 20 μm (**b**), 40 μm (**d**) and 40 μm (**e**)

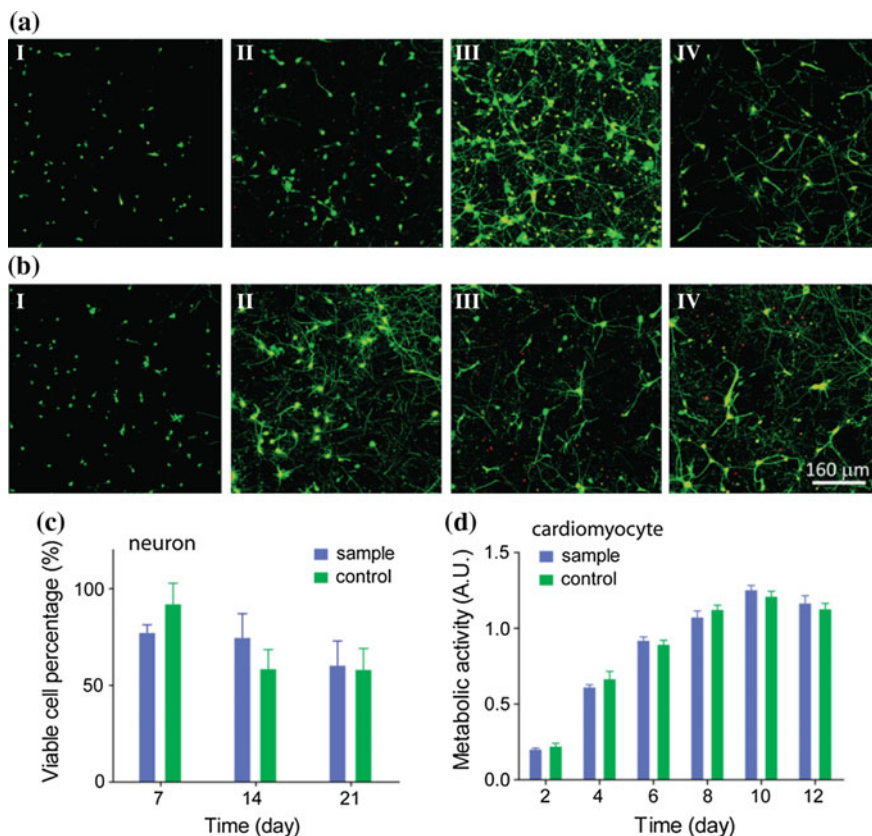
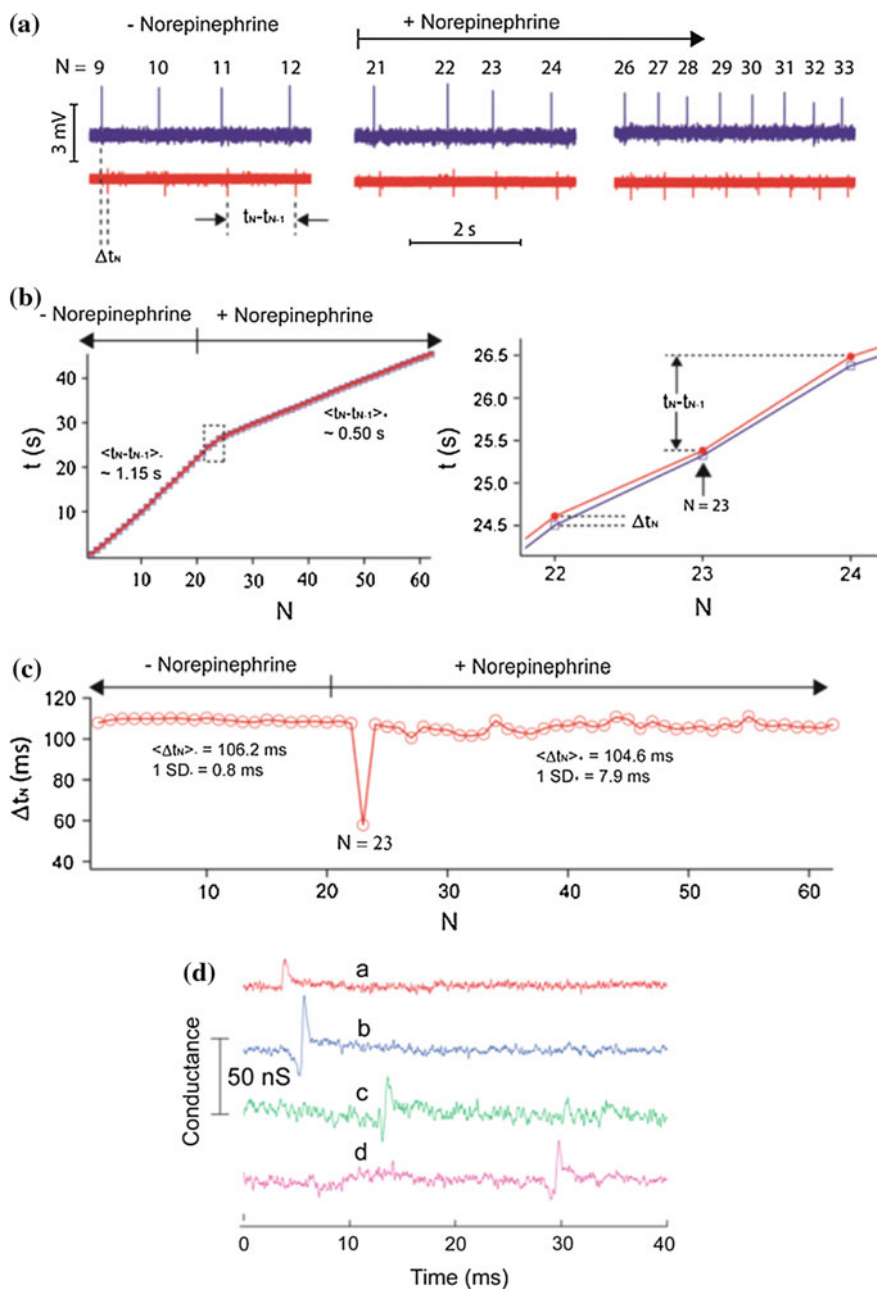


Fig. 4.15 Biocompatibility of nanoES. 50- μm projection confocal fluorescence images of neuron culture in MatrigelTM (a) versus nanoES/MatrigelTM (b). Neurons were labeled by LIVE/DEAD cytotoxicity assay after 0 days (I), 7 days (II), 14 days (III) and 21 days (IV) culture. c Percentage of viable hippocampal neurons cultured in nanoES/MatrigelTM versus MatrigelTM. Cell viability was evaluated with LIVE/DEAD cytotoxicity assay from (a, b). Cells were counted from 3D reconstructed confocal fluorescence photomicrographs. $n = 6$; data are means \pm SD. Differences between groups were very small although statistically significant ($p < 0.05$). d MTS cytotoxicity assay of cardiomyocytes evaluated using the MTS assay. $n = 6$; data are means \pm SD. Differences between groups were very small although statistically significant ($p < 0.05$).

4.3.5 Monitoring of Cell Activity Change to External Stimulations

We demonstrated the electrical recording capabilities of nanoES in a 3D cardiomyocyte/nanoES construct (Fig. 4.16a). Output recorded from a single nanowire FET inside construct showed regular spikes with ~ 1 Hz frequency, ~ 2 to 3 mV calibrated amplitude, ≥ 3 signal-to-noise (S/N) ratio, and ~ 2 ms width.



◀**Fig. 4.16** Multiplexed electrical recording from nanoES innervated synthetic cardiac patch. **a** Electrical recording traces from two devices in a cardiac patch, before (left), during (middle) and after (right) Norepinephrine application. We call Δt_N as the temporal difference between a pair of spikes from two devices, $t_N - t_{N-1}$ as the interval between consecutive spikes from a single device, N as the spike index. **b** The time (t) versus spike index (N) plot. The color coding for devices is the same as in **(a)**. The data show that the cells exhibit overall coherent beating and response to the drug. The right panel is the zoom-in view of the transition, where the middle point ($N = 23$) shows a decreased Δt_N compared to earlier and later spikes. **c** The Δt_N versus N plot. $\langle \Delta t_N \rangle$ and 1 SD (standard deviation) before (-) and after (+) norepinephrine application show that although the drug has minimum effect on $\langle \Delta t_N \rangle$, the sub-millisecond and millisecond fluctuations of Δt_N (1 SD) increase by ~ 10 fold following drug addition. Such stochastic variation suggests millisecond-level, heterogeneous cellular responses to the drug. **d** Multiplex electrical recording of extracellular field potentials from 4 nanowire FETs (**a–d**) in a mesh nanoES

The peak amplitude, shape, and width are consistent with extracellular recordings from cardiomyocytes [20]. We investigate the potential of the nanoES based 3D cardiac culture for monitoring appropriate pharmacological response by dosing the 3D cardiomyocyte mesh construct with norepinephrine, a drug that stimulates cardiac contraction via β_1 -adrenergic receptors [44]. Measurements from the same nanowire FET device showed a twofold increase in contraction frequency following drug application. Interestingly, recording from two nanowire FETs from the cardiac patch upon norepinephrine application showed sub-millisecond and millisecond level, heterogeneous cellular responses to the drug (Fig. 4.16a–c). Additionally, simultaneous recordings from 4 nanowire FETs with separations up to 6.8 mm in a nanoES/cardiac construct (Fig. 4.16d) demonstrated multiplexed sensing of a coherently beating cardiac patch, with sub-millisecond time resolution. Our current device design yields relatively sparse device distribution with 60 devices over a ca. $3.5 \times 1.5 \text{ cm}^2$ area. Increases in nanowire FET density, the use of cross-bar circuits and implementing multiplexing/demultiplexing for addressing [40], could allow the nanoES scaffolds to map cardiac and other synthetic tissue electrical activities over the entire constructs at high-density in 3D.

Last, we demonstrate multiplexing measurement of 3D response to chemical activation from nanoES/neural construct (Fig. 4.17). We stimulate the hybrid construct by applying glutamate to the culture medium. Recording from three devices in 3D self-organized that distributed from surface to the bottom of construct, we can observe sequential local field potential changes due to the diffusion of glutamate from surface into construct. Importantly, the slow diffusion of glutamate molecule into the construct demonstrates a seamless integration between nanoES and neural construct in 3D. Together these experiments suggest nanoES constructs can monitor in vitro the response to drugs from 3D tissue models, and thus have potential as a platform for in vitro pharmacological studies [9, 10].

We have also extended our approach towards development of artificial tissue with nanoES. Specifically, vascular nanoES constructs were prepared by processes analogous to those used for tissue engineered autologous blood vessels [31, 45] except the addition of the nanoES (Fig. 4.18). HASMCs were cultured on 2D mesh nanoES with sodium ascorbate to promote deposition of natural ECM. The hybrid

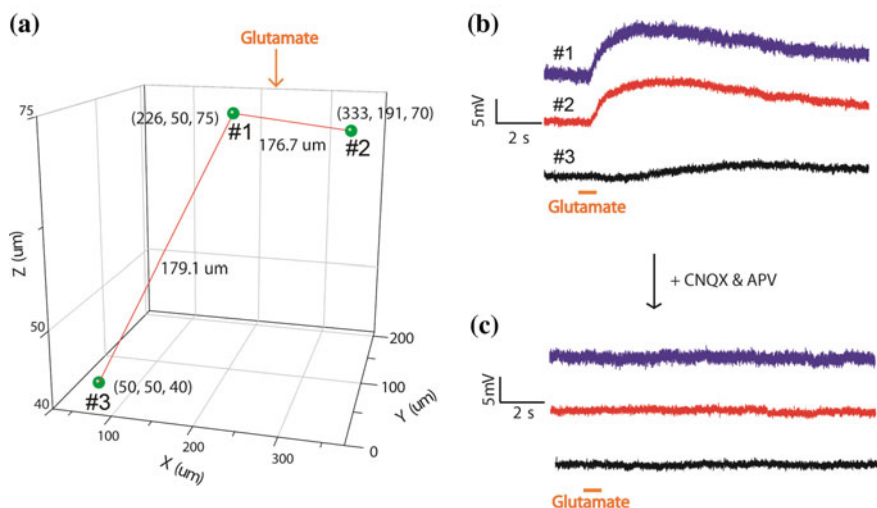


Fig. 4.17 Multiplexed 3D recording from hybrid self-organized nanoES/neural constructs. The hybrid nanoES/neural 3D construct was prepared by culturing neurons with a 3D self-organized device array for 14 days *in vitro* with a density of >4 million neurons/mL in Matrigel™. **a** Three nanowire FETs (labeled 1, 2 and 3) were distributed in the construct with x - y - z positions. **b** The local field potential changes recorded from three devices in the 3D neuron construct showed distinct position-dependent temporal responses following glutamate solution injection. **c** Perfusing 6-cyano-7-nitroquinoxaline-2,3-dione (CNQX) and D(-)-2-Amino-5-phosphonopentanoic acid (APV) blockers prior to glutamate addition eliminate any observed response, and thus show that the observed response in **(b)** can be attributed to postsynaptic signal propagation. The orange segments mark the timing when glutamate solution was injected (continued) **(b, c)**. The observed responses are consistent with the effects of glutamate, CNQX and APV

nanoES/HASMC sheets (Fig. 4.18b) were rolled into multi-layer 3D tubular structures and matured without macroscopic delamination or desquamation (Fig. 4.18c), and analyses showed that the cells expressed smooth muscle α -actin (Fig. 4.18d), the key contractile protein in smooth muscle [31].

We visualized the distribution of nanoES in the tubular construct by micro-computed tomography (μ CT). A projection of the reconstructed 3D μ CT data (Fig. 4.19a) revealed regularly spaced metal interconnects with at least four revolutions (arrows, Fig. 4.19a, II), consistent with the nanowire FET mesh and tissue rolling. Analyses of hematoxylin-eosin-stained sections (Fig. 4.19b) revealed smooth muscle tissue ~ 200 μ m thick, with elongated cells and collagenous nanofibers, and embedded SU-8 ribbons from the nanoES (Fig. 4.19b). These findings confirm 3D integration of nanowire FET nanoelectronics with healthy smooth muscle.

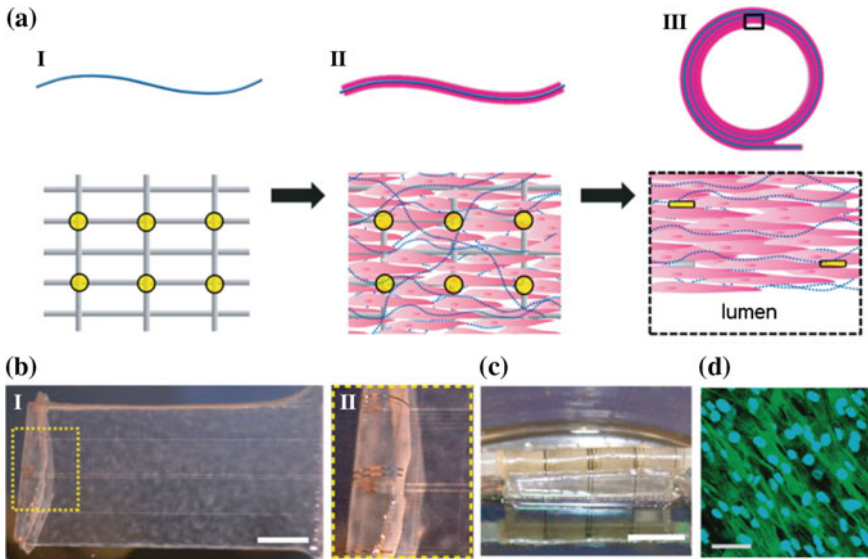


Fig. 4.18 Mesh nanoES innervated synthetic vascular construct. **a** Schematic of the synthesis of smooth muscle nanoES. The upper panels are side views, while the lower ones are either top views (**I** and **II**) or zoom-in view (**III**). Grey: mesh nanoES, blue fibers collagenous matrix secreted by HASMC, yellow dots: nanowire FETs, pink: HASMC. **b, I**, Photograph of a single HASMC sheet cultured with sodium L-ascorbate (continued) on a nanoES. **II**, Zoomed-in view of the dashed area in (**I**), showing metallic interconnects macroscopically integrated with cellular sheet. **c** Photograph of the vascular construct after rolling into a tube and maturation in a culture chamber for 3 weeks. **d** Confocal fluorescence microscopy image from the surface of the HASMC/mesh-like nanoelectronics biomaterial shows α -actin (green, Alexa Fluor[®] 488) and cell nuclei (blue, Hoechst 34580) in smooth muscle cells. Local alignment of HASMCs is revealed by anisotropy in α -actin fibers running from upper left to lower right of image. Scale bars, 40 μm

We demonstrated the potential of this vascular construct to function as a biomedical device by a 3D pH sensing experiment (Fig. 4.19c). As the extravascular pH was varied stepwise with luminal pH fixed, simultaneous recordings from nanowire FETs in the outermost layer showed stepwise conductance decreases with a sensitivity of ~ 32 mV/pH. Nanowire FETs in the innermost layer (closest to luminal) showed minor baseline fluctuations. This ability to resolve extravascular pH changes makes possible detection of inflammation, ischemia, tumor microenvironments or other forms of metabolic acidosis due to overproduction of organic acids or impaired renal acidification [46, 47].

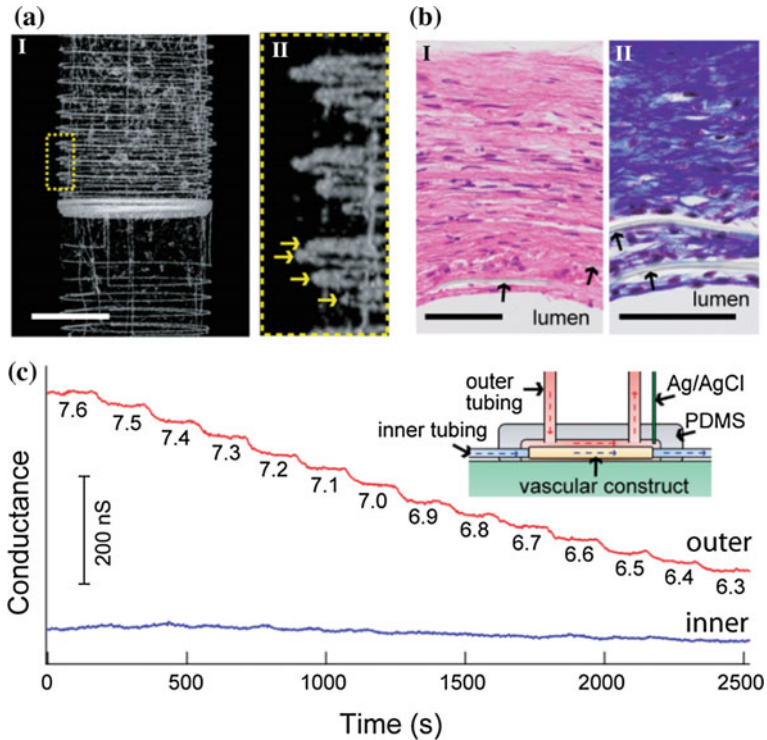


Fig. 4.19 Synthetic vascular construct enabled pH sensing. **a, I.** Micro-computed tomograph of a tubular construct segment. **II.** Zoomed-in view of (I). Arrows mark the individual nanowire FET-containing layers of the rolled construct. Scale bar, 1 mm. **b** Hematoxylin & eosin (I) and Masson Trichrome (II; collagen is blue) stained sections (~6 μm thick) cut perpendicular to the tube axis; lumen regions are labeled. Arrows mark the positions of SU-8 ribbons of the nanoES. Scale bars, 50 μm. **c** Changes in conductance over time for two nanowire FET devices located in the outermost (red) and innermost (blue) layers. Inset: schematic of the experimental set-up. Outer tubing delivered bathing solutions with varying pH (red dashed lines and arrows); inner tubing delivered solutions fixed pH (blue dashed lines and arrows)

4.4 Conclusion

The nanoES concept and implementations described here represent a new direction in merging nanoelectronics with biological systems since we have demonstrated 3D macroporous material/device platform that is distinct from either engineered tissue [6, 48] or flexible electronics [13–17, 49–51]. Looking forward, there are several areas to develop. Cell interactions with nanoES could be tuned by modification of the nanoES with growth determinants [6, 30]. In addition, the elements in the nanoES could be expanded to incorporate nanoscale stimulators and stretchable designs to provide electrical and mechanical stimulation to enhance cell culture.

Bibliography

1. Na K et al (2011) Directing zeolite structures into hierarchically nanoporous architectures. *Science* 333:328–332
2. Schaedler TA et al (2011) Ultralight metallic microlattices. *Science* 334:962–965
3. Place ES, George JH, Williams CK, Stevens MM (2009) Synthetic polymer scaffolds for tissue engineering. *Chem Soc Rev* 38:1139
4. Wylie RG, Ahsan S, Aizawa Y, Maxwell KL, Morshead CM, Shoichet MS (2011) Spatially controlled simultaneous patterning of multiple growth factors in three-dimensional hydrogels. *Nat Mater* 10:799
5. Kloxin AM, Kasko AM, Salinas CN, Anseth KS (2009) Photodegradable hydrogels for dynamic tuning of physical and chemical properties. *Science* 324:59
6. Dvir T, Timko BP, Kohane DS, Langer R (2011) Nanotechnological strategies for engineering complex tissues. *Nat Nanotechnol* 6:13
7. Kraehenbuehl TP, Langer R, Ferreira L (2011) Three-dimensional biomaterials for the study of human pluripotent stem cells. *Nat Meth* 8:731
8. Hutmacher DW (2010) Biomaterials offer cancer research the third dimension. *Nat Mater* 9:90
9. Huh D et al (2010) Reconstituting organ-level lung functions on a chip. *Science* 328:1662
10. Baker M (2011) Tissue models: A living system on a chip. *Nature* 471:661
11. Schwille P (2011) Bottom-up synthetic biology: Engineering in a Tinkerer's world. *Science* 333:1252
12. Ruder WC, Lu T, Collins JJ (2011) Synthetic biology moving into the clinic. *Science* 333:1248
13. Timko BP et al (2009) Electrical recording from hearts with flexible nanowire device arrays. *Nano Lett* 9:914
14. Viventi J et al (2010) A conformal, bio-interfaced class of silicon electronics for mapping cardiac electrophysiology. *Transl Med* 2:24ra22
15. Kim DH et al (2011) Materials for multifunctional balloon catheters with capabilities in cardiac electrophysiological mapping and ablation therapy. *Nat Mater* 10:316
16. Viventi J et al (2011) Flexible, foldable, actively multiplexed, high-density electrode array for mapping brain activity in vivo. *Nat Neurosci* 14:1599
17. Kim DH et al (2011) Epidermal electronics. *Science* 333:838
18. Tian B, Cohen-Karni T, Qing Q, Duan X, Xie P, Lieber CM (2010) Three-dimensional, flexible nanoscale field-effect transistors as localized bioprobes. *Science* 329:831
19. Qing Q et al (2010) Nanowire transistor arrays for mapping neural circuits in acute brain slices. *Proc Natl Acad Sci USA* 107:1882
20. Cohen-Karni T, Timko BP, Weiss LE, Lieber CM (2009) Flexible electrical recording from cells using nanowire transistor arrays. *Proc Natl Acad Sci USA* 106:7309
21. Timko BP, Cohen-Karni T, Qing Q, Tian B, Lieber CM (2010) Design and implementation of functional nanoelectronic interfaces with biomolecules, cells, and tissue using nanowire device arrays. *IEEE Trans Nanotechnol* 9:269
22. Prohaska OJ, Olcaytug F, Pfundner P, Dragaun H (1986) Thin-film multiple electrode probes: Possibilities and limitations. *IEEE T Bio-Med Eng BME* 33:223
23. Nicolelis, MAL (ed) *Methods for neural ensemble recordings*, 2nd edn. CRC Press, Boca Raton (FL)
24. McKnight TE et al (2006) Resident neuroelectrochemical interfacing using carbon nanofibre arrays. *J Phys Chem B* 110:15317
25. Yu Z et al (2007) Vertically aligned carbon nanofibre arrays record electrophysiological signals from hippocampal slices. *Nano Lett* 7:2188
26. Aviss KJ, Gough JE, Downes S (2010) Aligned electrospun polymer fibres for skeletal muscle regeneration. *Euro Cells Mater* 19:193

27. Timoshenko S, Woinowsky-Krieger S (1959) Theory of plates and shells, 2nd edn. McGraw-Hill Inc., p 4–6
28. http://www.genlantis.com/objects/catalog/product/extras/1285_N100200_NeuroPure_E18_Hippocampal_Cells_MV25April2007.pdf
29. Xu T, Molnar P, Gregory C, Das M, Boland T, Hickman JJ (2009) Electrophysiological characterization of embryonic hippocampal neurons cultured in a 3D collagen hydrogel. *Biomaterials* 30:4377
30. Sapir Y, Kryukov O, Cohen S (2011) Integration of multiple cell-matrix interactions into alginate scaffolds for promoting cardiac tissue regeneration. *Biomaterials* 32:1838
31. L'Heureux N, Pâquet S, Labbé R, Germain L, Auger FA (1998) A completely biological tissue-engineered human blood vessel. *FASEB J* 12:47
32. Pautot S, Wyart C, Isacoff EY (2008) Colloid-guided assembly of oriented 3D neuronal networks. *Nat Meth* 5:735
33. Kiernan JA (2008) *Histological and histochemical methods: theory and practice*, 4th edn. Scion Publishing Ltd.
34. <http://www.polysciences.com/SiteData/docs/872/4dfadd3f92e8e02f9ac9638745201f/872.pdf>
35. Prabhakaran MP, Kai D, Ghasemi-Mobarakeh L, Ramakrishna S (2011) Electrospun biocomposite nanofibrous patch for cardiac tissue engineering. *Biomed Mater* 6:055001
36. Dequach JA, Yuan SH, Goldstein LS, Christman KL (2011) Decellularized porcine brain matrix for cell culture and tissue engineering scaffolds. *Tissue Eng Part A* 17:2583
37. Hanley PJ, Young AA, LeGrice IJ, Edgar SG, Loiselle DS (1999) 3-Dimensional configuration of perimysial collagen fibres in rat cardiac muscle at resting and extended sarcomere lengths. *J Physiol* 517:831
38. Engelmayr GC Jr et al (2008) Accordion-like honeycombs for tissue engineering of cardiac anisotropy. *Nat Mater* 7:1003
39. Lu W, Lieber CM (2007) Nanoelectronics from the bottom up. *Nat Mater* 6:841
40. Yan H et al (2011) Programmable nanowire circuits for nanoprocessors. *Nature* 470:240
41. Wang MF, Maleki T, Ziaie B (2008) Enhanced three-dimensional folding of 53 silicon microstructures via thermal shrinkage of a composite organic/inorganic 54 bilayer. *IEEE/ASME J Microelectromech Syst* 17:882
42. Cho SH et al (2008) Biocompatible SU-8-based microprobes for recording neural spike signals from regenerated peripheral nerve fibres. *IEEE Sensors J* 8:1830
43. Voskerician G et al (2003) Biocompatibility and biofouling of MEMS drug delivery devices. *Biomaterials* 24:1959
44. Zipes DP, Jalife J (2009) *Cardiac electrophysiology: from cell to bedside*, 5th edn. Saunders, Philadelphia, PA
45. L'Heureux N et al (2006) Human tissue-engineered blood vessels for adult arterial revascularization. *Nat Med* 12:361
46. Neri D, Supuran CT (2011) Interfering with pH regulation in tumours as a therapeutic strategy. *Nat Rev Drug Discov* 10:767
47. Kraut JA, Madias NE (2010) Metabolic acidosis: pathophysiology, diagnosis and management. *Nat Rev Nephrol* 6:274
48. Dvir T et al (2011) Nanowired three-dimensional cardiac patches. *Nat Nanotechnol* 6:720
49. Sekitani T et al (2008) A rubberlike stretchable active matrix using elastic conductors. *Science* 321:1468
50. Mannsfeld SCB et al (2010) Highly sensitive flexible pressure sensors with micro-structured rubber as the dielectric layer. *Nat Mater* 9:859
51. Takei K et al (2010) Nanowire active matrix circuitry for low-voltage macro-scale artificial skin. *Nat Mater* 9:821

Chapter 5

Syringe Injectable Electronics

5.1 Introduction

With recent advancement in nanotechnology and materials science [1, 2], we have been able to fabricate electronics on flexible, stretchable and 3D substrates to cover electrical functional units on soft and non-planar surfaces for monitoring, control and making smart systems [3–12]. New requirements have been raised that electronics need to be implemented into objects with a minimal invasiveness followed by a 3D distribution of nano- and micro-scale sensor units in a large volume while maintaining mechanical ultra-flexibility [13, 14]. This is especially important for the field of bioelectronics, which require a seamlessly integration of electronics with behaving animal at single cellular level throughout the whole tissue. Previous chapters have shown examples involving construction of 3D soft electronic networks and building of polymers or synthetic tissues within electronic networks, yet, these examples are not applicable to existing objects and behaving animals [8]. In addition, while we can use rigid substrates to deliver electronics into targeted objects and release electronics from that substrate; however, these methods introduce significant damage from the insertion of rigid substrate materials further precluding a minimal invasive process [13].

Here we introduce a new strategy to meet those requirements through encapsulating electronics units into a freestanding mesh polymeric network, delivering these electronics into target system via a minimal invasive syringe-injection process that has been widely used in clinic medicine [15–18] and restoring injected electronics to their original geometric configuration. In this study, silicon nanowires [19, 20] were used as semiconductor components and metal electrodes [21] were used as electrical sensing units given their nano- and micro-scale structure, multi-functionalities and electrical and chemical recording capability.

5.2 Experimental

5.2.1 Freestanding Mesh Electronics Fabrication

Uniform single-crystalline nanowires were synthesized using the Au nanocluster-catalyzed vapor–liquid–solid growth mechanism in a home-built CVD system described previously [22]. Key steps in the fabrication of freestanding mesh electronics were discussed in previous chapters, in brief [14]: (1) Thermal deposition were used to deposit a 100-nm nickel metal layer over the whole silicon wafer, where the nickel served as the final relief layer for freestanding electronics. (2) A 300- to 400-nm layer of SU-8 photoresist was spin cast over the entire chip. (3) Photolithography and developing process was used to pattern the bottom SU-8 layer for passivating and supporting the whole device structure. (4) A 300- to 400-nm layer of SU-8 photoresist was spin cast over the entire chip, then (5) the synthesized nanowires were directly printed from growth wafer over the SU-8 layer by the contact printing. Photolithography and developing process was used to define regular SU-8 patterns for immobilizing nanowires. (6) To fabricate metal electrode electrophysiological sensor, photolithography and electron beam deposition were used to define and deposit $20 \times 20 \mu\text{m}^2$ Pt pad. (7) Photolithography and thermal deposition were used to define and deposit the metal contact to address each nanowire device and form interconnections to the input/output pads for the array. Symmetrical Cr/Pd/Cr (1.5/50–80/1.5 nm) metal was sequentially deposited followed by metal liftoff to define metal contact for semiconductor. Symmetrical Cr/Au/Cr (1.5/50–80/1.5 nm) metal was sequentially deposited followed by metal liftoff to define global interconnects. Nonsymmetrical Cr/Pd/Cr (1.5/50–80/50–80 nm) metal was sequentially deposited followed by metal liftoff to define mechanics-driven self-organized region as described in previous chapters. (8) A 300- to 400-nm layer of SU-8 photoresist was spin cast over the entire chip and photopatterned as the top passivation layer (9) A 300- and 500-nm thick layers of LOR 3A and S1805 photoresist can be deposited by spin-coating and defined by photolithography to further protect the device region if necessary [23]. (10) The 2D syringe injectable electronics were released from the substrate by etching of the nickel layer. (11) If the device region was protected by photoresist protection layer, electronics need to be transferred into deionized (DI) water for rinsing and then dried on substrate, exposed in ultraviolet light to sensitize the photoresist protection with subsequently immersed in developer solution to dissolve the protection on device region. The structure of the mesh electronics is in Fig. 5.1.

5.2.2 Mesh Structure Design

General mesh electronics: Design of mesh structure is illustrated in Fig. 5.2. We call the ribbon along the injection direction as the longitudinal ribbon and call the

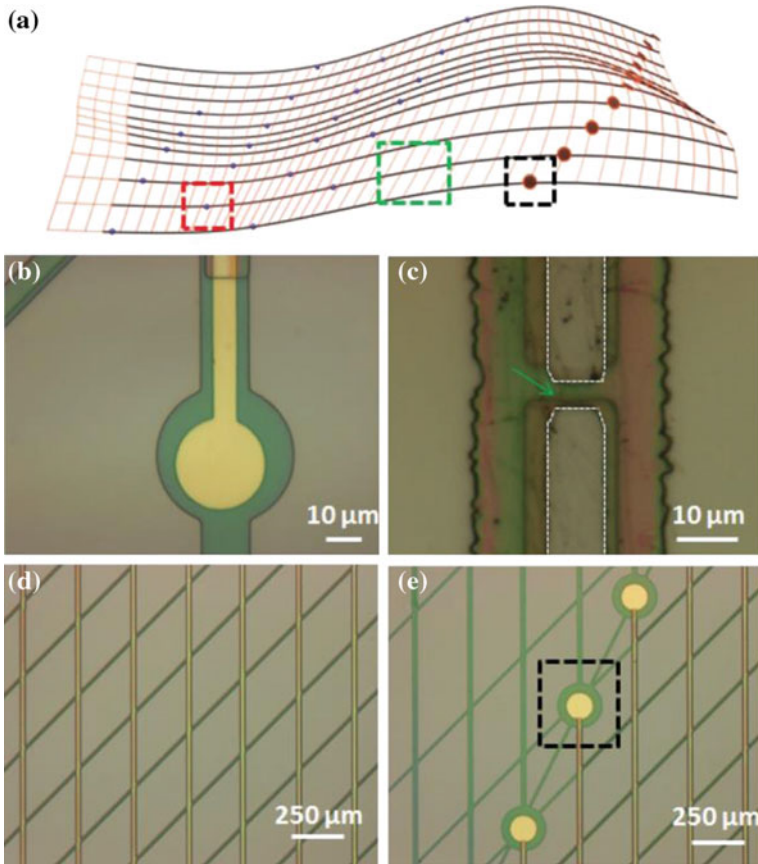
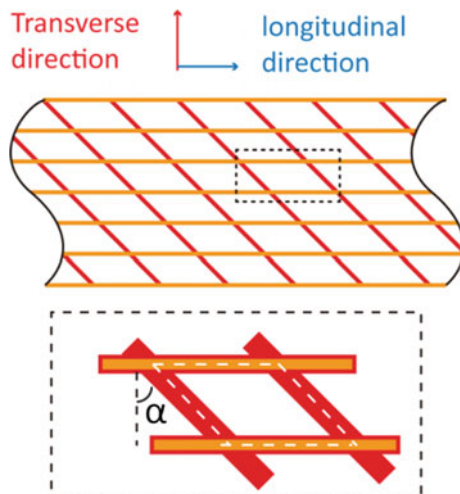


Fig. 5.1 Optical images of electronics structure. **a** Schematics of injectable electronics. Black, metal contact and I/O pads; orange, supporting polymer and blue, device. **b** Optical image of passive metal electrode. **c** Optical image of nanowire FET (indicated by green arrow) device. Source-drain electrodes are highlighted by white dashed lines. **d** Optical image of mesh region on the mesh corresponds to green dashed box in **a**. **e** Optical image of I/O pads corresponds to black dashed box in **a**

ribbon perpendicular to the injection direction as the transverse ribbon. Transverse ribbons are tilted with $\alpha = 45^\circ$ to transverse direction on the mesh plane. Metal contacts are mainly encapsulated in longitudinal ribbons. For active electronics, some transverse ribbons also contain metal contacts to form the S/D electrodes of FET. For passive metal electrode electronics, only longitudinal ribbons contain metal contacts. Silicon nanowire devices and passive metal electrodes are patterned either on the longitudinal ribbons in the center of unit cells or patterned separately in a beam in the longitudinal direction on the transverse ribbons in the center of unit cells to reduce strains for device during injection. For the ribbons containing metal contact lines, 100-nm thick metal lines are encapsulated in the middle of two

Fig. 5.2 Schematics of mesh design. Schematics show the structures of 2 different mesh designs. Black dashed boxes highlight the unit cell structure. Red, supporting and passivation polymer and yellow, metal lines



350-nm thick SU-8 layers. For the ribbons without metal contact lines, the total SU-8 thickness is ca. 700 nm. Transverse ribbons and longitudinal ribbons together form mesh with periodic unit cells. The dimensions of all unit cells are identical across the whole mesh. Design #1 is used for injection by needle with inner diameter larger than 200 μm . The width of mesh is 5–15 mm. The length of unit cell is 333 μm and width of unit cell is 250 μm . All the SU-8 layers are 20 μm in width and all the metal layers are 10 μm in width. Design #2 is used for injection by needle with inner diameter smaller than 200 μm . The width of mesh is 2–5 mm. The length of unit cell is 333 μm and width of unit cell is 250 μm . SU-8 layers in longitudinal ribbons are 20 μm in width and SU-8 layers in transverse ribbons are 5–10 μm in width. Metal layers in longitudinal ribbons are 10 μm in width and metal layers in transverse ribbons are 2–5 μm in width.

Control mesh electronics sample: The transverse ribbons are perpendicular to the longitudinal ribbons with $\alpha = 0^\circ$ to form an orthogonal mesh with the same periodic unit cell structure. All metal line patterns, thickness and width of ribbons are the same as design #1 of tilted transverse ribbons electronics. The width of electronics is 5–15 mm for testing.

Control thin film electronics sample: The thickness of SU-8 is 700 nm. All the metal line patterns are the same as design #1 of tilted mesh electronics. The width of electronics is 0.1–5 mm.

5.2.3 Injection of Mesh Electronics

Surface modification of electronics for syringe injectable: The freestanding electronics was transferred into DI water by glass pipette to remove nickel etchant or developer solution. Then the electronics was transferred and soaked into

poly-D-lysine aqueous solution for 2–12 h at 25 °C for surface modification. After surface modification, electronics was transferred into PBS buffer solution for future use.

Glass needle and fluidic channel preparation: Glass needle was prepared by using a conventional pipette puller and glass tube following the parameters: Heat: Ramp + 25, Pull: 0, Velocity: 140, Time: 100 and Pressure: 200. For a clean-cut needle with inner diameter from 20 to 200 μm , a ceramic tile was used to score the glass tip checked by optical microscope with subsequent mechanical break.

For the channels used for imaging, the pulling was halted and suspended in the middle to not completely break the glass tube. The channel size was measured by confocal fluorescence imaging. Rodamine-6G solution was filled into the channel for imaging. For a channel inner diameter smaller than 300 μm , epoxy glue was used to increase stability of channel preventing channel broken during imaging.

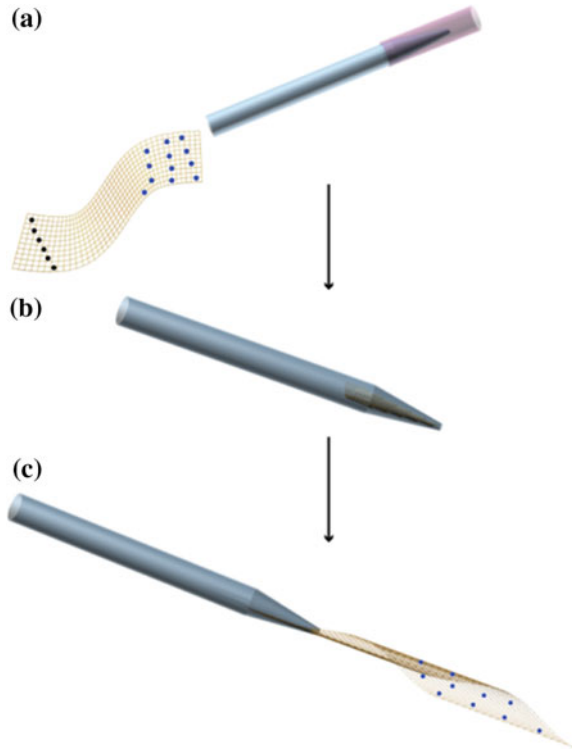
Injection by metal gauge needles: After surface modification, mesh electronics was transferred into syringe with metal gauge needle by a glass. It is very important to keep the orientation and unfolded structure of the electronics in the syringe to prevent any buckles, and allow electronics to be loaded into the needle from its tip region.

Injection by glass needle: To better control the injection through a small glass needle, a microinjector and a patch-clamp set-up were used to control the injection process. Mesh electronics was directly loaded into the glass needle illustrated by Fig. 5.3 as following: (1) A plastic tube was connected from the tip end of glass needle to a syringe. (2) Mesh electronics was drawn in into the rear part of glass needle. It is very important to load the electronics from its sharp tip to facilitate the folding of electronics in the glass tube and keep an extended structure to prevent buckles. (3) The plastic tube was removed from glass needle and the needle was mounted onto patch-clamp set-up and connected to micro-injector or syringe for injection.

Injection of mesh electronics in cavity: PDMS pre-polymer components were prepared in a 10:1 weight ratio at first, and diluted by hexane in a 1:3 (PDMS: hexane) volume ratio. The cavity for injection was formed by two pieces of cured PDMS. Mesh electronics was transferred from water to ethanol, dissolved in PDMS/hexane solution and then loaded into glass syringe with a 18 gauge metal needle. The sensor region of mesh electronics was injected into the cavity and the I/O region was ejected outside the cavity on a silicon or glass side. Hexane was used to wash away PDMS residues to unfold I/O region. The interconnect part of mesh electronics from the PDMS to the substrate was fixed by Kwik-Sil silicone elastomers to avoid damage during the drying process. Finally, the hybrid structure of PDMS and electronics was cured at room temperature for 48 h.

Injection of mesh electronics in MatrigelTM: Poly-D-lysine modified mesh electronics was transferred into PBS solution and then into the NeurobasalTM medium. Electronics was loaded into metal syringe needle as described above. MatrigelTM was diluted into 30% (v/v) with neuron culture medium and polymerized at 37 °C. Electronics was injected into polymerized Matrigel. The hybrid

Fig. 5.3 Loading in needle. Schematics show how the mesh electronics was stepwise loaded into glass needle. Blue, glass needle; pink, plastic tube; yellow, injectable electronics; black, I/O pads and blue, nanowire devices. **a** The tip of glass needle was connected to syringe by plastic tube. Injectable electronics was sucked in from the end of glass needle. **b** Electronics was loaded into glass needle. **c** Glass needle was mounted to patch-clamp setup for injection



structure was incubated in 37 °C to investigate the unfolding of electronics in MatrigelTM.

Co-inject mesh electronics with cells: Hippocampal neurons were prepared using a standard protocol described previously [4]. Cells were isolated by centrifugation at 200 g for 1 min and then resuspended in 5–10 mg/ml MatrigelTM at 4 °C. MatrigelTM with neurons were mixed with electronics at 4 °C and then loaded into syringe with metal gauge needle. Mesh electronics and neurons were co-injected into 30% (v/v) polymerized MatrigelTM in a culture plate and then placed in the incubator to allow the MatrigelTM to cure at 37 °C for 20 min. Then 1.5 mL of NeuroPure plating medium was added. After 1 day, the plating medium was changed to NeurobasalTM medium supplemented with B27, GlutamaxTM and 0.1% Gentamicin reagent solution. The in vitro co-cultures were maintained at 37 °C with 5% CO₂ for 14 days, with medium changed every 4–6 days.

5.2.4 Injection of Mesh Electronics into Behaving Animals

Animal preparation: Adult (25–35 g) male C57BL/6J mice (Jackson lab) were group-housed, giving access to food pellets and water ad libitum and maintained on

a 12 h: 12 h light: dark cycle. All animals were held in a facility beside lab 1 week prior to surgery, post-surgery and throughout the duration of the behavioral assays to minimize stress from transportation and disruption from foot traffic. All procedures were approved by the Animal Care and Use Committee of Harvard University and conformed to US National Institutes of Health guidelines.

Stereotaxic surgery: After animals were acclimatized to the holding facility for more than 1 week, they were anesthetized with a mixture of 60 mg/kg of ketamine and 0.5 mg/kg medetomidine administered intraperitoneal injection, with 0.03 mL update injections of ketamine to maintain anesthesia during surgery. A heating pad (at 37 °C) was placed underneath the body to provide warmth during surgery. Depth of anesthesia was monitored by pinching the animal's feet periodically. Animal was placed in a stereotaxic frame. 1 mm longitudinal incision was made and skin was resected from the center axis of the skull to expose a 2 mm by 2 mm portion of the skull. The dura was incised and resected from the surface of the skull. Next, a 0.5 mm diameter hole was drilled into the frontal and parietal skull plates using a dental drill. Sterile saline was swabbed on the brain surface to keep it moist throughout the surgery. Stereotaxic arm was used to clamp needle containing the injectable electronics. Mesh electronic was loaded into the glass needle with a diameter of 100–200 μm as described above. The glass needle was then mounted to a patch-clamp setup and lowered approximately 1 mm into the skull (Interaural: 6.16 mm, Bregma: -3.84 mm) for injection. After injection, needle is drawn out of the brain tissue and the I/O region was ejected on the surface of the skull.

After bonding with flexible cable by ACF bonding as described above, skins retracted from the center axis were replaced and the incision was sealed with a C&B-METABOND. Anti-inflammatory and anti-bacterial ointments were swabbed onto the skin after surgery. A 0.3 mL intraperitoneal injection of Buprenex for 0.1 mg/kg was administered to reduce post-operative pain. Animals were observed for four hours after surgery. Hydrogel was provided as food. Heating pad was used to maintain a 37 °C warm bath for the remainder of post-operative care. All procedures complied with the United States Department of Agriculture guidelines for the care and use of laboratory animals and were approved by the Harvard University Office for Animal Welfare.

Incubation and behavioral analysis: Animal was cared for every day for 3 days after the surgery and every other day after first 3 days. Animal was administered with 0.3 mL of Buprenex (0.1 mg/kg, diluted with 0.5 mL PBS) every 12 h for 3 days. Animal was also observed every other day for behavioral changes. Animals, which were surgically operated on, were housed individually in cage with food and water ad libitum. The room was maintained at constant temperature on a 12–12 h light-dark cycle.

5.2.5 Mechanical Analysis

Bending stiffness: We estimate the bending stiffness of the devices with different structures by finite element software ABAQUS. A unit cell is used for the simulation, and the tilt angle α is defined in Fig. 5.1. The devices are modeled with shell elements. The longitudinal ribbons are partitioned into a one-layer part and a three-layer part. A homogeneous section with 700- μm thick SU-8 is assigned to the transverse ribbons, while a composite section with three layers of 300-nm thick SU8, 100-nm thick gold and another 300-nm thick SU-8 is assigned to the three-layer part of the longitudinal ribbons. Both SU-8 and gold are modeled as linear elastic material, with Young's modulus 2 and 79 Gpa respectively [12]. To calculate the longitudinal and transverse bending stiffness, a fixed boundary condition is set at one of the ends parallel with the bending direction, and a small vertical displacement, d , is added at the other end. The external work, W , to bend the device is calculated. We define the effective bending stiffness of the device as the stiffness required of a homogenous beam to achieve the same external work W under the displacement d . Therefore, the effective bending stiffness per width of the device can be estimated as

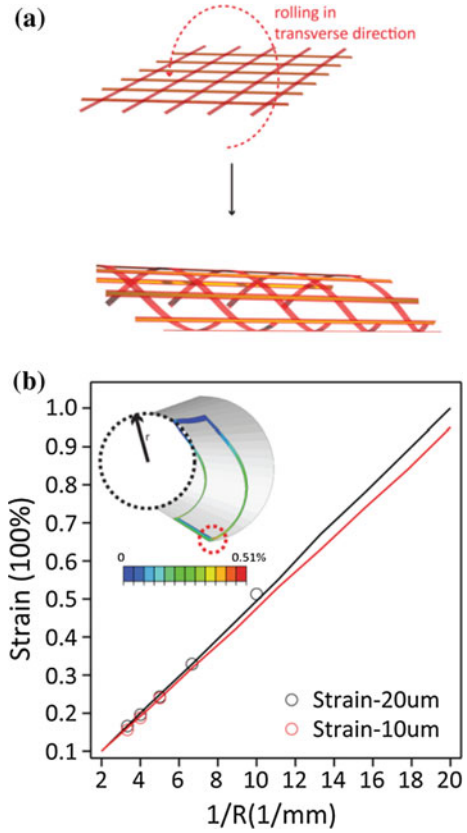
$$D = \frac{2Wl^3}{3d^2b}, \quad (5.1)$$

with b the width of the unit cell parallel with the bending direction, and l the length of the unit cell perpendicular to the bending direction.

Injection process: We further simulate a unit cell with the tilted angle $\alpha = 45^\circ$ going through a needle (Fig. 5.4a). The unit cell is bent by a rigid shell with radius of curvature R (Fig. 5.4b). A fixed boundary condition is set on one of the end of the device parallel with the bending direction. The distribution of the maximal principal strain ε_m is shown in the inset of Fig. 5.4b. When the radius of the needle R is 300 μm , the highest maximal principal strain is as small as 0.167%; when the radius of the needle R is 100 μm , ε_m reaches around 0.531%. The dependence of the highest maximal principal strain ε_m of the unit cell on the curvature $1/R$ is linear as shown in Fig. 5.4b. The two colors correspond to two different sizes of the mesh structures. The two corresponding fitting relations are $\varepsilon_m = 0.499/R$ and $\varepsilon_m = 0.473/R$ respectively.

Dimensional analysis of mesh electronics with cells: Flexibility of electronics implanted into biological system has been proved to be a critical factor for the level of provoked immunoresponse from the surrounding tissue, especially in long-term implantations [24]. If the structure of electronics is rigid, daily movements between electronics and tissues will introduce sever mechanical damage to the tissue. Here, we analyze this mechanical mismatch through definition of a dimensionless number $D/\gamma L^2$, where D is the bending stiffness per width of the ribbons in our mesh electronics or representing feature of other implantable electronics, γ is the membrane tension of cells and L is the length of the electronics. Since the bending

Fig. 5.4 Mechanics of mesh during rolling. **a** Schematics show that mesh roll up in transverse direction in needle. **b** Simulated highest strain value as functions of 1 over needle radius. Inset is a representative simulation shows the strain distribution of unit cell in 200- μm inner diameter needle. Red dashed circle highlights the point with highest strain. Black dashed circle and black arrow show the inner boundary and diameter of the needle



curvature of the electronics scales as $\sim 1/L$, the bending energy scales [25] as $\sim Dw/L$, with w is the width of the electronics. The surface membrane energy due to the insertion of the electronics scales as $\sim n\gamma wd$, with n is the number of cells on the electronics and d is the size of cells. Considering in the long-term implantation, the electronics will fully contact with tissue, then nd scales as $\sim L$. Therefore, the ratio of the bending energy and the surface energy gives the dimensionless number $D/\gamma L^2$, which describes the flexibility of electronics compared to the membrane tension of cells. Our mesh electronics have the properties of $D \sim 0.36 \text{ nN m}^{14}$ and $L \sim 300\text{--}500 \mu\text{m}$, and typical cells have $\gamma \sim 1 \text{ mN/m}^{26}$ and neuron cells measured by AFM have $\gamma \sim 0.01\text{--}0.4 \text{ mN/m}$ [26]. We can calculate $D/\gamma L^2$ is ca. 3.5–140. Given the elastic modulus of Si, carbon fiber, gold and SU-8 are 130 GPa [24], 234 GPa [27], 79 and 2 GPa [8], respectively, we can calculate the bending stiffness of previous reported Silicon microelectronic probe, carbon fiber probe and thin film electronics is ca. 4.6×10^{-5} , 9.2×10^{-5} and $1.3 \times 10^{-6} \text{ N m}$. The ratio of the bending energy and the surface energy calculated for injectable electronics is orders magnitude smaller than conventional silicon microelectronics ($1.15 \times 10^5\text{--}4.6 \times 10^6$) [24], carbon fiber probes ($2.3 \times 10^5\text{--}9.2 \times 10^6$) [28] and reported thin film electronics

(3.3×10^3 – 1.3×10^5) [10]. Therefore the design of injectable mesh electronics exhibits significantly more mechanical flexibility to cells and tissues showing unparalleled advantages as an implantable electronics.

5.2.6 Electrical Measurement

ACF bonding for electrical measurement: Mesh electronics were injected through syringe into solution, soft matters, biomaterials or tissues, with I/O part injected outside the target materials. DI water and other solvents (PBS, culture medium, hexane, etc.) were introduced to facilitate unfolding the I/O region, after which the I/O region was rinsed and dried with ethanol (Fig. 5.4). For the connection to measurement setup, the unfolded and dried I/O region of injectable electronics was bonded to the flexible cable (FFC/FPC Jumper Cables PREMO-FLEX, Molex, Lisle, IL) through an anisotropic conductive film (ACF, AC-4351Y, Hitachi Chemical Co. America, Ltd., Westborough, MA). ACF was 1.2 mm wide with conductive particles $\sim 3 \mu\text{m}$ in diameter. Firstly, an ACF with protective layer was positioned on the I/O region, and presealed after being heated to 90° and a pressure of 1 MPa for 1 min with a homemade hot bar or commercial bonding system (Fineplacer Lambda Manual Sub-Micron Flip-Chip Bonder, Finetech, Inc., Manchester, NH) to tack it on I/O part with protective layer removed. Then the flexible cable was placed on the ACF and aligned. At last, the endsealing was made with a temperature of 190 – 210°C in ACF and a pressure of 4 MPa on the top for 5 min applied by homemade hot bar or commercial bonding system. In order to demonstrate the adhesion strength of the interface between I/O pads and flexible cable, the structure was peeled from the substrate and examined by optical microscopy.

The connection resistance of ACF was measured to investigate the influence of bonding on electrical properties of devices (Fig. 5.4c, d). The conductance of each device was measured by probe station as R_0 and R_1 before and after ACF bonding, respectively. The connection resistance for each I/O pad (100 μm diameter) was calculated as $(R_1 - R_0)/2$, illustrated in Fig. 5.4c. The calculated connection resistance after ACF bonding with commercial bonder and homemade bonding is ca. 21.2Ω and ca. 33.7Ω respectively (Fig. 5.4d), below 0.05% of typical nanowire resistance and 0.03% of MEA device. The insulation resistance between I/O pads without circuits was over $10^{10} \Omega$. These measurements and calculation results demonstrated that ACF bonding had little influence on electrical properties of injectable electronics, which ensured reliable measurement of injectable electronics in many kinds of applications afterwards.

Yield of injection: To obtain the yield of electronics after injection, conductance of nanowire devices before and after injection through needles was compared as following procedure: (1) As-made 2D electronics was partially immersed in etchant solution (Nickel Etchant TFB, Transene Company Inc., Danvers, MA) for 3–4 h at 25°C to firstly release nickel layer under I/O region of electronics. Then,

electronics was transferred to DI water and dried in ethanol, while the released I/O region was unfolded on the substrate. (2) After electronics dried completely, the left nickel layer was etched in etchant solution for 1–2 h at 25 °C, after which electronics would be transferred to DI water and dried in ethanol to allow active device region to be unfolded on the substrate. Because the I/O pads covering larger region than electronics, these two-step etching process reduce the etching time for active device region. (3) After completely dried, electronics adhered weakly on the wafer, which can be easily removed from the substrate afterwards. Conductance (G_0) for each device was measured by a probe station (Desert Cryogenics, Model 4156C) with back plane grounded. Current–voltage (I – V) data were recorded using an Agilent semiconductor parameter analyzer (Model 4156C) with contacts to device through probe station. Device with conductance above 100 nS were accounted as initial devices with total number N_0 in this stage. (4) After conductance measurement, electronics on substrate was immersed in DI water for 4–6 h until it released from the substrate and fully suspended in the solution. (5) The electronics was transferred through glass pipette to PDL aqueous solution for surface modification as described above. (6) Electronics was loaded by glass pipette into syringe with gauge metal needle and injected through needle with different inner diameters (from 100 to 600 μm) into a chamber with I/O part unfolded near the chamber on a substrate. (7) Ethanol was used to rinse and dry the I/O part. (8) Conductance (G_1) for each device was measured again with the same probe station under same condition, and the total number of survived devices with G_1 above 100 nS was N_1 . Yield and conductance change were calculated as (N_1/N_0) and $(G_1 - G_0)/G_0$, respectively (Fig. 5.5).

5.2.7 Characterization

Surface-to-volume-ratio calculation: The surface-to-volume-ratio of a ribbon or a film (length, l ; width, w ; height, h) is calculated as $2(lw + lh + wh)/lwh = 2(1/h + 1/w + 1/l)$. For a typical thin film of 10 μm height, with much larger length and width, the surface-to-volume-ratio is ca. $2/h = 0.2 \mu\text{m}^{-1}$. For a typical ribbon (large length l) in our mesh structure with 5 and 0.7 μm in width and height respectively, the surface-to-volume-ratio is $\sim 2/h + 2/w = 3.25 \mu\text{m}^{-1}$.

Structure characterization: Scanning electron microscopy (SEM) was used to characterize the detail structure of electronics. Fluorescence images were obtained by doping the SU-8 resist solution with Rhodamine 6G at a concentration less than 1 $\mu\text{g}/\text{mL}$ before deposition and patterning. HMXST Micro-CT X-ray scanning system with a standard horizontal imaging axis cabinet was used to characterize the structure of mesh electronics in polymers. *ImageJ* (ver. 1.45i) and *VGStudio MAX* (ver. 2.0) were used for 3D reconstruction and analysis of confocal and micro-CT images.

Imaging of electronics in glass channel: Electronics with different width, and mesh structure were injected into the glass channels following the same injection

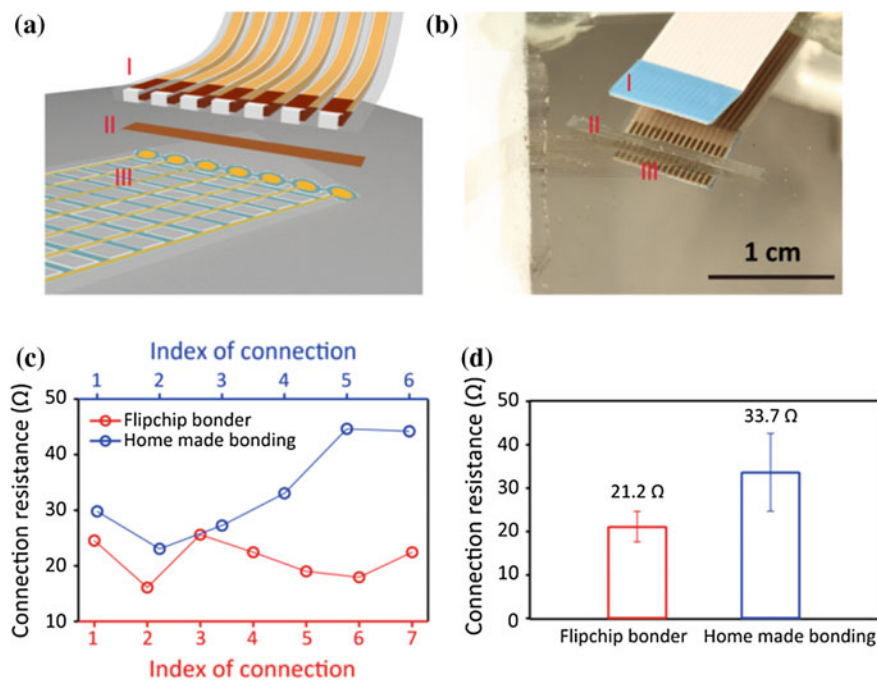


Fig. 5.5 Bonding process. Schematics (a) and corresponding optical image (b) of bonding. (I) flexible cable, (II) ACF film and (III) unfolded I/O region of device on substrate. **c** Connection resistance of ACF film bonded by flipchip bonder (red) and home-made bonding system (blue). **d** Statistic results of connection resistance data in (c), showing the average value and standard deviation

process described above. However, electronics was only partially injected through the needle. Confocal fluorescence microscope was used to image the 3D structure of the electronics in the glass needle. *Image J* was used to re-slice the 3D reconstructed images of device in the longitudinal direction by the step of $1\ \mu\text{m}$.

Immunostaining: Cells were fixed with 4% paraformaldehyde (Electron Microscope Sciences, Hatfield, PA) in PBS for 15–30 min, followed by 2–3 washes with ice-cold PBS. Cells were pre-blocked and permeabilized (0.2–0.25% Triton X-100 and 10% feral bovine serum (F2442, Sigma-Aldrich Corp. St. Louis, MO) for 1 h at room temperature. Next, the cells were incubated with primary antibodies Anti-neuron specific β -tubulin (in 1% FBS in 1% (v/v)) for 1 h at room temperature or overnight at $4\ ^\circ\text{C}$. Then cells were incubated with the secondary antibodies AlexaFluor-546 goat anti-mouse IgG (1:1000, Invitrogen, Grand Island, NY). For counter-staining of cell nuclei, cells were incubated with $0.1\text{--}1\ \mu\text{g}/\text{mL}$ Hoechst 34580 (Molecular Probes, Invitrogen, Grand Island, NY) for 1 min.

5.2.8 Chronic Damage Analysis

Brain slice preparation: (1) Mice underwent transcardial perfusion (40 mL PBS) and were fixed with 4% formaldehyde 4–5 weeks after the surgery [28]. (2) Mice were decapitated and brains were removed from the skull and set in 4% formaldehyde for 24 h as post fixation and then PBS for 24 h to remove extra formaldehyde. Electronics was kept inside the brain throughout fixing process. (3) Brains were blocked, separated into the two hemispheres and mounted on the stage of vibratome. 50–100 μm vibratome tissue slices (horizontal and coronal orientations) were prepared for samples with staining for microglia, astrocytes and nuclei. 30–50 μm vibratome tissue slices (horizontal and coronal orientations) were prepared for samples with staining for neurons. For samples with electronics injected in lateral ventricle, brains were blocked and then fixed in 1% (w/v) agarose type I-B to fix the position of electronics in the lateral ventricle cavity and then mounted on the stage of vibratome. 100 μm vibratome tissue horizontal slices were prepared. Coronal slices allowed for cuts in a direction along the long axis of the injected electronics and horizontal slices allowed for cuts in a direction perpendicular to the long axis of the injected device.

Chronic immunostaining for astrocytes and microglia: (1) Sections were then cleared with 5 mg/mL sodium borohydride in HEPES-buffered Hanks saline (HBHS) for 30 min, with 3 following washes with HBHS in 5–10 min intervals. Sodium azide (4%) was diluted 100x in HBHS in all steps using HBHS. (2) Slices were incubated with 0.5% (v/v) Triton X-100 in HBHS for 30 min at room temperature. (3) Slices were blocked with 5% (w/v) FBS and incubated overnight at room temperature. (4) Slices were washed four times in 30 min intervals with HBHS to clear any remaining serum in the tissue. Slices were then incubated overnight at room temperature with the GFAP primary antibody and rabbit anti-Iba-1 primary antibody containing 0.2% triton and 3% serum. (5) After incubation period, slices were again washed four times for 30 min with HBHS, slices were incubated with secondary antibody Alexa Flour 546 goat anti-rat and secondary antibody Alexa Fluor 488 goat anti-rabbit, Hoechst 33342, 0.2% Triton and 3% serum overnight. (6) After the final washes (four for 30 min each HBHS), Slices were mounted on glass slides with coverslips using Prolong Gold mounting media. The slides remained covered (protected from light) at room temperature, allowing for 12 h of clearance before imaging.

Chronic immunostaining for neuron: Slices were cleared with 5 mg/mL sodium borohydride in HBHS for 30 min, with 3 following washes with HBHS in 5–10 min intervals. Then, slices were incubated with 0.5% (v/v) Triton X-100 in HBHS for 30 min at room temperature. Next, sections were blocked with 5% (w/v) serum and incubated overnight at room temperature. Next, slices were washed four times in 30-minute intervals with HBHS to clear any remaining serum in the tissue. Slices were then incubated with primary antibody NeuN in 0.3% Triton-X100 and 3% serum in PBS overnight at room temperature. After 24 h, sections were washed four times for 30 min in PBS and then counterstained with Hoechst 33342. Prolong

gold coverslips were used again to protect from light and allowed for 12 h of clearance before imaging. When the antibody solutions were first prepared, they included 0.3 Triton X-100 and 5% normal goat serum.

Chronic immunostaining for lateral ventricle: Slices were cleared with 5 mg/mL sodium borohydride in HBHS for 30 min, with 3 following washes with HBHS in 5–10 min intervals. Then, slices were incubated with 0.5% (v/v) Triton X-100 in HBHS for 30 min at room temperature. Next, sections were blocked with 5% (w/v) serum and incubated overnight at room temperature. Next, slices were washed four times in 30-minute intervals with HBHS to clear any remaining serum in the tissue. Slices were then incubated with primary antibody NeuN in 0.3% Triton-X100 and 3% serum in PBS overnight at room temperature. After 24 h, sections were washed four times for 30 min in PBS and then counterstained with Hoechst 33342. Prolong gold coverslips were used again to protect from light and allowed for 12 h of clearance before imaging. When the antibody solutions were first prepared, they included 0.3 Triton X-100 and 5% serum.

5.3 Results and Discussion

5.3.1 Syringe-Injectable Electronics

Figure 5.6 shows the schematics of the basic idea. We design and encapsulate electronic components in a mesh network made by photopatternable epoxy (SU-8). This mesh network are fabricated on a nickel sacrificial layer as reported previously [14], and then completely removed from the substrate. All the electronic sensor

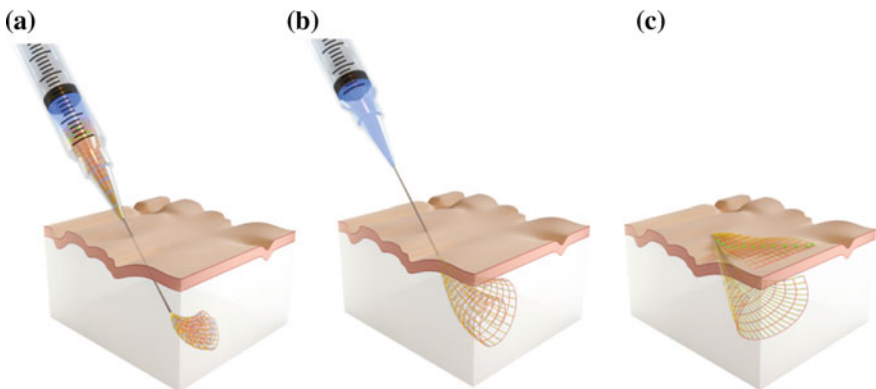


Fig. 5.6 Syringe-injectable electronics. **a** Mesh electronics is loaded into syringe and injected into targeted system. **b** Mesh electronics is injected into targeted system and gradually unfold. **c** Mesh electronics has been injected into targeted system and totally unfold with I/O region injected outside for bonding. Blue and green dots: nanodevice and (Continued) I/O pads; yellow: metal line encapsulated in polymer; red: supporting polymer; blue: solution

units, metal interconnects and input/output (I/O) pads distribute in this freestanding network (Fig. 5.1). We can load mesh electronics into a syringe and then inject through a needle (Fig. 5.6a) with mesh unfold to restore its original geometry (Fig. 5.6b, c). By precisely controlling the injection process, we can withdraw the needle during injection to unfold mesh inside the targeted system and eject the I/O region on the outside of the targeted system for the further electrical bonding and connection to individually address electrical components delivered into the targeted system.

In our design, the width of ribbons in the network is typically 5–40 μm , the total thickness is less than 800 nm and the size of unit cells is several hundred micrometers. Figure 5.7a shows a 3D reconstructed confocal fluorescence image of a representative injection. 2-mm-wide mesh electronics was injected through a glass needle with 95- μm inner diameters into PBS solution. This electronics has ribbons with feature size of 5 μm and thickness of 700–800 nm. We modify the mesh electronics by poly-D-lysine (0.5–1.0 mg/mL, MW 70,000–150,000) to get a hydrophilic surface to allow it to be suspended and unfolded in aqueous solution. The stepwise process of a representative injection into a free solution is shown in Fig. 5.7b. Mesh electronics was loaded into a glass tube (with 95 μm tip) as described in experimental section. Glass needle was then detached from the syringe and mounted onto a commercially available patch-clamp system. Microinjector is connected to the glass needle to apply sufficient pressure (1 bar, 1–10 ms) for injection.

Using microinjector, we can inject mesh electronics out gradually from needle with injection rate at 5–10 μm of mesh electronics per injection. we can control

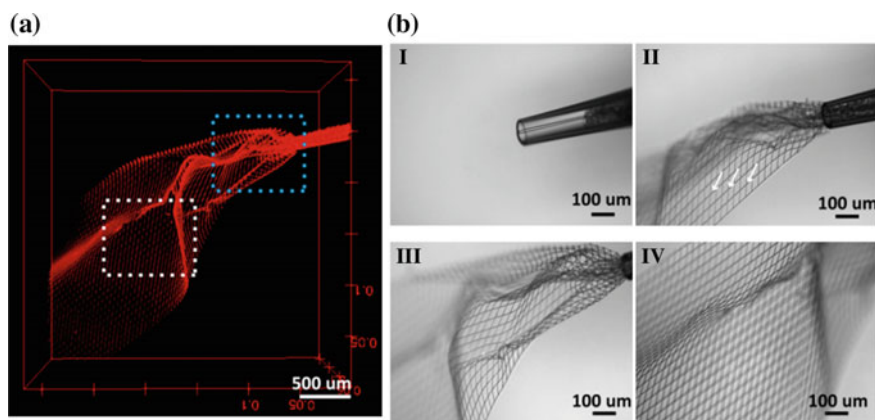


Fig. 5.7 Stepwise injection. **a** 3D reconstructed fluorescence image shows the electronics are injected out from needle (blue dashed box) and subsequently self-unfolded in the solution. **b** Images show that electronics are stepwise injected into solution by glass needle with diameter of 90 μm . Electronics was pushed to the tip of needle (I), electronics was partially injected out (II), 50% area of whole electronics was injected out, with partially unfolded mesh structure near needle region (III) corresponding to the region highlighted by blue dashed box in (c), and completely unfolded mesh structure (IV) corresponding to the region highlighted by white dashed box in (a)

injected solution less than 100 nL in each injection to minimize the invasiveness (Fig. 5.8). Injected mesh electronics can gradually unfold in the aqueous solution due to the reduction of surface energy and release of the internal strain. This precisely controlled injection process allows us to inject mesh electronics with sensors into the targeted system while eject the metal interconnects and I/O region on the outside. We further use the anisotropic conductive film (ACF) to bond the I/O pads of mesh electronics with external recording set-ups (Fig. 5.4).

We evaluate the correlation between the yields of device after injection to the inner diameter (ID) of needle by using standard metal gauge needles (Fig. 5.9). The average yield of mesh electronics containing semiconductor nanowires ranges from 98% (600 μm , ID) to 83% (100 μm , ID) with less than 12% conductance change in average. The average yield of injection for metal electrode ranges from 90%

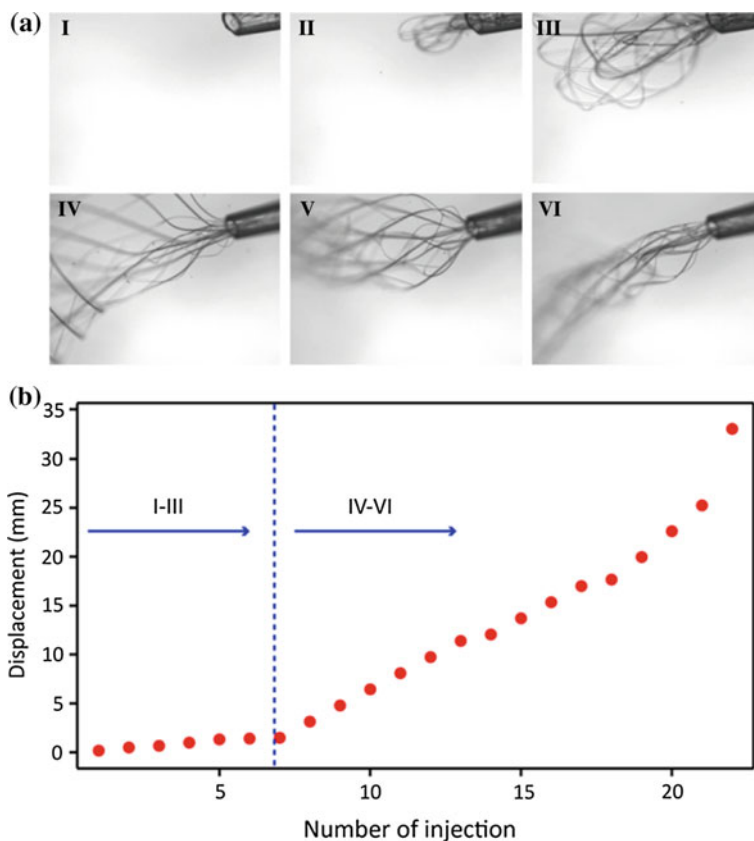


Fig. 5.8 Control of injection process. **a** Optical images of a typical device during injection process. (I–VI) The device is gradually injected into free solution by micro-injector with 1 bar pressure, 10 ms pulse (before blue dashed line in **b** and 50 ms pulse (after blue dashed line in **b**)) injection time for each step. **b** The injected length of device versus number of injection. Blue arrow (I–III) corresponding to images (I–III) in **(a)**. Blue arrow (IV–VI) corresponding to images (IV–VI) in **(a)**

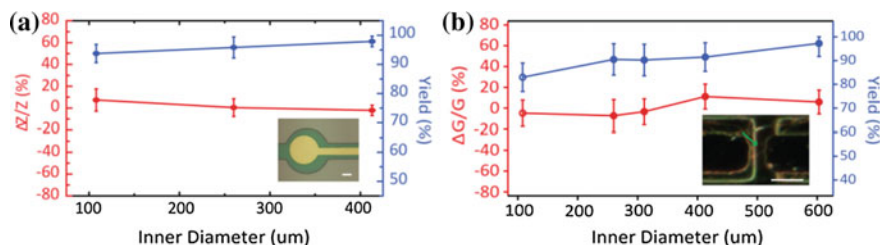


Fig. 5.9 Yield of injection. **a** Yield (blue) and impedance change (red) of electronics containing metal electrode injected through different gauge needles inset: bright field image of metal electrode on mesh electronics. **b** Yield (blue) and conductance change (red) of electronics containing nanowire field-effect transistor injected through different gauge needles. Solid spot: 5 mm wide mesh, hollow spot: 2 mm wide mesh. Inset: bright field image of nanowire FET (highlighted by green arrows) on mesh electronics. Scale bar: 10 μm

(100 μm , ID) to 98% (400 μm , ID) with less than 10% impedance change in average. Altogether, results show robustness of mesh electronics for syringe-injection through a wide range of needle ID.

5.3.2 Parameters for Syringe Injectable Electronics

We believe this submicron thickness and mesh network design for electronics are very critical to the success of injection. First, this design increases the surface-to-volume ratio of electronics from $0.2 \mu\text{m}^{-1}$ (thin film electronics with 10- μm thickness) to $3.25 \mu\text{m}^{-1}$ (mesh electronics with 5- μm -wide and 800-nm-thick ribbon). Second, combining with the polyelectrolyte surface modifications, this design reduces the effective density of electronics (due to the forming of electric double layers) allowing electronics to be unfold and floating in solution. Third, this design increases the drag force from solution motion to mesh electronics enabling effective injection. Finally, the mesh design reduce the effective bending stiffness of electronics from 0.0602 nN m (thin film electronics) to 0.0025 nN m (mesh electronics) so that electronics can be readily folded to pass through fine needles.

To further understand the structure design parameters for injection, we carried out imaging experiments using confocal fluorescence imaging to 3D reconstruct the structure of injectable electronics inside a glass needle. Glass tube was pulled into a fluidic channel (Fig. 5.10a), with the same geometry and inner diameter as the metal and glass needle used for applications. The channel inner diameter is 200–600 μm measured by confocal fluorescence imaging and the length is 0.1–0.5 mm. We injected mesh electronics with different structures into channel. SU-8 in mesh electronics was doped by Rhodamine-6G for imaging and 3D reconstruction.

We call the ribbons along the injection direction as longitudinal ribbons and the ribbons perpendicular to the injection direction as transverse ribbons. Longitudinal and transverse ribbons together form mesh with a periodic unit cells structure. All the

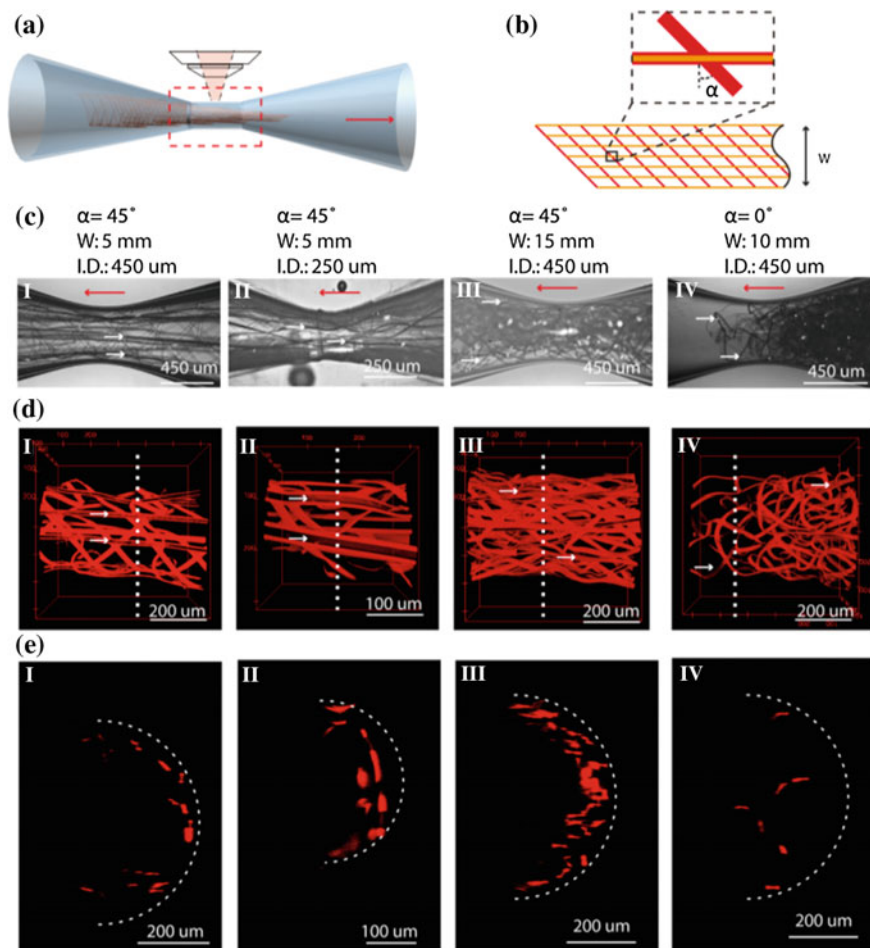


Fig. 5.10 Parameters for injection. **a** Schematic shows the structure of the pulled glass tube for testing and imaging the structure of different electronics design in the needle. Red arrow indicates the direction of injection. **b** Schematics of design for injection. The dashed black circles highlight the detailed structure where red represents supporting and passivation polymer and yellow represents metal lines. **c** Optical images of different electronics design injected through glass needle. (I–II) 5 mm wide meshes as design in **(b, I)** were injected through 450 and 250 μm ID glass needle; (III) 15 mm wide mesh as design in **(b, I)** was injected through 450 μm ID needle. (V) 10 mm mesh as design in **(b, II)** was injected through 450 μm ID needle. **d** Top view of 3D reconstructed confocal images corresponding to **(c)**. White arrows in **(c and d)** highlight metal contacts in the mesh. **e** Images at cross-sections as indicated by white dashed lines in **(c)**. White dashed curves in **e** highlight the cross-section of needle boundary

unit cells are identical in our design. Metal interconnects and sensors are mainly encapsulated in longitudinal ribbons (Fig. 5.10b). The ribbons in imaging experiments are 20- μm -wide and 700-nm-thick for SU-8 and 10- μm -wide and 100-nm-thick for metal. Different width of mesh was used for investigating the

limitations since wider electronics can cover a larger sensing area. All meshes have sharp tip of 45° to be easily loaded into syringes (Fig. 5.10b). Two meshes with different unit cell geometries have been used here to investigate the injection. In design #1, the transverse ribbons are tilted 45° counterclockwise in transverse direction on the mesh plane forming $\alpha = 45^\circ$ to longitudinal ribbons. In design #2, the transverse ribbons are perpendicular to the longitudinal ribbons to form $\alpha = 0^\circ$ to longitudinal ribbons. Figure 5.10c–e show optical micrographs, 3D-reconstructed and cross-section images of assembled structures for each mesh in glass channels.

Firstly, 5-mm-wide mesh with $\alpha = 45^\circ$ design structure can be smoothly injected through a channel with ca. 500- μm -inner-diameter (Fig. 5.10c, I). The 3D-reconstructed image shows that the mesh rolls into a tubular structure inside the channel keeping longitudinal ribbons straight and transverse ribbons bended (Fig. 5.10d, I). The cross-section image of 3D reconstruction further confirms this tubular structure, illustrating that all of the ribbons are closely and uniformly packed to the inner surface of glass channel. The other half of mesh in the bottom part of the needle is blocked from imaging by the dense ribbons on the top part of channel. Secondly, we found that reduction of channel's ID did not affect the assembled structure of mesh in the needle. The same mesh can be injected smoothly in through 200- μm ID channel (Fig. 5.10c, II). 3D-reconstructed and cross-section images further demonstrate the tubular structure of mesh in the needle and closed packed ribbons to the inner surface of channel (Fig. 5.10d, II, e, II). Thirdly, increasing the width of mesh can also allow the mesh to be smoothly injected through channels. As a representative example, 15-mm-wide mesh can be injected through the channel with an ID of ca. 500 μm (Fig. 5.10c, III). The width-to-ID ratio is ca. 30. The 3D-reconstructed and cross-section images (Fig. 5.10d, III, e, III) also show a tubular structure of mesh in the channel and closed packed ribbons to the inner wall of channel. We found that the longitudinal ribbons can remain straight during injection even further increase the numbers and densities of ribbons. Fourthly, as a control sample, we found that the mesh with $\alpha = 0^\circ$ design could not pass through the channel with 500- μm ID and easily forms a jammed structure (Fig. 5.10c, IV). 3D-reconstructed and cross-section imaging further shows the ribbons entangled together and block the channel (Fig. 5.10d, IV, e, IV). Together, these results highlight the point that longitudinal ribbons need to keep straight during injection to avoid a high-strain deformation that could damage devices and buckles that could dramatically decrease the stiffness of the structure in the longitudinal direction [29], and therefore, collapse longitudinal ribbons rather than bend transverse ribbons causing large strain to damage device and block the needle for the further injection.

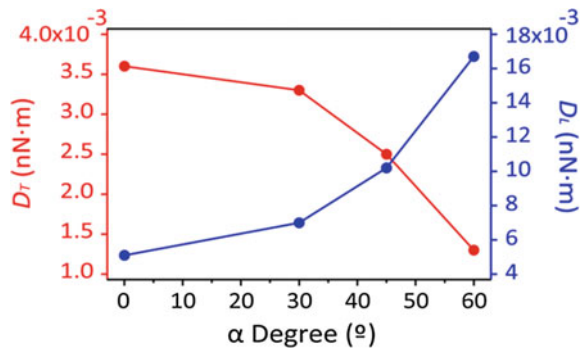
To quantitatively explain these experimental results, we define the bending stiffness for mesh bent in longitudinal direction and transverse direction of injection as D_L and D_T respectively. Firstly, the $\alpha = 0^\circ$ design leads to a non-uniform distribution of effective bending stiffness D_L . Considering the effective bending stiffness D_L of different cross-sections, when the cross-section goes through the transverse ribbons, the bending stiffness is high (0.0602 nN m), while when the cross-section does not go through the transverse ribbons, the bending stiffness is

very low (0.0025 nN m). This dramatic bending stiffness change facilitates stress localization leading to the buckling of longitudinal ribbons. On the contrary, $\alpha = 45^\circ$ design creates a uniform distribution of effective bending stiffness D_L , therefore, the electronics can bend homogeneously. Secondly, this $\alpha = 45^\circ$ design decreases D_T and increase D_L so that the mesh is more readily to bend and roll-up into tubular structure going through the needle and less readily buckle in the longitudinal direction.

We conducted finite element modeling (FEM) analysis to simulate the bending stiffness for mesh bending in two directions. Notably, reducing the D_T and increases D_L is benefit to the injection process. Figure 5.1 is the schematic showing how to select unit cells from the periodic mesh structure for simulation. The relation of angle α to bending stiffness was investigated. The white dashed lines indicate the boundary for unit cells from mesh for simulation. We define effective bending stiffness of mesh as the stiffness required a homogenous beam to achieve the same bending under the same moment. Therefore, every unit cell has the same bending stiffness and we use a unit cell to calculate the effective bending stiffness of the structure from the simulations. The results (Fig. 5.11) show that increasing α from 0° to 60° , D_T decreases from 0.0036 to 0.0013 nN m and D_L increases from 0.0051 to 0.0167 nN m. The bending stiffness ratio between bending in transverse and longitudinal direction increases for 8.7 times (1.46–12.8). Altogether, those results show that increasing the α can significantly facilitate the rolling of electronics in the needle in transverse direction to form a tubular structure and prevent bending in the longitudinal direction.

We use simulations to further estimate the strain distribution in the electronics during injections in needles with different sizes. We only simulate the bending of a unit cell to the curvature of the needle, since every unit cell behaves similarly. The inset of Fig. 5.5b shows a bending structure of a representative unit cell inside a 200- μm diameter needle. The color mode shows the contour plot of the maximal principle strain. The maximal value is reached on the junction between the transverse and longitudinal ribbons. Simulation results (Fig. 5.5b) show the dependence of the maximal principal strain of the unit cell on the curvature of the needles $1/r$, and a linear relation can fit the dependence. The two colors correspond to two different sizes of the mesh structures used for needle inner diameter larger or

Fig. 5.11 Mechanical analysis for injection process. Bending stiffness in longitudinal and transverse direction of the mesh with change of ribbons angle in Fig. 5.1



smaller than 200 μm . the two corresponding fitting relation are $0.499/r$ and $0.473/r$. For the needle diameter around 100 μm , the maximal principle strain can be extrapolated as 0.998 and 0.946% respectively, which are both smaller than the critical breaking strain of SU-8 for bulk materials. The stress intensity factor K for a thin film under pure bending has the following scaling relation [30] $K \sim E\varepsilon\sqrt{h}$, where E is the Young's modulus of the material, and h is the thickness of ribbon. The ribbon breaks when K reaches the toughness of the material K_c . K_c is usually on the order of $100 \text{ KPa}\sqrt{\text{m}}$, [31] and E for SU-8 is around 1 GPa. Therefore, for a device with thickness several hundred nanometers, the fracture strain ε_c is on the order of several percent. In fact, with our current structure, experiment demonstrates that SU-8 ribbon can sustain the bending with curvature larger than $0.1 \mu\text{m}^{-1}$ that corresponds to the curvature of 20- μm ID needle.

Last, we tested the injection by using thin film electronics with same thickness (Fig. 5.12a). For ca. 400- μm inner diameter needle, only 1.5 mm thin film electronics can go through (Fig. 5.12b). These results further demonstrate the unique design of the mesh electronics for injection.

5.3.3 Syringe-Injectable Electronics for Soft Matters

Mesh electronics can be co-injected with various materials into cavities with a small injection site and unfold to distribute sensors (Fig. 5.6c). We mixed 15-mm-wide electronics containing nanowire strain sensors with PDMS monomer diluted in hexane. We injected this mixture through a 20-gauge (603 μm , ID) needle into a cavity constituted by two pieces of cured PDMS (Fig. 5.13a), and ejected interconnects and I/O pads outside for bonding. Mesh electronics inside the cavity can gradually unfold and cover the 15 mm \times 20 mm area (Fig. 5.13b, c). Micro-CT 3D reconstructed imaging of mesh electronics shows that, due to the flexibility, mesh electronics can cover the 3D step-like structures inside the cavity (Fig. 5.13c, II). The conductance changes from 11 silicon nanowire devices on the mesh electronics can be recorded as strain sensors. We monitored the response of nanowire device when a point load in z-direction has been introduced to PDMS to create a non-uniform strain distribution (Fig. 5.13d). The conductance changes from nanowire device are consistent with strain distribution and our previous report [14]. This result proves that injected electronics can be delivered into soft system with small damage and used to measure strain distribution inside soft materials to the external mechanical deformation.

We further extended this co-injection concept through the co-injection of mesh electronics with embryonic neural cells into tissue scaffold (Fig. 5.14). Embryonic rat hippocampal neurons were mixed with mesh electronics and uncured MatrigelTM. We inject the composite into cured MatrigelTM (Fig. 5.14a). 3D-reconstructed confocal micrographs from two-week culture showed that neurons with high-density outgrowth neurites interpenetrating in the mesh structure of

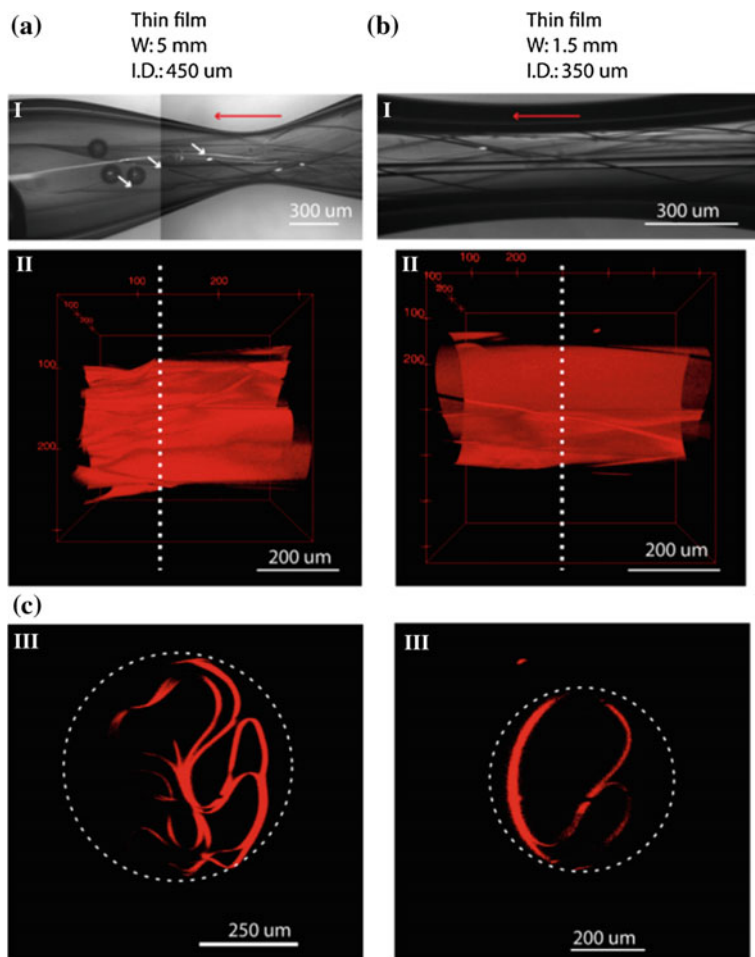


Fig. 5.12 Control experiments of thin film electronics in needle. **a** (I, II), Optical image shows 5-mm-wide thin film electronics was injected through 400- μ m inner diameter glass needle (I), and 1.5-mm-wide thin film electronics was injected through 350- μ m inner diameter glass needle (II). Red arrow indicates the direction of injection. White arrows in (I) indicate the end of metal line to show the thin film cannot totally go through the needle. **b** (I, II), Top view of 3D reconstructed confocal images correspond to dashed box in (a). **c** (I, II), Images at cross-section as indicated by white dashed line in (b). White dashed circle in (c) highlights the needle boundary

electronics, proving the biocompatibility of the electronics. It is noticeable that the width of ribbons was similar to the neurite projections, exhibiting seamless integration between them (Fig. 5.14b).

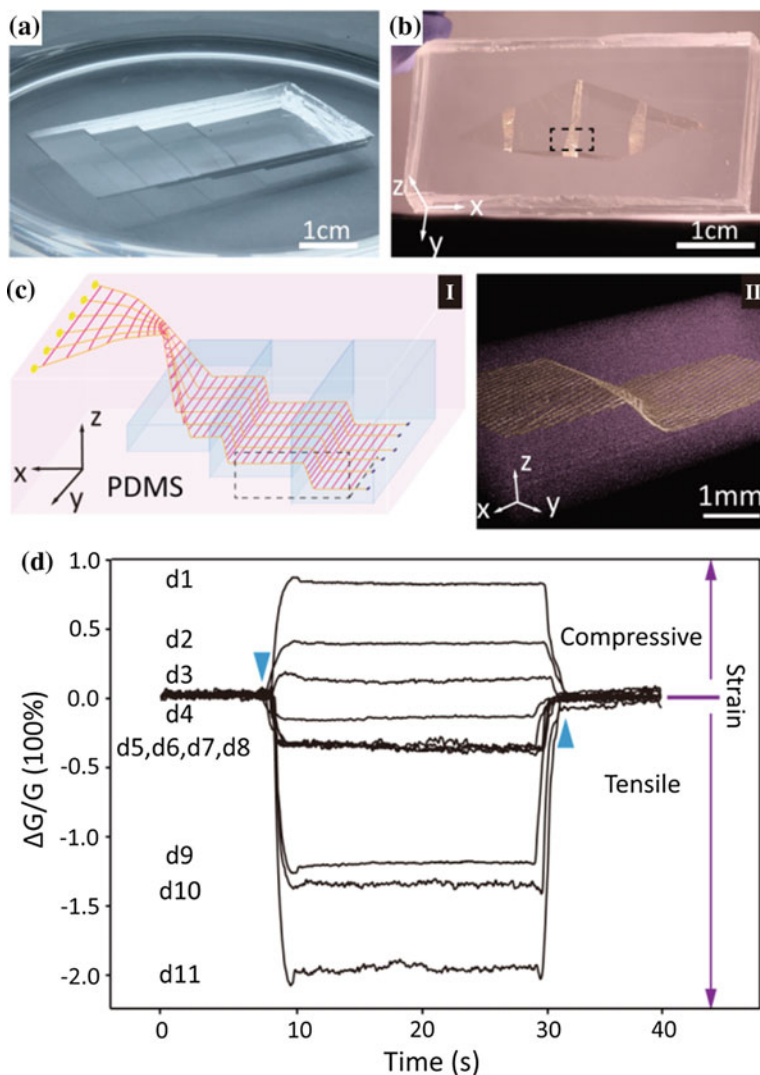


Fig. 5.13 Injectable electronics for soft mater. **a**, **b**, Optical images of PDMS cavity before injection (**a**) and the hybrid structure of injectable devices embedded in PDMS after injection (**b**). **c** Schematic of electronics injected and cured in cavity of PDMS with I/O pads unfolded outside the cavity (**I**). Red, SU8; Yellow, metal/SU8; Blue, nanodevices. Micro-CT image (**II**) shows the zoomed-in structure highlighted by the black dashed box in (**b**) and (**c**, **I**). Pseudocolors are applied: Yellow, metal; Purple, PDMS. **d** 11 nanowire devices response to point loading on the PDMS. The downward and upward pointing triangles denote the times when the strain was applied and released, respectively. The upward and downward arrows show the compressive and tensile strains, corresponding to the plus and minus change of conductance respectively

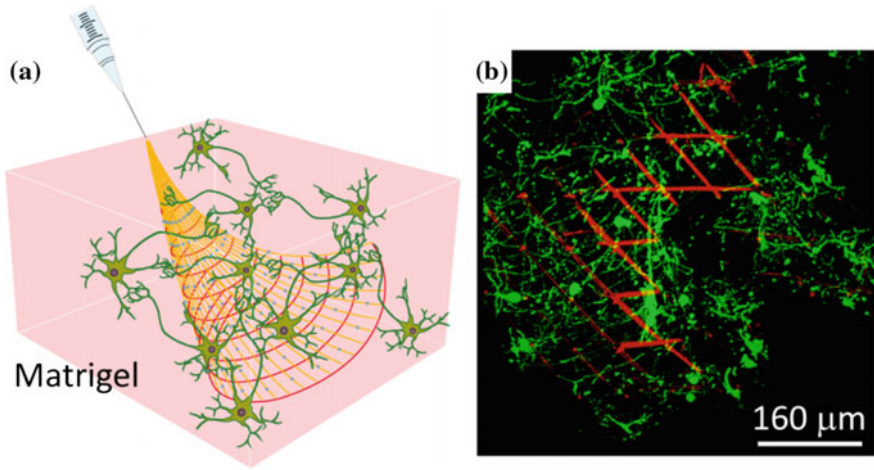


Fig. 5.14 Inject electronics for tissue engineering. **a** schematic of injection of electronics with neuron cells into Matrigel. Red, SU8; Yellow, metal/SU8; Blue, nanodevices; Green, neuron cells. **b** Confocal fluorescence images of 100 μm projection show the interpenetration between neurons and ribbons of injectable electronics after co-injected into matrigel for 14 days. Red: reflective image of mesh and green: beta-tubulin staining for neurons

5.3.4 Syringe-Injectable Electronics for Behaving Rodent Brains

Based on our simulation, D_L of mesh electronics that can be injected is ca. 0.01 nNm, which is similar to the bending stiffness of tissue. In addition, the bending energy of mesh electronics matches the surface membrane energy [32] of single cells and 1 million times less than the bending stiffness of the conventional silicon probe and carbon fibers [24, 27]. In addition, our previous studies [8] have demonstrated that the design of these macroporous structures has allowed the growth of tissue within interior spaces. Together, we consider syringe-injectable electronics as a great candidate for in vivo chronic implants, especially for the soft tissues such as brain.

We conducted the in vivo chronic implantation experiments by stereotactically injecting mesh electronics into behaving rodent brain tissue with a 0.5-mm diameter drilled hole from craniotomy. The injection follows steps illustrated in Fig. 5.15a, b. Specifically, 2-mm-wide electronics was injected into the tissue-dense hippocampus region of the mice (Fig. 5.15c, I) through a ca. 200- μm inner diameter glass needle controlled by microinjector. This process only introduced trace amount of solution ($<1 \mu\text{L}$) into the brain showing vanishingly-small invasiveness. Fluorescence imaging of coronal brain slice shows unfolding of mesh electronics after 5 weeks in hippocampus region with little interruption to the layered structure of neurons (Fig. 5.15d, e). Immunostaining imaging further shows no proliferation

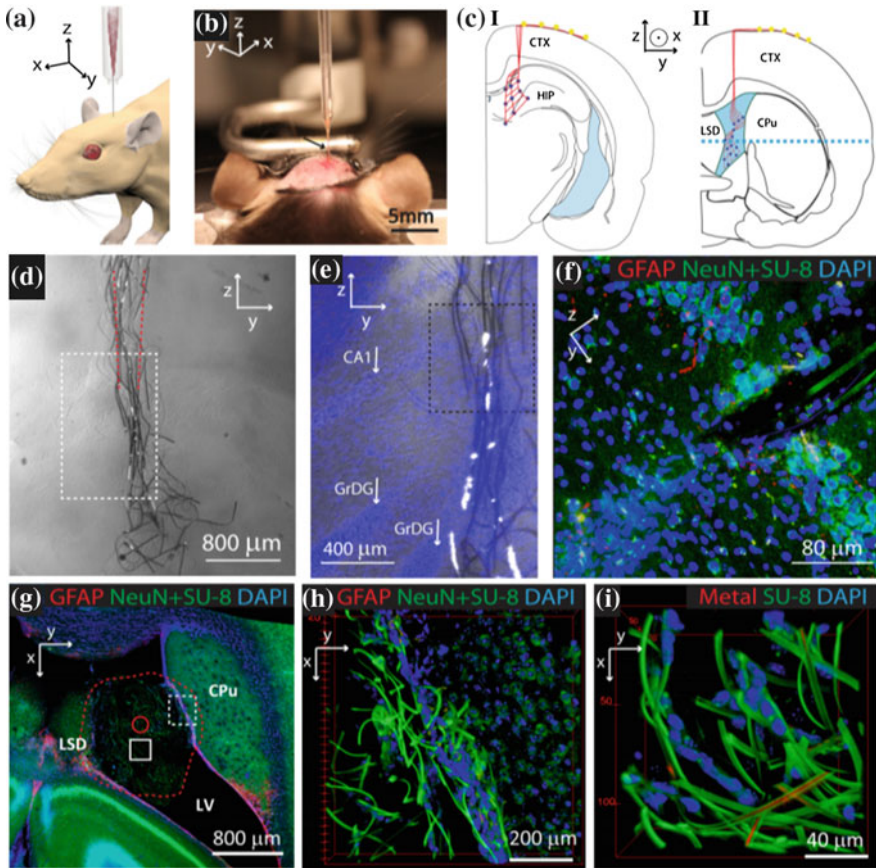


Fig. 5.15 Injectable electronics for brain implants. **a** Schematic shows stereotactic injection of injectable electronics into in vivo system. **b** Optical image shows the stereotactic injection of injectable electronics into mice brain tissue. **c** Schematics of coronal slices show that injectable electronics are injected into cerebral cortex (CTX) and hippocampus (HIP) region of brain (I), and the cavity of Lateral Ventricle (LV) beside caudoputamen region (CPu) and lateral septal nucleus (LSD) with unfolding (II). Red: mesh structure of injectable electronics, blue: nanodevices or metal electrodes on injectable electronics and yellow: I/O pads for electrical connections. Blue dashed lines indicate direction of horizontal slicing for imaging. **d** Bright-field image of coronal slice in (c, I) shows the electronics was injected into the cortex and hippocampus region. Red dashed lines indicate the boundary of glass needle. **e** Overlaid bright field and epi-fluorescence image of white dashed box highlighted region in (d). Blue: DAPI. White arrows indicate the different layers of cells in hippocampus. GrDG: granular layer dentate gyrus and CA3: field CA3 of hippocampus. **f** Projection of 30 μm thick volume from the zoomed-in region by black dashed box in (e) shows neural cells interface with electronics. **g** Projection of 100 μm thick volume for the electronics injected into LV inside brain at the position indicated by blue dashed line in (c, II). Red dashed line highlights the boundary of unfolded mesh inside LV. Red circle indicates the size of the needle for injection. **h** 3D render of the zoomed-in region highlighted by white dashed box in (g) shows the interface between nanoelectronics and subventricular zone. **i** 3D render of the zoomed-in region highlighted by white box in (g)

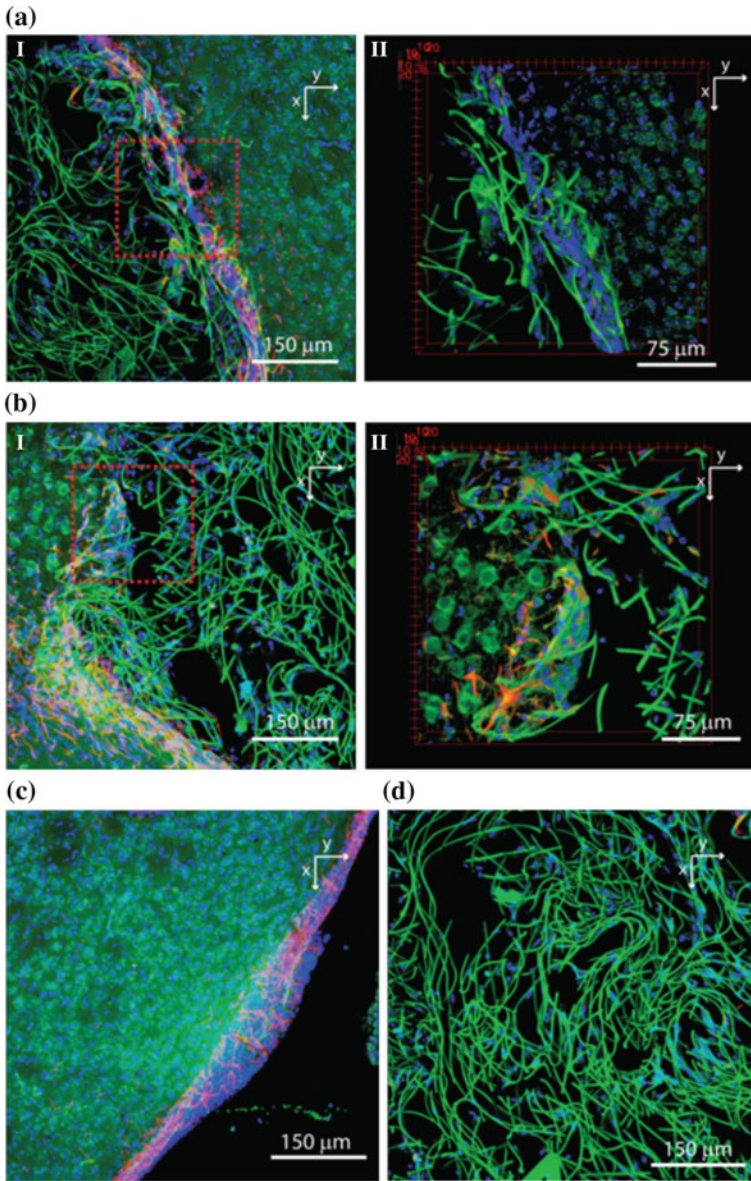


Fig. 5.16 Interface between electronics and in vivo regenerative neural tissue. **a** Projection of 30 μm thick volume of slice shows the interface between electronics in in vivo with subventricular zone (I) and 3D render of red dashed box highlighted zoomed-in region (II). **b** Projection of 30 μm thick volume of slice shows the interface between electronics in in vivo with stria (I) and 3D render of red dashed box highlights zoomed-in region (II). Blue: DAPI, green: SU-8 and NeuN and red: GFAP. **c** Control sample shows subventricular zone without device. **d** Projection of 80 μm thick volume for the region highlighted by white box in Fig. 5.15g. Blue: DAPI, green: SU-8 ribbon and neurons and red: GFAP

of astrocytes around the electronics and a tight junction between neurons and unfolded mesh electronics (Fig. 5.15f).

To further demonstrate the potential of the geometrical restoration of the injectable electronics in cavity as well as its uniqueness for potential applications in cellular therapy, we injected mesh electronics into the cavity of lateral ventricle region in rat brain to target the subventricular zone region, considering progenitor cells in this region have proved capability for regeneration and long-distance migration [33], which shows potential for neuron replacement therapy [34, 35]. Mesh electronics was stereotaxically injected into the lateral ventricle region through a 200- μm glass needle (Fig. 5.15c, II). Mesh electronics in solution is similar to synthetic polymeric networks. A large volume of mesh electronics can be continuously injected into the cavity of lateral ventricle to fulfill the cavity and contact cell walls after unfolding. After 5 weeks, immunostaining of horizontal slice showed unfolded mesh electronics occupied a volume with 1.5-mm diameter, which covers the most inner area of lateral ventricle and bridges the lateral walls. Immunostaining with higher magnification shows that ribbons from mesh electronics contacted with the caudoputamen have interpenetrated with cells and merged into the astrocytic-characteristic tube-like structure (Fig. 5.15g–i) [33]. Control experiment from the same rodent shows the same level of glial fibrillary acidic protein (GFAP) expression, which demonstrates no chronic tissue response to the electronics. Importantly, image shows a migration of neural outgrowth cells from both sides of the lateral ventricle cell walls into the interior space of the unfolded mesh, even in the center of cavity. Those cells formed tight junctions on the ribbons of electronics in chain-structures and migrated along the direction of ribbons from mesh electronics (Fig. 5.16). Considering the electrophysiological monitoring capability, these results show a potential application to use injectable electronics to direct, mobilize and monitor the adult stem neurons from lateral ventricle region to injured brain region for therapy.

5.4 Conclusion

The methods and mechanical designs introduced here represent new concepts for electronics fabrication and delivery. The future potential development is to (1) increase the complexity of electronics while keeping its nanoscale-thickness to maintain the syringe injectable property, (2) investigate different materials as supporting materials for injectable electronics to achieve the subsequent dissolving of materials releasing the sensing unit inside the injected subject to allow those unit to behave like colloidal in the subject for better integration, (3) further develop a non-surgical implantation bioelectronics and (4) create cellular therapy by using injectable electronics as scaffold for stem cell delivery, mobilization and monitoring.

Bibliography

1. Reuss RH, Hopper DG, Park J (2006) *Macroelectronics*. MRS Bull 31:447
2. Thakor NV (2013) Translating the brain-machine interface. *Sci Transl Med* 5:210ps17
3. Kim DH et al (2008) Stretchable and foldable silicon integrated circuits. *Science* 320:507
4. Kaltenbrunner M et al (2013) An ultra-lightweight design for imperceptible plastic electronics. *Nature* 499:458
5. Timko BP et al (2009) Electrical recording from hearts with flexible nanowire device arrays. *Nano Lett* 9:914
6. Cherenack K, van Pieterse L (2012) Smart textiles: challenges and opportunities. *J Appl Phys* 112:091301
7. Kim DH et al (2011) Epidermal electronics. *Science* 333:838
8. Tian B et al (2012) Self-adjusted synthesis of ordered stable mesoporous minerals by acid-base pairs. *Nature Mater.* 11:986
9. Rousche PJ et al (2001) Flexible polyimide-based intracortical electrode arrays with bioactive capability. *IEEE Trans Biomed Eng* 48:361
10. Kim T et al (2013) Injectable, cellular-scale optoelectronics with applications for wireless optogenetics. *Science* 340:211
11. Troyk PP (1999) Injectable electronic identification, monitoring, and stimulation systems. *Annu Rev Biomed Eng* 1:177
12. Liu J et al (2013) Multifunctional three-dimensional macroporous nanoelectronic networks for smart materials. *Proc Natl Acad Sci USA* 110:6694
13. Alivisatos PA et al (2013) Nanotools for neuroscience and brain activity mapping. *ACS Nano* 7:1850
14. Deisseroth K, Schnitzer MJ (2013) Engineering approaches to illuminating brain structure and dynamics. *Neuron* 80:568
15. Bencherif SA et al (2012) Injectable preformed scaffolds with shape-memory properties. *Proc Natl Acad Sci USA* 109:19590
16. Hillel AT et al (2011) Photoactivated composite biomaterial for soft tissue restoration in rodents and in humans. *Sci Transl Med* 3:93ra67
17. Bible E et al (2009) Attachment of stem cells to scaffold particles for intra-cerebral transplantation. *Nature Protoc.* 4:1440
18. Davidson BL, Breakefield XO (2003) Viral vectors for gene delivery to the nervous system. *Nat Rev Neurosci* 4:353
19. Cui Y, Wei Q, Park H, Lieber CM (2001) Nanowire nanosensors for highly sensitive and selective detection of biological and chemical species. *Science* 293:1289
20. Lieber CM, Wang ZL (2007) Functional nanowires. *MRS Bull* 32:99
21. Du J, Roukes ML, Masmanidis SC (2009) Dual-side and three-dimensional microelectrode arrays fabricated from ultra-thin silicon substrates. *J Micromech Microeng* 19:075008
22. Patolsky F, Zheng G, Lieber CM (2006) Fabrication of silicon nanowire devices for ultrasensitive, label-free, real-time detection of biological and chemical species. *Nat Protoc* 1:1711
23. Qing Q et al (2014) Free-standing kinked nanowire transistor probes for targeted intracellular recording in three dimensions. *Nat Nanotechnol* 9:142
24. Lee H, Bellamkonda RV, Sun W, Levenston ME (2005) Biomechanical analysis of silicon microelectrode-induced strain in the brain. *J Neural Eng* 2:81
25. Steif PS (2012) *Mechanics of materials*. Pearson, London
26. Dai J, Sheetz MP, Wan X, Morris CE (1998) Membrane tension in swelling and shrinking molluscan neurons. *J Neurosci* 18:6681
27. Yoshida Kozai TD et al (2013) Ultrasmall implantable composite microelectrodes with bioactive surfaces for chronic neural interfaces. *Nat Mater* 11:1065
28. Seri B et al (2001) Astrocytes give rise to new neurons in the adult mammalian hippocampus. *J Neurosci* 21:7153

29. Koiter WT (2008) Elastic stability of solids and structures. Cambridge University Press, Cambridge
30. Tada H, Paris PC, Irwin GR (2000) Stress analysis of cracks handbook. ASME Press, New York
31. Selby K, Miller LE (1975) Fracture toughness and mechanical behaviour of an epoxy resin. *J Mater Sci* 10:12
32. Sen S, Subramanian S, Discher DE (2005) Indentation and adhesive probing of a cell membrane with AFM: theoretical model and experiments. *Biophys J* 89:3203
33. Alvarez-Buylla A, Garcia-Verdugo JM (2002) Neurogenesis in adult subventricular zone. *J Neurosci* 22:629
34. Cuitis MA, Faull RLM, Eriksson PS (2007) The effect of neurodegenerative diseases on the subventricular zone. *Nat Rev Neurosci* 8:712
35. Goldman S (2005) Stem and progenitor cell-based therapy of the human central nervous system. *Nat Biotechnol* 23:862

Chapter 6

Outlook

In the first part of this thesis, we introduced new flexible macroporous nanoelectronics that incorporate photopatternable polymers and “bottom-up” synthesized nanoelectronic units into designed networks and circuitry. This method can be readily applied to pattern virtually any nanomaterials (e.g. graphene, two-dimensional semiconductors, etc.) onto polymer substrate for flexible electronics fabrication. Using this 2D macroporous nanoelectronic network as precursor, we invented a mechanics-driven self-organization strategy to generate 3D regular and addressable nanoelectronic networks. This strategy offers opportunities to design and incorporate nanoscale electronic components into a 3D interconnected circuitry, which potentially could be used to significantly further enhance the density of functionally computing units in current integrated circuits. Considering limitations in further reducing the size of individual transistor, a 3D integrated circuit design that combines different modules could offer solutions for further enhancing the computing power in both CPU and GPU [1, 2]. Notably, different functional nanoscale components could be readily integrated into a 3D macroporous nanoelectronic network as a multifunctional embedded system [3].

In the second part of this thesis, we integrate this 3D macroporous nanoelectronic networks into soft material systems, translating inactive materials into very “smart” systems. Importantly, the low volume filling ratio, nanoscale feature size and ultra-flexibility of nanoelectronics introduce vanishingly-small interruptions to physical and chemical properties of host materials. In this direction, one can envision the incorporation of sensors, actuators, close loop control and radio-frequency identification circuitry into soft material to create smart systems that could be used for applications ranging from wearable devices to internet of things [4, 5].

In the third part of this thesis, we use 3D macroporous nanoelectronic network to mimic the structure of extracellular cellular matrix. We studied the seamlessly

integration of this biomimetic 3D nanoelectronic network with synthetic tissue scaffolds as hybrid nanoelectronic scaffold (nanoES) and growth of synthetic tissues within nanoES. Through this way, we can, for the first time, seamlessly and non-invasively innervate nanoelectronic units with cells throughout the whole tissue at single cell level. We show that nanoelectronic units can sense and stimulate activities at single cell and single spike level from neurons and cardiomyocytes throughout the whole 3D tissue, which cannot be achieved by traditional MEA, patch-clamp and optical technologies. More importantly, this integration will not alter the chemical and physical properties of synthetic tissue due to the ultra-flexibility and low filling ratio of nanoelectronic networks, which have been proved by imaging results and sensing experiments of chemical diffusion inside tissue. Therefore, this work has been widely considered as the first example of “cyborg tissue” [6].

This part of work can be further benefited by following studies. One is to incorporate nanodevices that can be delivered into intracellular environment for interrogation of intracellular activity. Building intracellular-nanoelectronics interface inside tissue is very challenging, yet important for fields from drug delivery to neuroscience. It requires a good mechanical match between the supporting structure and tissue to minimize the movement between cells and nanodevice that bridging intracellular environment and external connections. This seamlessly integration and bending stiffness match between nanoES and tissue provide an idea platform for this study. Second study is to incorporate vascular structure in synthetic tissue. Current synthetic tissue suffer from the size limitation due to the under developed synthetic vascular system. Therefore, the failure to deliver oxygen and nutrition into the central regions of synthetic tissues could cause cells death in synthetic tissue, limiting the size that tissue can grow. To further enhance this, microfluidic channels can be incorporated into nanoES to facilitate the delivery of oxygen and nutrition during synthetic tissue. The third study is to incorporate Complementary metal-oxide-semiconductor (CMOS) technique into flexible nanoES to dramatically increase the number of sensors to individually address all the cells throughout the whole tissue.

To move forward to applications, one direction is to develop cyborg tissues for drug screening assays [7]. Current drug screening assays employ 2D planar MEA or single-cell patch-clamp to record the response of tissue activities from drug stimulation, which lacks the capability to study the diffusion of drugs throughout the tissue. Optical imaging methods yet provide the 3D imaging, still suffer from a limited penetration depth and relatively low temporal resolution due to the requirement of 3D scanning. The results in our experiments that cells can form tight networks within nanoES and show similar behaviors, compared with synthetic tissues, to the external drug stimulation show potentials to use cyborg tissues as drug screen assays to study the diffusion effect of drug. The second direction is to make cyborg synthetic tissues for cellular therapies and employ the seamlessly integrated nanoelectronics as tools to locally monitoring and promote the process of integration between synthetic tissues and implanted systems. As example, a cyborg cardiac patch can be used to implant into patients’ malfunctioned heart for repairing

and monitoring [8]. The third one will be building of a dynamic nanoelectronic systems that can expand together with the developmental process of synthetic tissue to study the individual cell behavior throughout the whole tissue during tissue development.

The last part of the thesis introduces a syringe-injection method to deliver ultra-flexible mesh electronics into behaving animal brain tissues. The results from this example show a non-invasively chronic integration of mesh electronics within brain tissue and a neutrophilic electronics for recording. We envision this technique will bring revolutionary impacts into neuroscience, neurology and development of next generation brain-machine interface. First, current techniques used for deep brain mapping and stimulation suffer from strong immunoresponses from the surrounded neural tissue to the implanted probes, which typically lead to hundreds micrometers “killing zone” for neurons and scar tissues formation. Therefore, there is no way to stably sense/stimulate same neurons, especially same type of neurons for a long time. This is a major problem for electronics-enabled therapeutics such as deep brain stimulation (Parkinson’s disease, epilepsy, etc.) that requires long-term stable stimulation at effective brain regions, in which, consequently, patients suffer from re-adjustment of the implants every several months or even weeks [9]. Application of injected mesh electronics that introduce no chronic damage to the surrounding brain tissue with neural filament regenerated after months’ implantation could provide a much more robust nanoelectronic-neuron interface to reduce the extra-damage to patients and enhance the efficiency of therapy. In addition, those injected mesh electronics could gradually unfold inside brain, especially in embryonic and neonatal brain, in which tissues exhibit viscoelastic behavior rather than elastic behavior. Therefore, we can envision a delivery of mesh electronics with millions to billions sensors/stimulators followed by a complete unfold to fully distribute throughout the whole brain tissue for precise brain activity mapping at single neuron and single spike level for deciphering the brain coding [10].

Bibliography

1. Topol AW et al (2006) Three-dimensional integrated circuits. *IBM J. Rev. & Dev.* 50:491
2. Patti RS (2006) Three-dimensional integrated circuits and the future of system-on-chip designs. *Proc IEEE* 94:1214
3. Felton S, Tolley M, Demaine E, Rus D, Wood R (2014) A method for building self-folding machines. *Science* 345:644
4. Gao W et al (2016) Fully integrated wearable sensor arrays for multiplexed in situ perspiration analysis. *Nature* 529:509
5. Kortuem G, Kawsar F, Sundramoorthy V, Fitton D (2009) Smart objects as building blocks for the internet of things. *IEEE Internet Comput* 14:44
6. Service RF (2013) Bioelectronics. The cyborg era begins. *Science* 340:1162
7. Dai X, Zhou W, Teng G, Liu J, Lieber CM (2016) Three-dimensional mapping and regulation of action potential propagation in nanoelectronics-innervated tissues. *Nat. Nanotechnol.* 10.1038/nnano.2016.9611:776

8. Feiner R et al (2016) Engineered hybrid cardiac patches with multifunctional electronics for online monitoring and regulation of tissue function. *Nature Mater.* 15:679
9. Perlmutter JS, Mink JW (2006) Deep brain stimulation. *Annu Rev Neurosci* 29:229
10. Alivisatos PA et al (2013) Nanotools for neuroscience and brain activity mapping. *ACS Nano* 7:1850